Development of Track Reconstruction and Data Analysis Techniques for Neutrino Experiments

Thesis Submitted to

The University of Calcutta

for The Degree of

Doctor of Philosophy (Science)

By

Tapasi Ghosh

2010

Certificate from the supervisor

This is to certify that the thesis entitled **"Development of Track Reconstruction and Data Analysis Techniques for Neutrino Experiments"** submitted by **Tapasi Ghosh**, who got her name registered **(No. 3229 Ph.D. (Sc.) Proceed/ 2007)** on **24.09.2007** for the award of Ph.D. (Science) degree of University of Calcutta, is absolutely based upon her own work under my supervision and that neither this thesis nor any part of it has been submitted for any degree/diploma or any other academic award anywhere before.

<div align="right">

Dr. Subhasis Chattopadhyay

Scientific Officer

V.E.C. Centre, D.A.E.

Govt. of India

1/AF, Bidhan Nagar,

Kolkata-700064.

</div>

Dedicated to my loving son "Om"

ACKNOWLEDGMENTS

computational packages, great friendship and sharing different thoughts for all these years.

I also thank all the Ph.D. students, my seniors and juniors at VECC and the members of the Physics Group for interesting discussions and wonderful explanations, for their enjoyable company and support. My special thanks to my batchmates Sidharth, Mriganka, Arnomitra, Saikat, Jhilam, Rupa for their wonderful company in all these years and it is my great pleasure to thank Aparajita di, Mili di, Sukanya, Jamil, Arnab, Partha, Atanu da and Dhruba da. I have really enjoyed by working with them and their company.

My special thanks to my teachers from different academic institutes where I have studied, for their valuable suggestions, inspiration and encouragement, which help me to reach at this stage.

I would like to thank my wonderful parents Mr. Milan Kumar Ghosh and Mrs. Madhuri Ghosh, my mother-in-law Mrs.Jayanti Banerjee, my brother Manas, my husband Prasun and my relatives for believing in me. Their love, patience, constant support and inspiration help me to pursue my research works during all these years and I am extremely grateful to them. I have no words to acknowledge the sacrifice of my little son during the period of preparing this thesis work.

<div align="right">

Tapasi Ghosh

Kolkata, India

</div>

Abstract of The Thesis

Neutrino oscillation has been firmly established through a series experiments in last several years and spectacular results from those experiments have created a lot of interest in neutrinos, and many future neutrino experiments are in preparation to enhance our understanding about the tiny particle. In order to create an underground neutrino experiment facility in India, a multi-institutional neutrino collaboration has been formed with the objective of building an India-based Neutrino Observatory (INO). Cosmic pions are the main source of atmospheric neutrinos and the INO is a proposed atmospheric neutrino experiment. This thesis presents various works conducted for the development of simulation and data analysis framework for the INO experiment. In this thesis, we have discussed various aspects of simulation, prototyping and reconstruction of the INO detector towards investigating the phenomena of neutrino oscillation.

In INO, a 50kTon iron calorimeter (ICAL) will be the main detector and Resistive Plate Chambers (RPCs) will act as active detectors inside ICAL. A small prototype detector having geometry similar to ICAL has been installed at VECC. In the present work, we have simulated the response of the prototype by GEANT4 for incident cosmic muons. We have extended the simulation by performing two important steps towards reconstruction of muon tracks, likely to be produced by the charged-current (CC) interactions of atmospheric neutrinos.

The first step involves the use of the Artificial Neural Network (ANN) technique for discriminating muon hits from hadron hits layer by layer. We have taken the number of hits corresponding to a particular type of particles as input to ANN. It has been demonstrated that the method can isolate muon hits with an efficiency upto 98% with varying purity. The second step is to make use of the isolated muon hits and join them together to form muon tracks. A recursive algorithm known as Kalman Filter (KF) technique has been employed to fit the tracks towards obtaining best fitted track

parameters. KF incorporates the associated noise contribution while fitting. The fully contained (FC) muon tracks could be reconstructed with a momentum resolution of 15%. The reconstructed momenta have been found to be linear with respect to the incident tracks momenta.

For performing a complete simulation work, we have developed a Monte Carlo package for the simulation of RPC-response to minimum ionizing particle (MIP). As RPCs will be used as the sensitive detectors for ICAL, so this response simulation can be incorporated to the GEANT based simulation to obtain the realistic response. In the procedure different steps towards signal generation in RPC working in the avalanche mode e.g., primary ionization, avalanche formation & propagation, and finally signal generation have been incorporated. Additionally we have introduced a formalism for studying the RPC response due to the rough electrode surfaces. We have estimated the effects of roughness on efficiency and time resolution for a single-gap timing RPC. It is seen that the effect on time resolution is more prominent, compared to that on efficiency. The time resolution worsens by 30% for a 4% average variation in gap thickness, while the efficiency reduces by 10% due to a 20% variation in field caused by the surface roughness.

The aim of the work discussed in this thesis is towards building a self-consistent simulation and reconstruction procedure towards design and data analysis of ICAL.

Contents

List of Figures

xvii

List of Tables

Chapter 1

Introduction

1.1 Neutrino Physics

The existence of neutrinos in nature was first postulated in 1930 by Pauli [1] to explain the apparent energy non-conservation in nuclear beta decays. From the beta-decay, monoenergetic line spectrum of electron is expected, however a continuum spectrum was observed. To explain the observed spectrum, Pauli suggested the formation of a light neutral particle other than neutron and this particle was named as 'neutrino'. It was another 23 years before this bold theoretical proposal was verified experimentally in a reactor experiment performed by C.Cowan and F.Reines [2]. Most fundamental properties of neutrino were verified during the subsequent decade. Neutrino was shown to be left handed in an ingenious experiment by Goldhaber, Grodzins and Sunyar [3] in 1957. The distinct nature of ν_e and ν_μ was demonstrated in 1962 in a pioneering accelerator neutrino experiment at Brookhaven National Laboratory by Danby *et al.*[4]. Finally, the third neutrino flavour species ν_τ was discovered in the year 2000 at Fermilab by observing the τ leptons in a nuclear emulsion experiment [5].
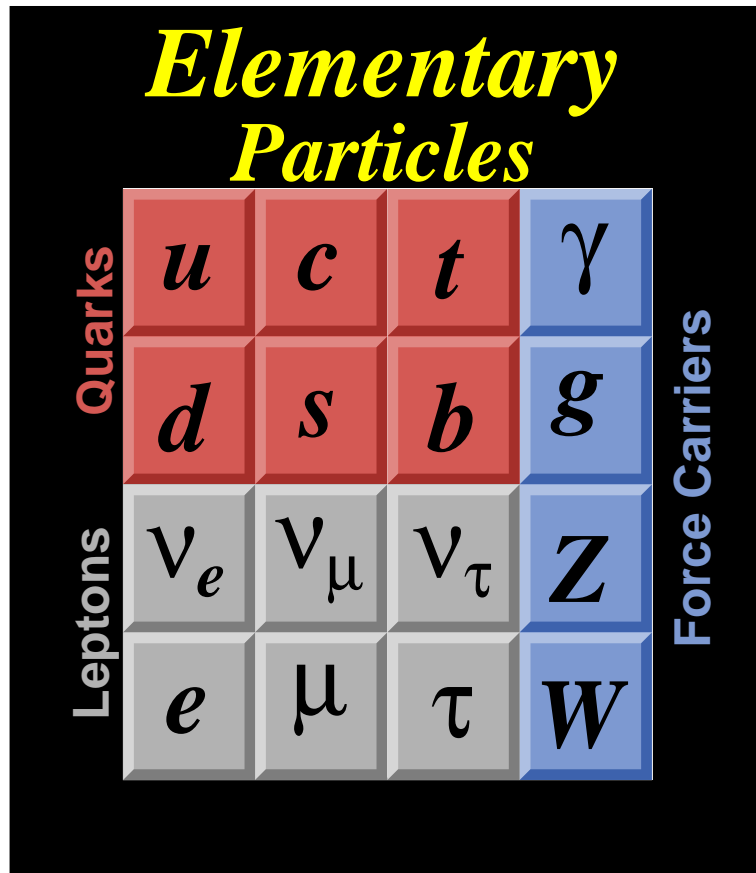
Figure 1.1: The elementary particles in standard model (SM).

Neutrinos are among the fundamental constituents in nature and in the "standard model"(SM) of fundamental particles, it was assumed that the neutrino is a massless fermion. Neutrinos undergo weak interactions, with tiny reaction cross-sections, and therefore exceedingly difficult to detect. The SM has twelve building blocks of matter, six leptons and six quarks, along with their anti-particles as shown in the figure 1.1. In SM, each massless neutrino is associated with charged lepton (e, μ or τ).

Neutrinos being weakly interacting particle, can travel long distances without suffering any interaction and during this travel one flavour of neutrino can transform into other flavour and this phenomenon was called "neutrino oscillation" [6, 7] by Maki, Nakagawa

and Sakata in 1962. Neutrino oscillation is the main signature of the existence of small but finite neutrino masses and neutrino mixing. In the following subsection the neutrino oscillation is discussed briefly.

1.1.1   Neutrino Oscillation

The study of neutrino oscillation offers us potentially the most sensitive approach to search for and to measure neutrino masses or to be very precise, neutrino mass-squared difference. The neutrino eigenstates that travel through space are not the flavour states, rather the mass states. The flavour basis undergoes weak interactions, whereas the mass eigenstates determine how neutrinos propagate. Each neutrino flavour state can be expressed as a quantum mechanical combination of mass eigenstates and for 2-flavour mixing :

$$\begin{pmatrix} \nu_e \\ \nu_\mu \end{pmatrix} = \begin{pmatrix} +\cos\theta & +\sin\theta \\ -\sin\theta & +\cos\theta \end{pmatrix} \begin{pmatrix} \nu_1 \\ \nu_2 \end{pmatrix} \tag{1.1}$$

i.e., the flavour states (ν_e, ν_μ) are associated with the mass states through a mixing matrix, where θ is the mixing angle and there is a probability to obtain a different flavour state other than the original one after some time and some distance. Hence, due to neutrino oscillation massive neutrinos will oscillate from one flavour (say, ν_e) to another flavour (say, ν_μ).

Neutrino Oscillation in vacuum

From equation 1.1 a ν_e state with momentum $\overrightarrow{p}$ at time t=0, can be represented by:

$$|\nu_e(t = 0)\rangle = \cos\theta \ |\nu_1\rangle + \sin\theta \ |\nu_2\rangle \tag{1.2}$$

where ν_1 and ν_2 are mass eigenstates with masses m_1 and m_2. When this state propagates in vacuum, each term picks up standard quantum mechanical phase factor for

plane wave propagation and so:

$$|\nu(\overrightarrow{x}, t)\rangle = e^{-i(E_1 t - \overrightarrow{p}.\overrightarrow{x})} \cos\theta \, |\nu_1\rangle + e^{-i(E_2 t - \overrightarrow{p}.\overrightarrow{x})} \sin\theta \, |\nu_2\rangle \tag{1.3}$$

In the relativistic limit, the energy E_i of the ith mass eigenstates is given by:

$$E_i = \sqrt{p^2 + m_i^2} = p\sqrt{1 + m_i^2/p^2} \approx p + m_i^2/2p$$

For $x = L$ and $t = L/c$ where L is the distance travelled by the neutrino, then equation 1.3 will be

$$|\nu(t)\rangle \rightarrow |\nu_1\rangle \cos\theta e^{-im_1^2 t/2p} + |\nu_2\rangle \sin\theta e^{-im_2^2 t/2p}. \tag{1.4}$$

After time t, the neutrino that was originally in a pure ν_e state is no longer in a pure ν_e state, but due to the phase difference $\phi = \left(\frac{m_1^2}{2p} - \frac{m_2^2}{2p}\right) t$, a non-zero component of ν_μ will appear and the neutrino state will be propotional to the following superposition:

$$|\nu(t)\rangle \propto |\nu_1\rangle \cos\theta + e^{i\phi} |\nu_2\rangle \sin\theta \tag{1.5}$$

Hence the probability that a original ν_e will appear as ν_μ [8]

$$P(\nu_e \rightarrow \nu_\mu) = |\langle \nu_\mu | \nu(t)\rangle|^2 = \sin^2 2\theta \sin^2 \frac{1.27 \Delta m^2 L}{E} \tag{1.6}$$

In the above equation $\Delta m^2 = m_1^2 - m_2^2$, $p \approx E$ in the relativistic limit. In equation 1.6, the first factor gives the amplitude whereas the second factor stands for the phase of the neutrino oscillation. The wavelength of oscillation can be obtained from this phase as,

$$\lambda = 2.54 \text{km} \left(\frac{E}{\text{GeV}}\right) \left(\frac{\text{eV}^2}{\Delta m^2}\right)$$

In equation 1.6, Δm^2 is in eV^2, and the neutrino energy E is in GeV. The probability formula has the characteristic dependence on L/E, which is a distinctive signature of neutrino oscillation. Figure 1.2 shows the oscillation probability vs. energy, as obtained from the equation 1.6. The oscillations of atmospheric ν_μ and solar ν_e can be
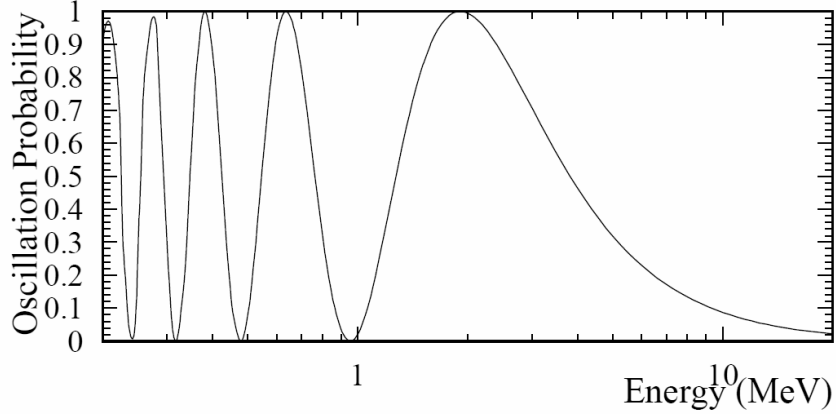
Figure 1.2: Oscillation probability as a function of neutrino energy for fixed value of $\Delta m^2 L$ and $\sin^2 2\theta$=1. (Figure adopted from Ref. [8])

explained separately by considering each as a two neutrino system. However, both the phenomena of solar and atmospheric neutrino oscillations can be explained together if we consider a three neutrino mass system.

1.1.2   The three-flavour picture

Similar to the 2×2 mixing in equation 1.1, the three neutrino flavour eigenstates are related to the mass eigenstates by a 3×3 unitary matrix, completely analogous to the CKM matrix for quarks. The neutrino mixing matrix is known as MNS matrix for Maki, Nakagawa, and Sakata, and occasionally PMNS considering Pontecorvo's early contributions to the neutrino oscillation. The relationship between flavour and mass states can be expressed by the following matrix equation:

$$
\begin{pmatrix} \nu_e \\ \nu_\mu \\ \nu_\tau \end{pmatrix} = \begin{pmatrix} U_{e1} & U_{e2} & U_{e3} \\ U_{\mu1} & U_{\mu2} & U_{\mu3} \\ U_{\tau1} & U_{\tau2} & U_{\tau3} \end{pmatrix} \begin{pmatrix} \nu_1 \\ \nu_2 \\ \nu_3 \end{pmatrix}
\tag{1.7}
$$

where the probability for a transition from flavour a to b is given by[9]:

$$
\begin{aligned}
P_{(\nu_a \to \nu_b)} &= \delta_{ab} - 4 \sum_{j>i} \mathrm{Re}(U_{ai}^* U_{bi} U_{aj} U_{bj}^*) \sin^2(1.27\Delta m_{ij}^2 L/E) \\
&\pm 2 \sum_{j>i} \mathrm{Im}(U_{ai}^* U_{bi} U_{aj} U_{bj}^*) \sin^2(2.54\Delta m_{ij}^2 L/E).
\end{aligned}
\tag{1.8}
$$

with L in km, E in GeV and Δm^2 in eV^2. In equation 1.8, i,j are the indices for mass eigenstates and U is the mixing matrix. The 3×3 PMNS matrix [6, 10] in equation 1.7, can be expressed by:

$$
U = \begin{pmatrix} 1 & 0 & 0 \\ 0 & c_{23} & s_{23} \\ 0 & -s_{23} & c_{23} \end{pmatrix} \begin{pmatrix} c_{13} & 0 & s_{13}e^{i\delta} \\ 0 & 1 & 0 \\ -s_{13}e^{i\delta} & 0 & c_{13} \end{pmatrix} \begin{pmatrix} c_{12} & s_{12} & 0 \\ -s_{12} & c_{12} & 0 \\ 0 & 0 & 1 \end{pmatrix}
\tag{1.9}
$$

where "s" represents the sine of each mixing angle($s_{ij} \equiv \sin \theta_{ij}$) and "c" represents the cosine term ($c_{ij} \equiv \cos \theta_{ij}$). The minus sign refers to the neutrinos and the plus sign for the anti-neutrinos. The familiar two-flavour oscillation formula is the limiting case when a single Δm^2 between two states is considered, which is discussed in the earlier subsection.

With the three neutrino masses, there are two neutrino mass differences $(\Delta m_{21}^2, \Delta m_{32}^2)$, three mixing angles $(\theta_{13}, \theta_{23}, \theta_{12})$ and one CP violating phase δ. From our current understanding from recent experiments [9, 11] on solar and atmospheric neutrino, the values of the two mass squared differences, and two mixing angles $(\theta_{23}, \theta_{12})$ are known. In the decomposition above in equation 1.9, the disappearance of solar neutrinos is driven by the oscillations of 1-2 mass states, which are mixed by the matrix with the θ_{12} terms, and the observed disappearance of the atmospheric neutrinos is driven by the matrix having θ_{23} terms. At the middle mixing matrix, there is the unmeasured θ_{13} term. The non-zero value of θ_{13} is currently a high priority topic in the field of neutrino physics and a description about the upcoming reactor and accelerator experiments
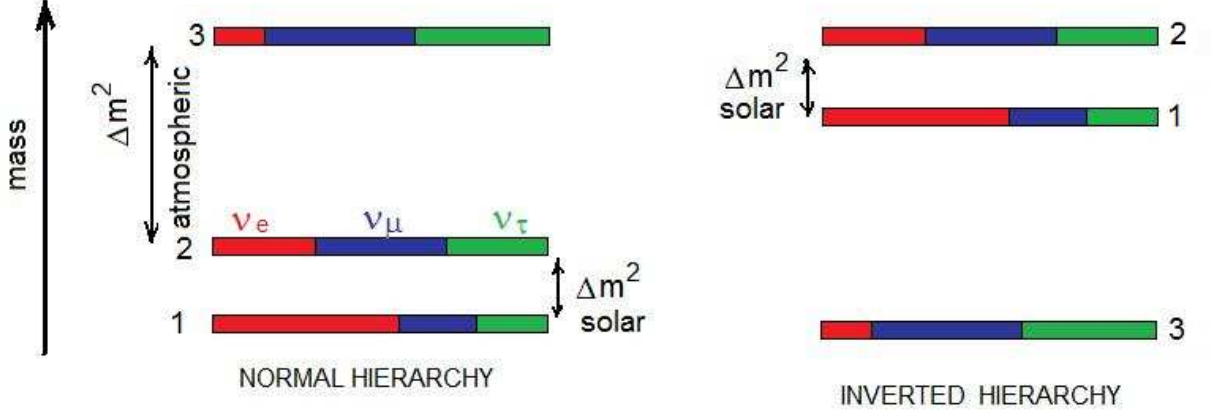
Figure 1.3: Neutrino mass eighenstates (1,2,3) as a combination of flavour states (e, μ, τ) and the schematic of normal and inverted hierarchies.

searching for the value of θ_{13} is given in Ref. [11]. The δ term in the above expression stands for CP violation and for a non-zero value of δ, the oscillation probability for neutrinos will be different from that of anti-neutrinos i.e., $P(\nu_e \to \nu_\mu) \neq P(\bar{\nu}_e \to \bar{\nu}_\mu)$.

Measurements of atmospheric and solar neutrino oscillations also help us, to partially determine the pattern of neutrino masses. The solar neutrino experiments have successfully inferred the sign of Δm_{21}^2 because the MSW effect in the Sun dominates in solar neutrino oscillations and the sign of the effect depends on the sign of Δm_{21}^2. The MSW (Mikheyev-Smirnov-Wolfenstein) effect [12] is the effect of transformation of one neutrino species (flavour) into another one in a medium with varying density (discussed in next subsection). Whereas the atmospheric neutrino data do not have significant sensitivity to matter effects, and therefore it is not well determined whether $m_2 < m_3$ or $m_2 > m_3$. However, the atmospheric neutrinos are the only source to study the matter effect until very long baseline experiments using β-beams or neutrino factories [13] are built. A simulation study of neutrino mass hierarchy by atmospheric neutrinos

(energies 2-10 GeV) with pathlength in the range of 4000-12500km inside the earth, for magnetized iron calorimeters and water Cerenkov detectors has been reported in Ref. [14]. Due to the ambiguity in neutrino mass scale ($m_2 < m_3$ or $m_2 > m_3$), there are two possible hierarchies for the neutrino mass eigenstates. The "normal" hierarchy has two light states and one heavier state, with $m_1 < m_2 < m_3$ and in "inverted" hierarchy m_3 is the lightest state as shown in figure 1.3. It is very important to mention that the neutrino oscillation experiments are only sensitive to the mass-square difference, and do not measure the absolute masses.

1.1.3 Matter effects

Neutrinos being very weakly interacting particle can travel from one end of the entire earth to the other end and the presence of matter influences the neutrino propagation and hence the oscillation probability in presence of matter will be different when compared to their vacuum counterpart. Normal matter contains copious numbers of electrons, however never any μ or τ. While travelling through the matter, neutrinos can interact with leptons in matter, so electron type neutrinos contribute in both charged current and neutral current weak interactions whereas other flavour neutrinos (ν_μ and ν_τ) contribute only in neutral current interaction, represented in figure 1.4. As a result, electron neutrinos pick up an extra interaction term proportional to the density of electrons in matter, which acts as a matter induced potential. While calculating the effects of the matter interaction on neutrino oscillation known as **matter effects** [12], the influence of the neutral current interaction is ignored since its' effect is same for all flavour of neutrinos.
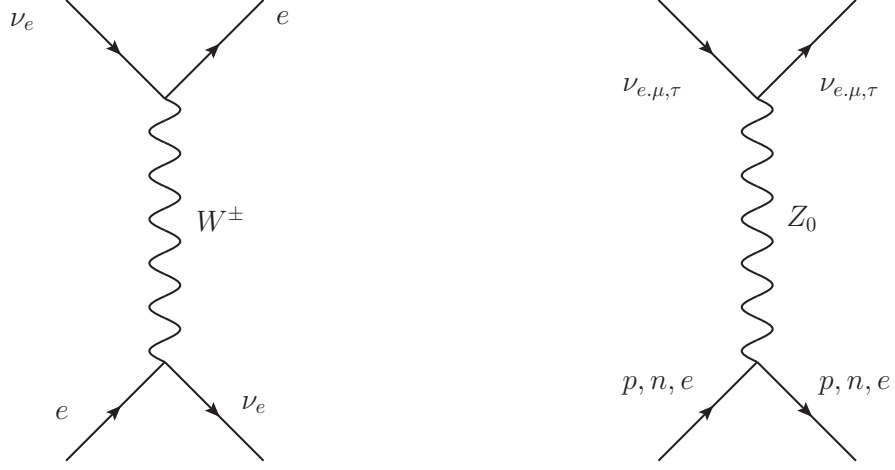
Figure 1.4: Feynman diagrams representing the neutrino interactions inside matter. Left picture shows CC interactions whereas right picture depicts NC processes.

The time evolution of the neutrino flavour in flavour basis including both mixing and matter effect is given by [8]:

$$i\frac{d}{dt}\begin{pmatrix} \nu_e \\ \nu_\mu \end{pmatrix} = \begin{pmatrix} -\frac{\Delta m^2}{4E}\cos 2\theta + \sqrt{2}G_F n_e & \frac{\Delta m^2}{4E}\sin 2\theta \\ \frac{\Delta m^2}{4E}\sin 2\theta & \frac{\Delta m^2}{4E}\cos 2\theta \end{pmatrix}\begin{pmatrix} \nu_e \\ \nu_\mu \end{pmatrix}$$

So, the additional interaction experienced by the electron type neutrino while crossing the matter is provided by [12],

$$V \simeq \sqrt{2}G_F.n_e$$

where n_e is the density of electron in matter and G_F is the Fermi coupling term. This effect known as MSW effect after Mikheev, Smirnov, and Wolfenstein [12], gives rise to a rich phenomenology in which oscillation probabilities in dense matter, such as the interior of the sun, can be different from the vacuum probability. Experimentally in solar neutrino oscillations the MSW effect plays a significant role, although the future long-baseline neutrino oscillation experiments will also be sensitive to matter effect. The strength of V inside the Sun, the Earth and a supernova is listed in Table 1.1.

We can estimate the importance of matter effects on neutrino oscillations if the value

Table 1.1: Matter potential in different mediums

Medium	Matter Density	Matter Potential (V)
Solar core	$\sim 100 \text{gm/cm}^3$	$\sim 10^{-12} \text{eV}$
Earth core	$\sim 10 \text{gm/cm}^3$	$\sim 10^{-13} \text{eV}$
Supernova	$\sim 10^{14} \text{gm/cm}^3$	$\sim \text{eV}$

of the matter potential is compared with $\Delta m^2 / 2E$. If we consider a 5GeV neutrino travelling through the core of the Earth then V will be compitable with the value of $\Delta m^2 / 2E (= 2.5 \times 10^{-13} \text{eV}$ if $\Delta \text{m}^2 = 10^{-3} \text{eV}^2)$.

In presence of matter effect, the 2-flavour mixing matrix will be :

$$\begin{pmatrix} \cos \theta_m & \sin \theta_m \\ -\sin \theta_m & \cos \theta_m \end{pmatrix}$$

where θ_m is the mixing angle in matter and similarly the conversion probability will be,

$$P_{e\mu} = P_{\nu_e \to \nu_\mu} = \sin^2 2\theta_\text{m} \sin^2 \left(\frac{\pi \text{L}}{\lambda_{21}^\text{m}} \text{t} \right) \tag{1.10}$$

where

$$\lambda_{21}^m = \frac{\pi E}{1.267 \delta_{21}^m}$$

is the **oscillation wavelength** in presence of matter.

Through the neutrino oscillation phenomenon, quantum mechanics probe the measurement of the smallest massive particle. According to the SM, neutrinos should be massless. Thus the neutrino experiments claim most importantly *an extension of the standard model*. Many of the popular extensions of the Standard Model do indeed predict nonzero neutrino masses and the existence of neutrino oscillation [15]. The existence of the oscillation phenomenon is established by several experimental observations as mentioned below and discussed in section 1.1.4.

(a) The need for dark (i.e., non-shining) matter [16] , is based mainly on three phenomena: the motion of galaxies, the flat rotational curves for stars in spiral galaxies, and the successes of inflationary Big Bang cosmology which predicts that the density of the universe equals the so-called critical density. Neutrinos, since they are present in abundance everywhere, could account for at least a part of the dark matter as they have finite mass.

(b) The solar neutrino deficit, i.e., the observation of fewer sun-originated neutrinos on earth than is expected from the known solar luminosity [17].

(c) The atmospheric neutrino anomaly [18], i.e., a measured ν_μ/ν_e ratio for neutrinos from cosmic ray interactions in our atmosphere is significantly smaller than predicted. The hypothesis that this anomaly is caused by neutrino oscillations is strongly supported by the observation of up-down asymmetry in the atmospheric ν_μ flux by the Super-Kamiokande Collaboration [19], as well as their studies of upward going muons.

1.1.4   Solar Neutrino experiments

The Sun is a prolific source of neutrinos (mainly ν_e) with energies in the range $\sim$ $0.1 - 20$MeV and these neutrinos are generated due to the fusion reaction

$$4p + 2e^- \rightarrow {}^4_2He + 2\nu_e + 26.731 \ MeV \tag{1.11}$$
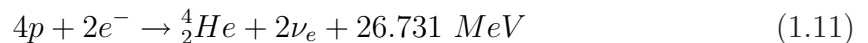
The Sun emits $\sim 2 \times 10^{38}$ electron neutrinos per second, leading to the neutrino flux on the surface of the earth $\sim 6 \times 10^{10}$ cm^{-2}s^{-1} in the energy range $E \le 0.42$ MeV and flux $\sim 5 \times 10^6$ cm^{-2}s^{-1} in the energy range 0.8 MeV $\lesssim$ E ≤ 15 MeV. The Ray Devis's chlorine experiment in the Homestake mine, South Dakota [20] measured the ν_e by analyzing the Ar atom production through the reaction $\nu_e + {}^{37}Cl \rightarrow {}^{37}Ar + e^-$. It is
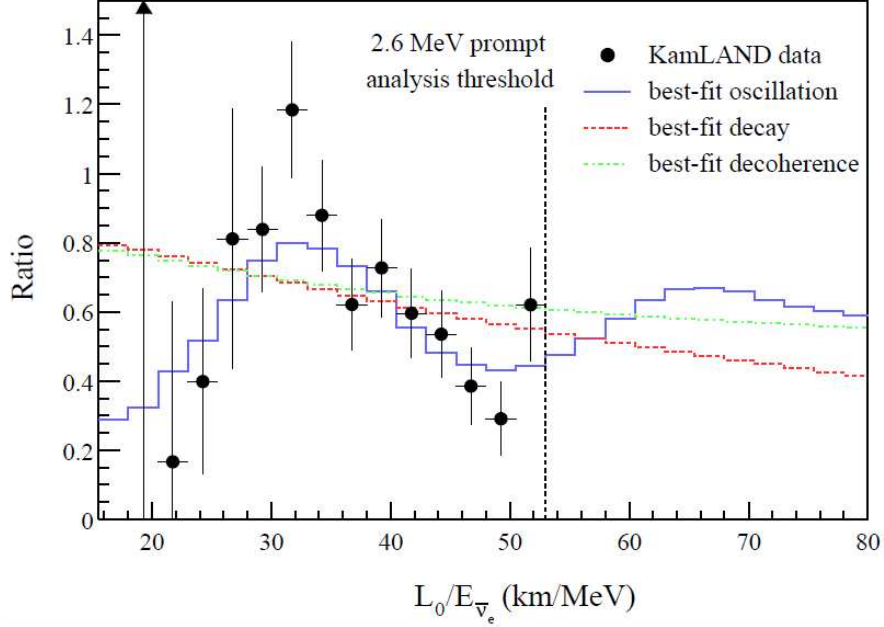
Figure 1.5: Ratio of the $\bar{\nu}_e$ flux to the expected flux measured by the KamLand with no oscillation, at different L/E values.(Figure adopted from Ref. [8])

observed that the measured flux of ν_e is $\sim 1/3$ of that predicted by various solar model calculations. Description about other approaches/experiments to measure the solar neutrino flux can be obtained in Ref. [8]. From multiple experiments with different measurement techniques, it is confirmed that the deficit in measured ν_e flux compared to the model prediction, is the conversion of solar ν_e to other flavours.

1.1.5 KamLand: the reactor neutrino experiment

KamLand is a reactor neutrino experiment facility in Japan, which generates $\bar{\nu}_e$ flux with peak energy ~ 3 MeV. The observed $\bar{\nu}_e$ flux was $\sim 1/3$ of that expected and figure 1.5 shows the L/E dependence of the ratio of the measured $\bar{\nu}_e$ flux with the expected one with no oscillation. This result was quite compatible with the solar
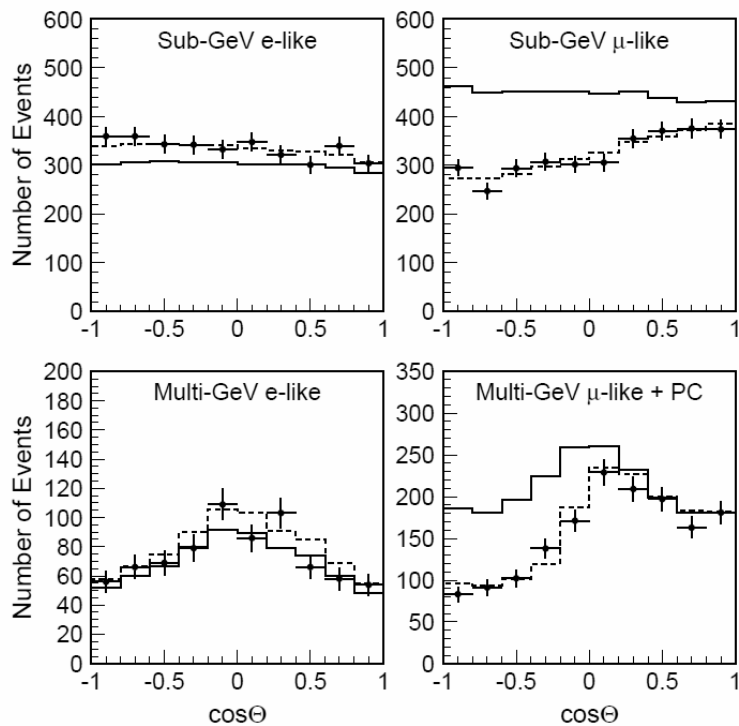
Figure 1.6: ν_μ and ν_e fluxes measured by the Super-Kamiokande experiment. Solid lines are for the 'no oscillation' prediction and the dashed line passing through the data points are the best-fit oscillation prediction.(Figure adopted from Ref. [8])

neutrino results and suggested that the flavour change due to the neutrino oscillation is the correct explanation of the deficit in measured neutrino flux [21].

1.1.6 Atmospheric neutrinos

Atmospheric neutrinos are generated when cosmic protons interact with the atmospheric particles and create hadronic showers. The pions in the showers decays to

$\pi^{\pm} \rightarrow \mu^{\pm}\nu_{\mu}$ and simultaneously $\mu^{\pm} \rightarrow e^{\pm}\nu_{\mu}\nu_{e}$. Hence for atmospheric case, the ν_{μ} flux is twice of the ν_{e} flux. The Super-Kamiokande experiment [19, 22] shows that the measured ratio of ν_{μ} and ν_{e} flux is $\sim 1 : 1$. the value of the deficit varies with neutrino energy and also with zenith angle of the events. Figure 1.6 shows the variation of the expected and measured flux of ν_{μ} at different zenith angle and also with varying energy range. As shown in figure 1.6, data can reasonably be explained with oscillation.

1.2 Estimation of neutrino parameters from different experiments

Neutrino oscillations have been firmly established by a series of experiments with neutrinos from the Earth's atmosphere [19, 22], Sun [20, 23, 24, 25, 26, 27, 28], nuclear reactors [29, 30], and accelerators [31, 32]. All these data can be described within a three–flavour neutrino oscillation framework, characterized by two mass-squared differences $(\Delta m_{21}^2, \Delta m_{31}^2)$, three mixing angles $(\theta_{12}, \theta_{13}, \theta_{23})$, and one complex phase (δ), as mentioned earlier. We know that two out of the three mixing angles are large [33],

$$\sin^2 \theta_{12} = 0.318^{+0.019}_{-0.016}, \qquad \sin^2 \theta_{23} = 0.50^{+0.07}_{-0.06}. \qquad (1.12)$$

The mass-squared differences are determined relatively accurately from the spectral data in the KamLAND [30] and MINOS [32] experiments, respectively [33],

$$\Delta m_{21}^2 = 7.59^{+0.23}_{-0.18} \times 10^{-5} \text{ eV}^2, \qquad |\Delta m_{31}^2| = 2.40^{+0.12}_{-0.11} \times 10^{-3} \text{ eV}^2. \qquad (1.13)$$

The sign of Δm_{31}^2 is not confirmed i.e., whether $m_3 > m_1$ or vice versa. The parameters in eqs. 1.12 and 1.13 are responsible for the dominating oscillation modes observed in the experiments mentioned above. The present information on the value of θ_{13} emerges from an interplay of the global data on neutrino oscillations, as illustrated in fig. 1.7, from recent global analysis [33, 34, 35, 36] .
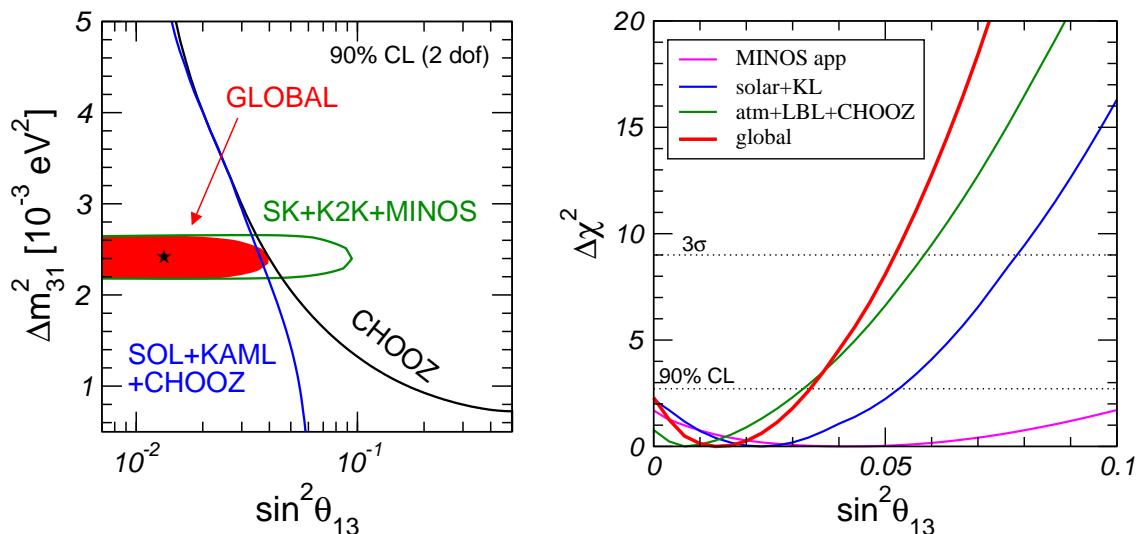
Figure 1.7: Constraints on $\sin^2 \theta_{13}$ from different parts of the global data [33](adopted from Ref [37]).

From the global analysis, the third mixing angle, θ_{13}, whose value is not known at present, and is constrained to be small compared to the other two angles [33] is obtained as follows:

$$
\begin{aligned}
\sin^2 \theta_{13} &\leq 0.034 \quad (0.053) \\
\sin^2 2\theta_{13} &\leq 0.13 \quad\;\; (0.20) \qquad\qquad 90\% \; (3\sigma) \; \text{CL} . \\
\theta_{13} &\leq 10.6° \quad (13.3°)
\end{aligned}
\tag{1.14}
$$

An important contribution to the bound on θ_{13} comes from the non-observation of disappearance of reactor electron anti-neutrinos at the scale of Δm_{31}^2 at the CHOOZ [38] and Palo Verde [39] experiments, while the final bound is obtained from the combination of global neutrino oscillation data. The value of θ_{13} has a big influence to solve the mass hierarchy problem. The most promising way to distinguish neutrino mass-squared differences is to search for the matter effect in transition due to Δm_{31}^2. The condition for the MSW resonance is

$$
\cos 2\theta_{12} = \pm \frac{2E_\nu V}{\Delta m_{31}^2}
\tag{1.15}
$$

15

where +(-) holds for (anti)neutrinos. The above equation will be satisfied for ν or $\bar{\nu}$ for a given sign of Δm_{31}^2. The matter resonance due to Δm_{31}^2 for ν or $\bar{\nu}$ will determine the sign of Δm_{31}^2. However the occurrence of matter effect in Δm_{31}^2 transitions is only feasible for a non-zero θ_{13}. Hence the possibility to determine the neutrino mass hierarchy through the observation of matter effect crucially depends on the observability of θ_{13} value.

1.2.1   The LSND result and the MiniBooNE Experiment

The LSND collaboration [40] reported the evidence of observing $\bar{\nu}_\mu \to \bar{\nu}_e$ oscillation. The values of the mixing parameters obtained from this experiment are $\sin^2 2\theta \approx 10^{-3} - 10^{-2}$ and $\Delta m^2 \sim 0.1 - 1.0$ eV^2. Hence, the value of Δm^2 obtained from the LSND result is much higher than those obtained from the solar and atmospheric neutrino experiments. If the LSND effect is due to neutrino oscillation, then it implies a third independent value of Δm^2, and so requires a fourth neutrino mass eigenstate. Because for three light neutrinos, there can have only two independent mass differences i.e. Δm_{21}^2 and Δm_{32}^2. If $\theta_{13} = 0$, then electron neutrino does not mix with ν_3, so $\Delta m_{31}^2 \approx \Delta m_{32}^2$. So if a fourth neutrino exists, it must be sterile i.e. non-interacting; however detailed analysis of solar and atmospheric data do not infer any existence of a single sterile neutrino [41]. At present the MiniBooNE experiment [42] at FermiLab is attempting to verify the LSND result.

1.2.2   MINOS and MiniBooNE results on CPT violation

Recently MINOS and MiniBooNE collaborations claim the CPT violation in neutrino sector. According to the CPT theorem, particle mass will be same of its' own anti-particle. MINOS collaboration has looked for ν_μ and $\bar{\nu}_\mu$ beams and it is observed that

neutrinos exhibit masses different from anti-neutrinos, thus violates the CPT theorem. It is reported in Ref. [43] that this is most probably the first time any experimental observation claims for CPT violation. The MINOS experiment looking for $\bar{\nu}_\mu \to \bar{\nu}_\tau$ and the mass-difference and mixing angle obtained is different than that of neutrinos [43]:

$$\Delta m_{32}^2 = 3.36_{-0.40}^{+0.45} \pm 0.06 \times 10^{-3} \text{ eV}^2; \sin^2 2\theta_{23} = 0.86 \pm 0.11 \pm 0.01 \qquad (1.16)$$

where the first error is statistical and the second is systematic and these anti-neutrino values have 2σ level discrepancy from the neutrino values in equation 1.13 & equation 1.12. The MiniBooNE results for $\bar{\nu}_e \to \bar{\nu}_\mu$ appearance are [43]:

$$\Delta m_{21}^2 = 0.064 \text{ eV}^2; \sin^2 2\theta_{21} = 0.96. \qquad (1.17)$$

So these values are very much different from solar $(\nu_e \to \nu_\mu)$ results. Therefore MINOS and MiniBooNE experiments together claim a very strong evidence that properties of $\bar{\nu}'s$ to be radically different from those of $\nu's$, to the extent of violating CPT invariance.

1.2.3 Existence of Tau Neutrino from OPERA Experiment

Several experiments have observed the disappearance of muon-neutrinos, confirming the oscillation hypothesis, but until now no observation for the appearance of a tau-neutrino in a pure muon-neutrino beam has been reported. The OPERA [44] neutrino detector in Gran Sasso Laboratory (LNGS) has been designed for the first detection of neutrino oscillations in direct appearance mode in $\nu_\mu \to \nu_\tau$ channel. The detectors are designed to face the high energy long-baseline CERN to LNGS neutrino beam (CNGS). At CERN, neutrinos are generated from the collisions of an accelerated beam of protons with a target. When protons hit the target, particles like pions and kaons are produced. They quickly decay, giving rise to neutrinos. The OPERA neutrino detectors detects the short-lived τ lepton ($c\tau = 87\mu m$) produced due to ν_τ charged-current interaction. The first observation of τ lepton detection possibly generated by

an oscillated ν_τ interaction, has been reported in Ref [45]. The existance of τ in this experiment is observed by the detection of its characteristic decay topologies, either in one prong (e,μ or hadron) or in three prongs. Appearance of ν_τ will prove that $\nu_\mu \to \nu_\tau$ is the dominant transition channel at the atmospheric scale. One of the observed τ
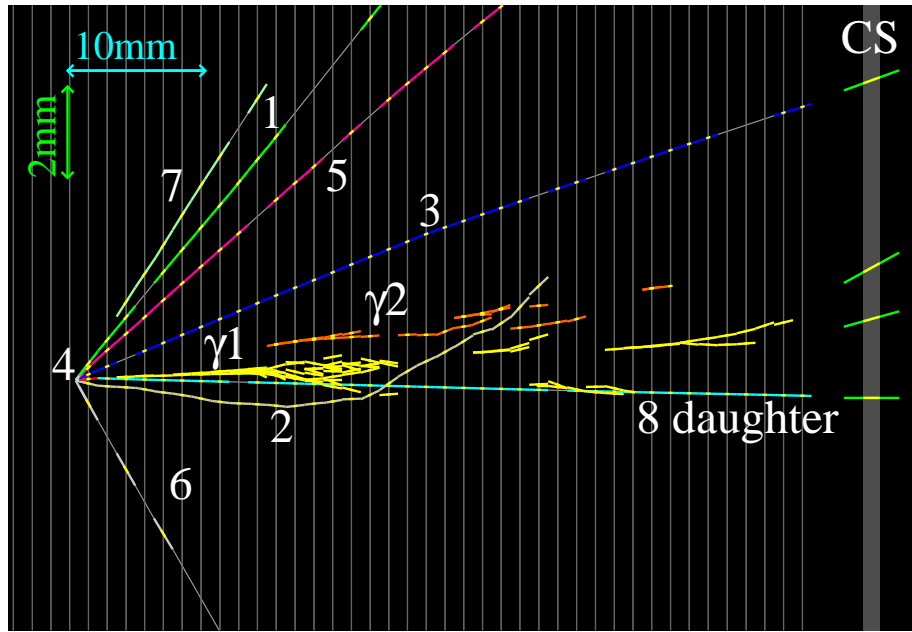
Figure 1.8: The τ event observed in OPERA experiment, adopted from Ref. [45].

decay is shown in figure 1.8.

1.3 Future directions in Neutrino Oscillation Experiments

Last decades saw a remarkable progress in neutrino experiments, especially those utilizing accelerators as their sources. Improvements in available accelerator energies and intensities, advances in neutrino beam technology, and more sophisticated and massive

neutrino detectors were all instrumental which enable to perform more precise neutrino experiments. We are now in a new era of experimental neutrino physics whose main thrust is twofold: better understanding of the nature of neutrino physics , i.e., a study of the neutrino properties, and use of the neutrino in astrophysics and cosmology as an alternative window to view the universe.

So far from different experiments, we are able to know Δm^2 parameters in a precision of $\sim 10 - 20\%$, and two of the three mixing angles are known approximately. Our ultimate goal is to know the values of all the components of the MNS matrix i.e., for completion of the picture, it is very important to measure the unknown mixing matrix parameters θ_{13} and δ_{CP}, along with the sign of Δm^2_{32} which will finally solve the hierarchy problem i.e. whether neutrinos have normal or inverted hierarchy.

1.4   India-based Neutrino Observatory

Indian initiative for neutrino physics experiment started with the Kolar Gold Field (KGF) underground laboratory in 1965 and the experiment ended with the closing of the mine in 1992. The KGF experiments involved a systematic study of the cosmic ray muons and neutrinos, and other exotic processes at large underground depth for several years. The experience gained from this experiment will be utilized to build a large scale neutrino experiment, known as the India-based Neutrino Observatory(INO) [46]. The main detector for the INO will be a 50kTon magnetized iron calorimeter (ICAL). All the details about the ICAL detector is explained in chapter 2. INO is an atmospheric neutrino experiment and the main sources of atmospheric neutrinos (ν) are the cosmic muons, generated due to the interaction of the highly energetic cosmic protons with the atmospheric nuclei. These neutrinos produce corresponding charged leptons while interacting with the iron nuclei of the calorimeter e.g., $\nu_\mu + p \rightarrow \mu^- + X$ where X
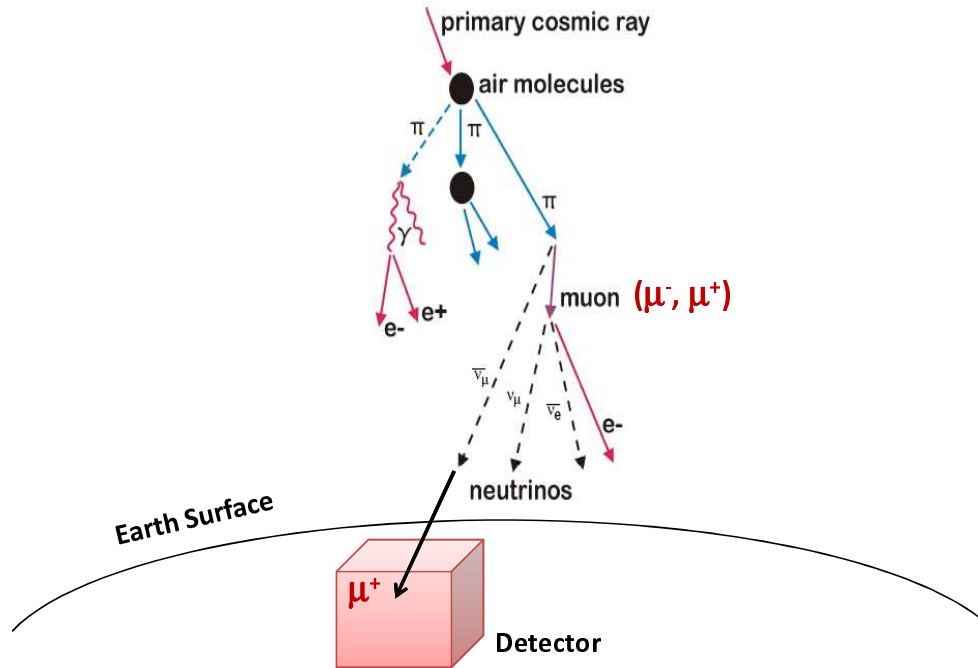
Figure 1.9: Schematic of the atmospheric neutrino production above the Earth's surface and production of muons after ν_μ interaction inside the ICAL detector.

denotes the hadrons. In INO, muons generated by the muon-neutrino (ν_μ) interactions are the signal particles to be detected, as shown schematically in the figure 1.9. Hence, the cosmic muons act as background to the signal muon, later one generated due to the ν interactions. To separate out the signal muon from a huge cosmic background, the site for the INO experimental hall requires to be surrounded by ~ 1 km mountain rocks almost in three directions.

1.4.1 Physics goals of the INO experiment

The major physics goals of the INO experiment are the following:

1. Re-confirmation of the neutrino oscillation phenomenon for atmospheric muon neutrino through the explicit measurement of the oscillation swing in ν_μ disappearance as a function of L/E.

2. Precise measurement of the atmospheric neutrino oscillation parameters.

3. Measurement of the influence of matter effect on the neutrino oscillation.

4. Determination of the sign of Δm^2_{32} using the matter effect.

5. To prove the CPT violation in the neutrino sector using the atmospheric neutrino oscillation phenomenon.

6. To explore the existence of sterile neutrino, if any.

The β-beam

A high intensity source of a single neutrino flavour with known spectrum is most appropriate for precision measurement. The Beta-Beam [47] is an expedient option for this purpose where the beam contains a single neutrino flavour. In this subsection, some details about the possible utilization of β-beam for the INO experiment is discussed.

$\bar{\nu}_e$s are produced by the super-allowed β^- transition

$$\ _2^6He \rightarrow\ _3^6Li + e^- + \bar{\nu}_e \tag{1.18}$$

Electron neutrino beams can be produced by the super-allowed β^+ transition

$$\ _{10}^{18}Ne \rightarrow\ _9^{18}Fe + e^+ + \nu_e \tag{1.19}$$

Long baseline experiments with neutrino beams is of extreme physics interest and the ICAL detector of INO could be utilized as a favorable target. The base ICAL design is

a 50 kton Fe detector with an energy threshold around 800 MeV. ICAL will be a good choice for a very long baseline β-beam experiment, with a source at CERN, Geneva (L= 7177 km from PUSHEP). The CERN to INO experimental site distance is very close to the 'magic baseline' ($\sim$ 7000 Km) where matter effects are largest and the effect of CP phase is negligible. For the baselines considered here, the neutrino beams will pass through the mantle of the earth and the density of the earth is assumed to be constant.

It is expected that the ICAL detector will be able to measure the mixing angle θ_{13} and the sign of Δm^2_{32} accurately, when the detector will face the high energy Beta Beam. Again as the CERN-INO distance is similar to the 'magic' baseline, so the INO data will be insensitive to the CP phase δ.

1.5   Motivation of the thesis

In the present work, we have studied various aspects of the INO calorimeter in terms of detector properties and data processing:

(A) Reconstruction of muon tracks by Kalman filter : One of the main goals of INO experiment is to study the neutrino oscillation phenomena and precise measurement of the atmospheric neutrino oscillation parameters. These parameters can be extracted by reconstructing the neutrino events from the products of the interaction. For example, neutrino energy (E) and the total path (L) traversed by the neutrino before interaction are used to construct a variable (L/E) for studying the oscillation parameters. Precise measurement of these quantities is therefore a pre-requisite for extracting the physics variables. To reconfirm the neutrino oscillation phenomenon in INO, it is required to measure the energy of the neutrino

event E, mentioned in equation 1.6. Due to charge-current interaction inside the ICAL detector, a neutrino produces muons associated with hadron showers. Muons generated due to a neutrino interaction carry most of parent neutrino energy. The measurement of momentum of the muon events or muon track inside the detector is performed by Track Reconstruction method utilizing Kalman Filter [48] algorithm. During the track reconstruction process, fitting of the each muon track is performed and momenta of the muon tracks are obtained, which is explained in chapter 5. The importance of this work is to evaluate the neutrino energy which will finally help to estimate the neutrino oscillation phenomena.

(B) Identification of muon hits in calorimeter layers : Before the track reconstruction process, it is very important to identify individual track inside the calorimeter. Muons are generated together with the hadrons from a ν interactions, however muons being minimum ionizing particle, leaves a long track inside the calorimeter compared to that of the hadron, which forms shower. It is extremely important to identify the muon hits from the mixture. We have developed an algorithm based on the Artificial Neural Network (ANN) for the discrimination of muon hits from the hadron hits inside the iron calorimeter detector layers. This part of the work is discussed in chapter 4. Those isolated muon hits will be further used to form a muon track and finally momentum of the muon track will be reconstructed by track fitting method.

(C) Simulation to the study effect of surface roughness on RPC performance : Resistive Plate Chambers are the active detectors inside the INO calorimeter for tracking charged particles generated by neutrino interactions. At VECC, we have built RPCs [49] using bakelite electrodes of different dimensions and it is observed that the surface profile of the bakelite sheets are not as smooth as that of glass surface. It is therefore very important to study the effect of the surface non-

uniformities of the electrodes, on the performance of RPC. We have developed a Monte Carlo method to calculate the time resolution(σ) and the efficiency of a single-gap timing RPC and studied the effect of the surface roughness of the electrodes on time resolution and efficiency of the detector. Detail description of the work and result is discussed is in chapter 6.

In summary, the work in this thesis is organized as follows, we have developed the geometry of the prototype of the INO iron calorimeter (ICAL) using GEANT4 simulation toolkit. We then analyzed the response of the simulated prototype detector volume for cosmic muon flux, which is discussed in chapter 3. In the chapter 4, we explain how the muon hits can be separated from the hadronic showers by using the Artificial Neural Network technique for the ICAl detector and then in chapter 5. we discuss the procedure by which the momenta of the muon tracks are reconstructed by Kalman Filter method. In chapter 6, we discussed the Monte Carlo procedure which we developed to simulate the response of a RPC and the effect of surface roughness on its' performance. Finally, we summarize the results and give the outlook in chapter 7 with a description of the steps needed for implementing them in ICAL data analysis.

Chapter 2

The Iron Calorimeter (ICAL) and Resistive Plate Chamber as active detector for ICAL

2.1 Introduction

The India-based Neutrino Observatory (INO) [46] is an atmospheric neutrino experiment and this experiment focuses to address several physics issues, mainly the precise measurement of the atmospheric neutrino oscillation parameters, to observe the influence of the matter effect on the oscillation phenomena and consequently to calculate the sign of the mass-squared difference (Δm_{23}^2), as explained in details in the previous chapter. To obtain the desired precision in the measured oscillation parameters, a large magnetized Iron Calorimeter (ICAL) is chosen as the main detector for the India-based Neutrino Observatory (INO) experiment. In this chapter we discuss the ICAL detector, the main reasons for choosing such a detector geometry and then discuss the design

and different other components. As mentioned earlier, the active detectors inside the iron calorimeter are Resistive Plate Chambers (RPCs) [49]. In this chapter, we also elaborate the working principles of RPCs.

Atmospheric neutrinos from all directions interact with the iron nucleons inside the iron calorimeter mainly by following channels:

1. In neutral-current (NC) interaction, hadrons are generated through the exchange of Z particles,

$$\nu_\mu + Fe \rightarrow \nu_\mu + X, \tag{2.1}$$

where X represents hadrons. In the above interaction mainly pions are produced, thereby creating the events having hits from hadrons only.

2. During the charged-current (CC) interaction, neutrinos interact weakly through the exchange of a W^+ or W^- boson to form charged particles:

$$\nu_\mu + Fe \rightarrow \mu^- + X, \tag{2.2}$$

$$\bar{\nu}_\mu + Fe \rightarrow \mu^+ + X \tag{2.3}$$

In these interactions events will consist of both muon and hadrons hits.

3. Low energy muon neutrinos undergo quasi-elastic scattering and muon tracks from these interactions dominate over very low energy hadrons. These events therefore contain mainly muon hits.

We can expect a mixture of all the above mentioned processes in INO, after data-taking for a long period. Atmospheric neutrinos cover a wide range of energy starting from a few MeV to hundreds of GeV. The typical flux of atmospheric neutrinos at earth's surface is $\sim 10^{-1} \text{cm}^{-2} \text{s}^{-1}$ [50]. The accuracy in the measured neutrino oscillation parameters rely on larger exposure of data i.e. Kilotons of detector material with

26

multiple years of data-taking and also sophisticated active or passive means to reduce the background.

2.2 The Iron Calorimeter for the INO experiment
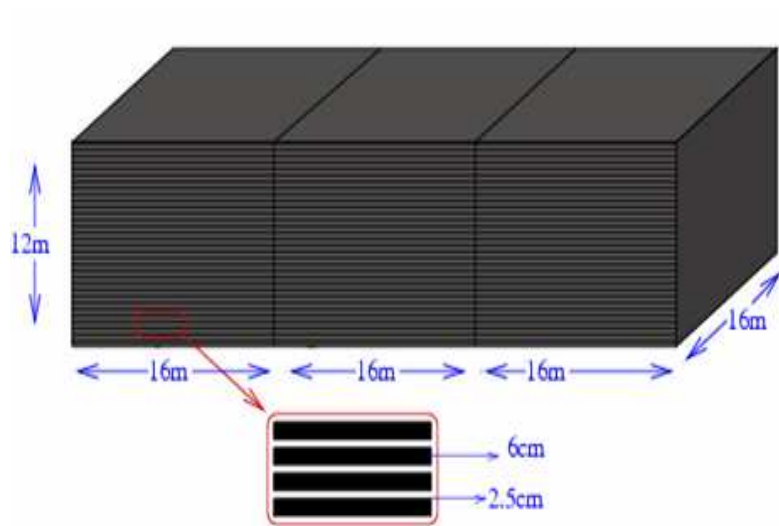
Figure 2.1: Schematic view of the 50 kTon iron calorimeter consisting of 3 modules, each having 140 layers of iron plates.

As mentioned earlier, INO will have a big Iron Calorimeter (ICAL) detector and the main reasons for choosing such a big calorimeter are following:

1. ν interactions are very rare (cross section $\sim 10^{-43} \text{cm}^2$), so to obtain a good statistics of the ν interacting events in a reasonable time-period we need large amount of detector material.

2. Ability to separate the ν and $\bar{\nu}$ events by the identifying the charges of μ^- and μ^+ events produced by the charged-current interaction as per equation 2.2 and equation 2.3 respectively. For better charge-identification, it is required to have a fully-contained track inside the volume of the detector. Charge identification is crucial for studying the matter effects in a three-flavour analysis, as discussed in chapter 1.

3. The iron plates in the calorimeter will be magnetized uniformly with a desired magnetic field intensity of ~ 1.3 T, which will help to identify μ^- and μ^+ events from their opposite bending.

4. A long track inside the calorimeter will help to obtain better energy and angular resolutions for ν events so that the ratio L/E can be measured with better precision. In the ratio, L is the length traversed by the atmospheric ν before interaction and E is the energy of the interacting neutrino event. The sinusoidal L/E dependence of $P(\nu_\mu \rightarrow \nu_\mu)$ will provide the direct evidence from the neutrino oscillation for atmospheric neutrino data.

The ICAL detector as shown schematically in figure 2.1, will consist of three modules each of dimension 16 m × 16 m × 12 m. Each module will contain a stack of 140 horizontal iron plates, each of thickness ~ 6 cm and each iron layer will be inter-spaced with 2.5 cm gap to house the active detectors. The total mass of the detector will be ~ 50 kTon. The specification of all the components of the ICAL detector are mentioned in Table 2.1.

Atmospheric neutrino flux peaks below few GeV energy, and then the flux decreases faster than $1/E^2$. So in the low energy regime the statistics will be higher whereas these events will not contribute significantly to the interesting region where the oscillation

Table 2.1: Specifications of the ICAL detector

ICAL	
No. of modules	3
Module dimension	16m × 16m × 12m
Detector dimension	48m × 16m × 12m
No. of layers/module	140
Thickness of Fe plate	∼ 6 cm
Gap for RPC trays	2.5 cm
Magnetic field	∼ 1.3 Tesla

has a maxima or a minima [46]. Typically, it is assumed that the ICAL detector will be sensitive to the neutrino events with energy larger than 1 GeV.

The INO experiment is designed to estimate the neutrino oscillation parameters precisely. As explained in section 1.1.1 of chapter 1 that the neutrino oscillation [51, 52] is a quantum mechanical phenomenon relying on the superposition principle. Neutrinos can travel from one end of the earth to other end mostly without any interaction, which makes them very difficult to detect. As mentioned earlier, neutrinos interact through the flavor neutrinos $(\nu_e, \nu_\mu, \nu_\tau)$, however they oscillate during their propagation as mass neutrinos (ν_1, ν_2, ν_3). Considering the occurrence of neutrino oscillation, during travel a ν_μ becomes a ν_τ, then back again to ν_μ and the oscillation process continues. The probability of a ν_μ to oscillate into ν_τ after time t is governed by the relation

$$P_{\mu\tau} = \sin^2 2\theta_{32} \sin^2 1.27 \frac{L\Delta m_{32}{}^2}{E} \tag{2.4}$$

Where θ_{32} is the mixing angle and $\Delta m_{32}{}^2 = m_3{}^2 - m_2{}^2$ is the mass-squared difference. So far individual masses of neutrinos are not known, only the values of mass-squared differences are measured and θ_{32} , $\Delta m_{32}{}^2$ are the dominating terms for the atmospheric ν oscillation. The mixing parameters, θ_{ij} are one of the fundamental parameters, that
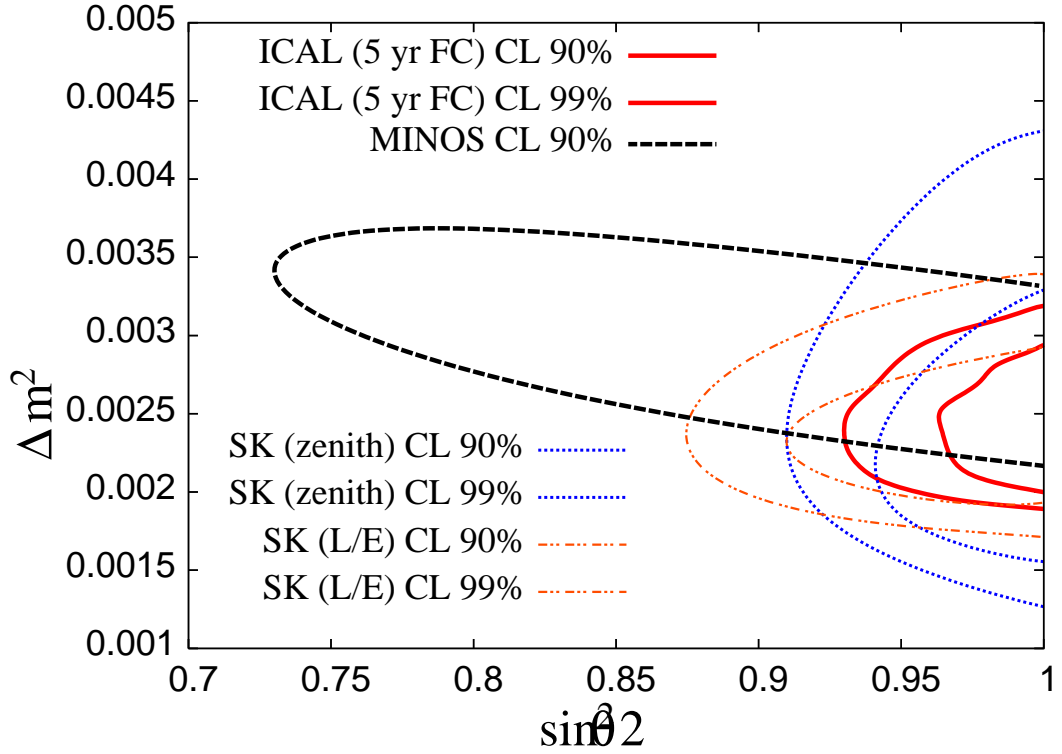
Figure 2.2: The contours at 90% and 99% CL for 5 years fully-contained events from ICAL simulation with $\Delta m^2 = 2.3 \times 10^{-3} \text{eV}^2$ and comparison with the contours obtained from other experiments (adopted from Ref. [53]).

could constrain theories beyond the standard model of the particle physics. Therefore, it is very important to measure the $\sin^2 2\theta_{32}$ as accurate as possible. The precisions on the measurements of $\sin^2 2\theta$ and $|\Delta m|^2$ for 5 years fully contained ICAL data are compared with the results obtained from the Super-K [22] and the MINOS experiments [54], shown in figure 2.2. Here contour plots at 90% and 99% CL in $\Delta m^2 - \sin^2 2\theta$ plane are shown and the ICAL data is compared with the Super-K (1489 days data) and the MINOS data [53]. For the case of Super-K two different analysis is performed, one with respect to zenith angle and other with respect to zenith angle. It is expected that the ICAL will have marginally better sensitivity to the measured parameters than that of the MINOS experiment and substantially better than those of Super-K.
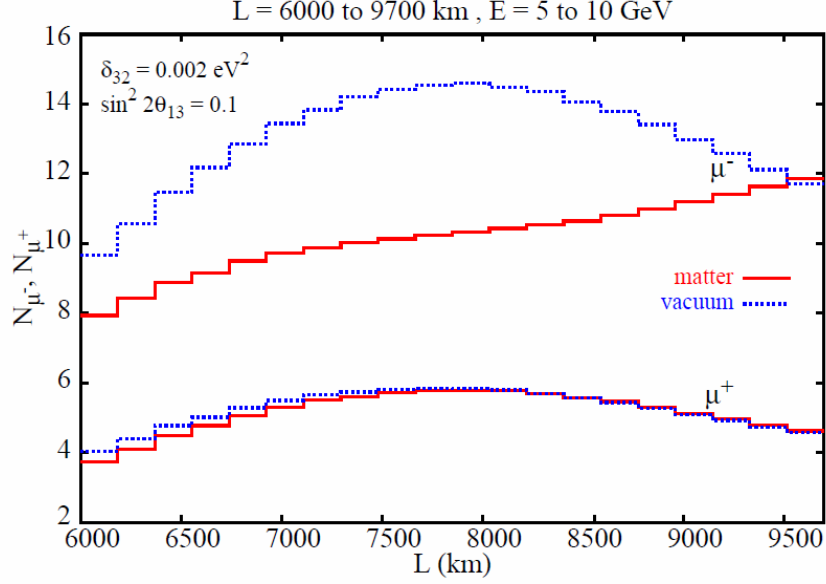
Figure 2.3: Total number of μ^+ and μ^- events in presence of vacuum and matter at different distances (L) for a positive Δm^2_{32}, taken from [46].

The simulated statistics of μ^+ and μ^- events inside the ICAL detector generated due to $\bar{\nu}_\mu$ and ν_μ as per equation 2.2 and 2.3 for 1000 kton-years exposure is shown in figure 2.3. Here the events considered are for the energy range of 5-10 GeV and L range of 6000-9700 km. Since ν_μ and $\bar{\nu}_\mu$ oscillates differently in matter, hence μ^- and μ^+ will respond differently. It is shown in figure 2.3 that for the L range of 6000-9700 km and for positive Δm^2_{32} i.e. for $m_3 > m_2$, the matter dependent μ^- events rate is noticeably smaller than the vacuum rate, whereas μ^+ events rates are similar. For negative Δm^2_{32} i.e. for $m_3 < m_2$, μ^- events rate are identical for vacuum and matter, however different for μ^+ events. The details are available in Ref. [46]. Hence in ICAL data, there will be a scope of solving the hierarchy problem i.e., whether neutrinos follow normal ($m_3 > m_2$) or inverted ($m_2 < m_3$) hierarchy. This hierarchy issue is one of the main physics goals of the INO experiment.
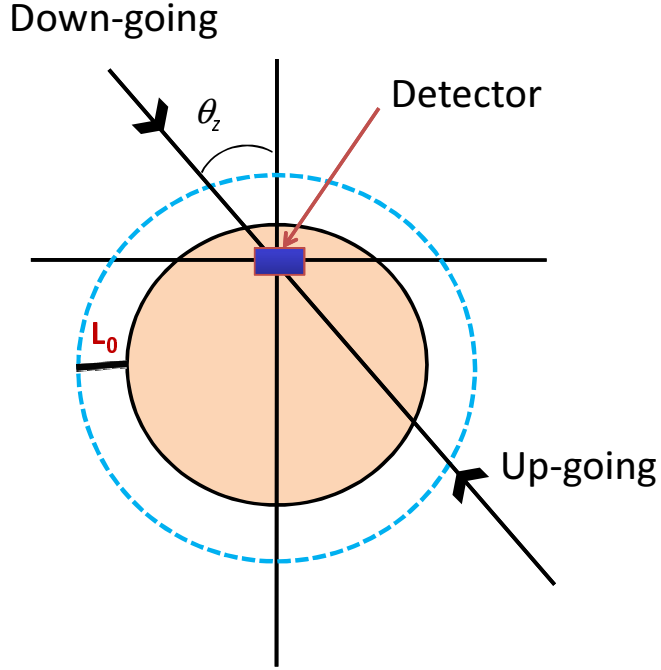
Figure 2.4: Schematic showing the up-coming and down-going neutrino directions and the path length L associated with the zenith angle θ_z.

To obtain the oscillation probability for given values of θ_{32} and $\Delta m_{32}{}^2$, one needs to evaluate the L/E ratio, as in equation 2.4. Where L is the length traversed by the atmospheric ν before interaction and E is the energy of the incident ν event. When a neutrino falls on the detector, it makes an angle θ_z with the normal to the earth, as shown in figure 2.4 and this angle is known as the *zenith angle*. The direction θ_z of the ν event can be measured from the direction of the muon event generated due to the ν_μ charge-current interaction and L can be estimated from measured θ_z values by the following relation

$$L = \sqrt{(R + L_0)^2 - (R \sin \theta_z)^2} - R \cos \theta_z \tag{2.5}$$

Where L_0 (~ 15 km) is the average height above the surface of the earth at which the atmospheric neutrinos are generated and R is the radius of the earth. Whereas the energy E of the ν event can be estimated by measuring the energy of the muon and hadrons produced by ν interaction with the iron nuclei.

If neutrinos oscillate, then there will be a discrepancy between the number of up-coming and down-going νs events, because up-coming neutrinos traverse larger distance inside the earth before they are detected, as shown in figure 2.4. The reference path length L for down-going neutrinos is associated with the up-going neutrinos by transforming $\theta_z \leftrightarrow (180-\theta_z)$ so that the range of L/E remains the same for up-going and down-going neutrinos [55]. The ratio of up-going and down-going events will have a dependence on the L/E ratio due to the neutrino oscillation, according to the equation 2.4. The Up/Down events vs L/E distribution is shown in figure 2.5 for 5-years ICAL simulated data. Therefore to observe the oscillation pattern the energy E and the direction θ of the incoming ν have to be measured accurately for every event. For precise estimation of the distance (L) traversed by the neutrino before interaction inside the iron calorimeter (as per equation 2.2 and 2.3), it is necessary to identify the direction of flight(θ) (i.e. whether up or down) of the produced muon tracks with high accuracy. The measurement of θ alone can not determine unambiguously whether the event is up-coming or down-going, for that additional information of the time of detection of the entire event is required. An active detector with a time resolution of 2ns or better can identify the direction of the track i.e. can provide desired up-down discrimination. The active detector needs to have a spatial resolution < 1 cm for better identification of hits positions of the muon tracks because the accurate measurement of the hit positions or the hit co-ordinates are essential to obtain the trajectory of the produced particle i.e., the muon track.
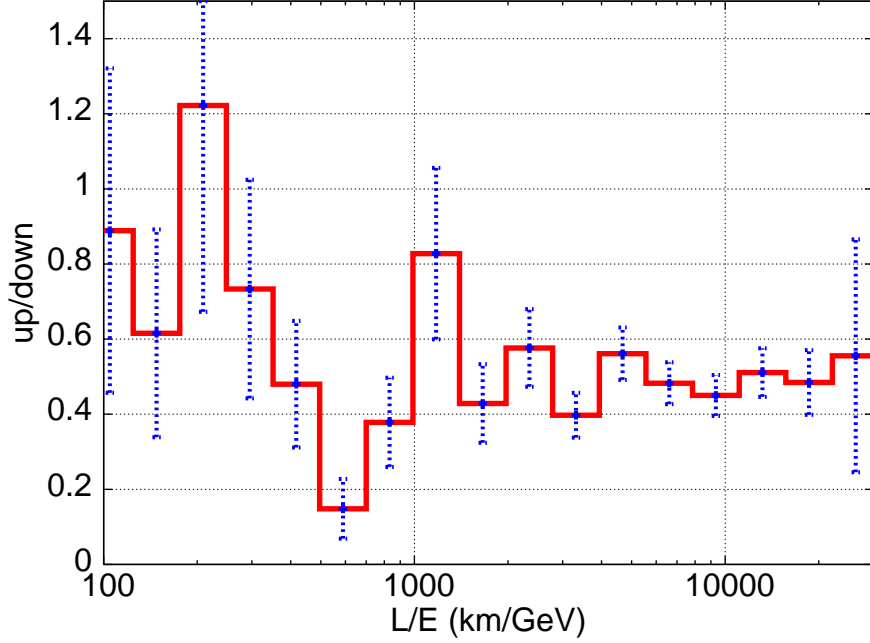
Figure 2.5: The ratio of the up-coming and down-going neutrino events as a function of L/E obtained from the ICAL simulation, for 5 years of FC events with $\Delta m^2 = 2.3 \times 10^{-3}\text{eV}^2$ (taken from Ref [46]).

2.3   RPC : The active detector for ICAL

Considering the better time and position resolutions together as the key factors, the Resistive Plate Chambers (RPCs) [49] are chosen as the active detectors for the INO experiment. The RPCs will be sandwiched between the pairs of iron layers and the signal i.e., the hits generated by the produced charged particle will be obtained by the readout strips or pads. The iron layers in the ICAL detector will be separated from its' successive layers by iron spacers and the spacers will be placed at every 2m interval along the X-direction and this will create 2m wide roads along the Y-direction for inserting RPCs inside the gap between two iron layers. So, for each module of 16m length, there will be 8 such roads in a layer. The dimension of each RPC will be 2m
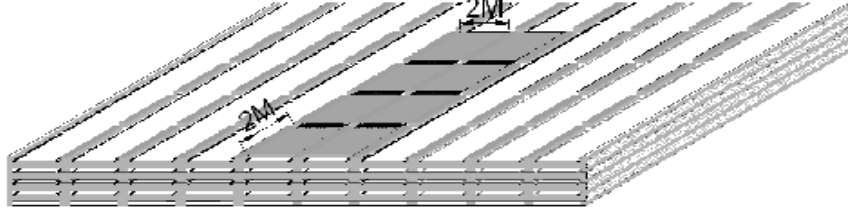
Figure 2.6: Schematic showing the placement of RPCs inside the ICAL detector, taken from Ref [46].

long and 2m wide. Hence there will be eight such RPC units in a road of dimension 16m × 2m, as shown in figure 2.6.

So inside the gap between two iron layers there will be 64 RPC units for each detector module and a total of ∼27,000 active detectors will be inside the whole volume of the ICAL detector. All the details about the required number of roads, RPCs etc. inside the ICAL detector are listed in Table 2.2.

Table 2.2: Specifications of the RPCs to be placed inside the ICAL detector

RPC	
RPC unit dimension	2m × 2m
Readout strip width	3 cm
No. of RPC units/Road/Layer	8
No. of Roads/Layer/Module	8
No. of RPC units/Layer	192
Total no. of RPC units	∼ 27,000
No. of electronics readout channels	3.6×10^6

2.4 Working principle of RPCs

The Resistive Plate Chamber (RPC) was first developed by R. Santonico and R. Cardaralli in 1981 [49]. RPC is a gas detector made of two highly resistive parallel electrodes of resistivity$\sim 10^{10} - 10^{12}$ Ω − cm. The internal structure of a RPC is shown in
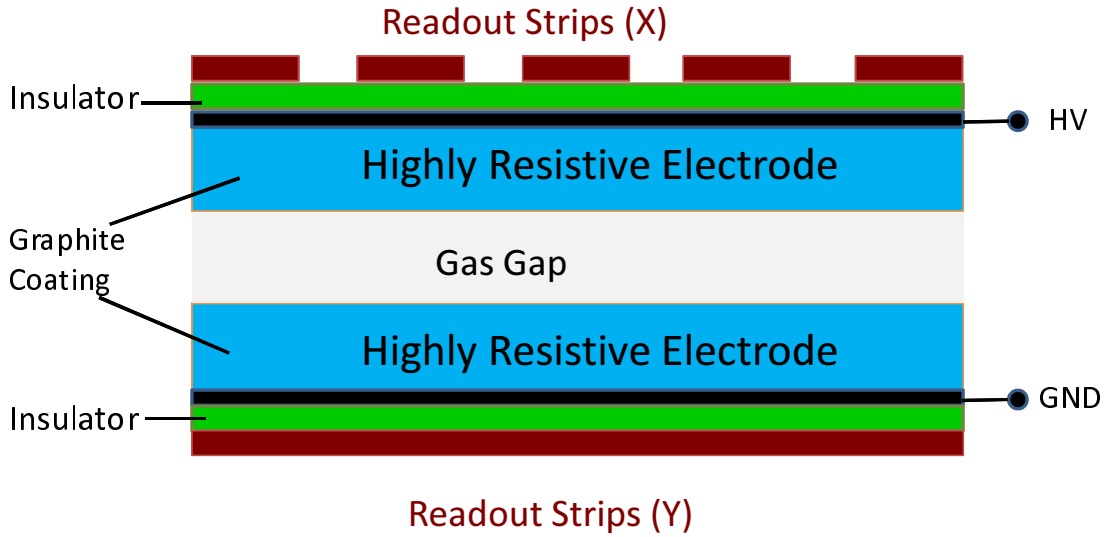
Figure 2.7: The internal structure of a RPC module.

detector, the particle 'decomposes' its' charge exponentially by:

$$Q = Q_0 e^{-t/\tau} \quad \text{with } \tau = \rho \varepsilon_0 \varepsilon_{\mathrm{r}} \tag{2.6}$$

where ρ is the volume resistivity of the material, ε_0 is the dielectric constant and ε_r is the relative permittivity of the electrode material. In general, the glass electrode has the volume resistivity of $\rho \approx 10^{12} \Omega$ − cm, giving the 'relaxation time' $\tau \approx 1s$, whereas the volume resistivity of bakelite is of the order of $\rho \approx 10^{10} \Omega$ − cm, i.e., $\tau \approx 10 ms$. The ionized charges in the resistive electrodes cause high voltage across the electrodes

and thus the electric field in the gas gap drops locally around the initial avalanche or discharge. As a consequence, the detector remains dead for each avalanche for a time of the order of relaxation time, however rest of the detector area remains sensitive to incident charge particles. After the relaxation time, the region get back to the original situation by obtaining charges from the power supply.

As shown in figure 2.7, the resistive electrodes/plates are painted with graphite coating of surface resistivity typically in the range 200-300 $k\Omega/\square$ and due to this coating the high voltage gets distributed over the electrode surfaces. The readout strips of the RPC are the orthogonal pickup strips placed over the entire area of the chamber along X and Y directions on both sides of the gas gap. The strips remain separated from the graphite coating by an insulating material. RPC operates in two different modes, avalanche mode [56] and streamer mode [57]. The main difference between these two modes of operation is the amplitude of pulse/signal from the detector.

2.4.1 Avalanche mode of operation of RPCs

In avalanche mode [58], the incident charged particles create primary ionization by interacting with the given gas molecules inside the detector and this primary ionization process is followed by the propagation and multiplication of the charges in presence of the electric field across the electrodes. The avalanche development is governed by the Townsend and attachment coefficients [59]. At a large gas gain the avalanche charges influence the electric field of the detector and also their own propagation and multiplication process, this phenomenon is called the space charge effect due to the avalanche. Due to the space charge, the electric field inside the detector deteriorates, details is discussed in chapter 6. The avalanche development inside a RPC is shown schematically in figure 2.8. The unwanted thing in the avalanche mode of operation
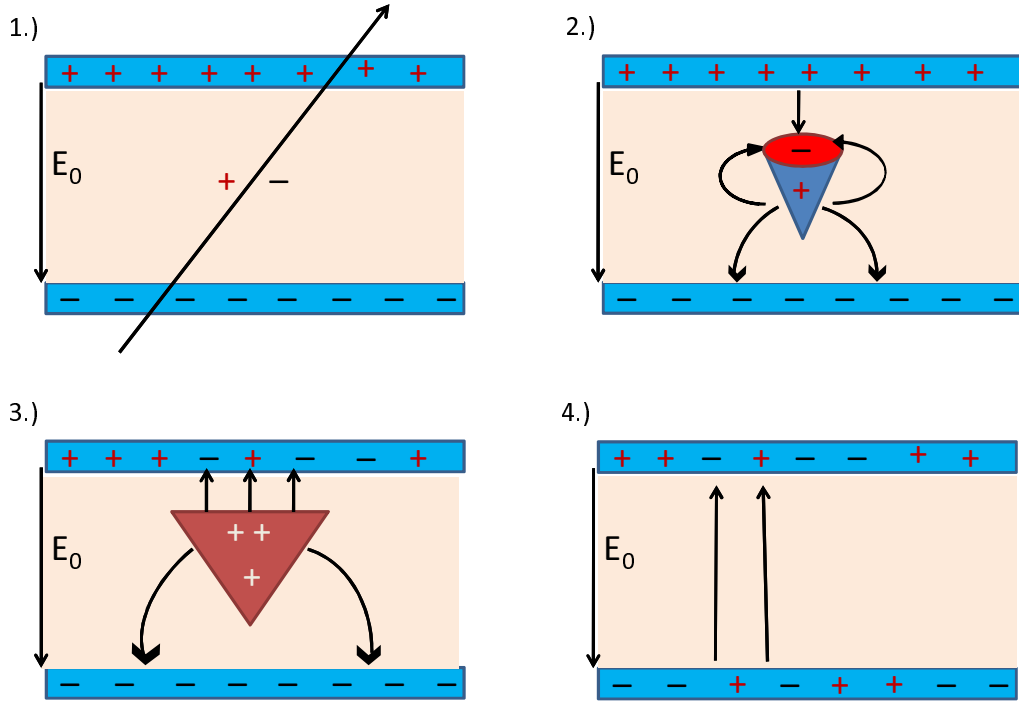
Figure 2.8: The avalanche growth inside RPC is shown schematically. E_0 is the applied electric field across the electrodes. (1)When a charged particle passes through the detector, primary ionization occurs, (2)Avalanche multiplication of the primary electrons and the avalanche electrons affect the electric field E_0, (3) The electrons reach the anode much faster than the ions as ions have much slower drift velocity, and (4) Finally the ions reach the cathode. So the charges in the resistive layers influence the electric field around the small area where the avalanche was developed.

of RPCs is the formation of streamer or discharge (discussed in the next subsection) and if the streamer is suppressed and RPC is allowed to operate in avalanche mode then the rate capability improves considerably upto few kHz/cm^2. This is achieved by adding SF_6 in small percentage to the gas mixture inside the gas gap [57]. However in avalanche mode the average size of the charge pulse is lower by a factor of ten than that

of the streamer pulse, so extra preamplifier is required during the readout of output signal. RPC electrodes made of bakelite i.e. the bakelite RPCs can be operated both in avalanche and streamer mode whereas the glass RPCs works only in avalanche mode, because streamer i.e. discharge etches the glass surface and damages the glass RPCs.

2.4.2 Streamer mode of operation of RPCs

When the gas gain increases beyond the space charge effect, then photons start contributing in the process of avalanche propagation, and the streamers appear [57, 60]. After that a conductive channel is created between the two electrodes and through this channel the electrode surfaces are discharged. A localized streamer discharge due to the passage of charged particles will induce pulses on the appropriate strips, however discharges may also create spark sometimes. The growth of the streamers inside the RPC is shown schematically in figure 2.9. The streamers form comparatively larger current signal than the avalanche pulses and typical size of streamer pulses are 50pC to few nC. So for the RPCs operated in streamer mode no preamplifier is needed and the signal can be discriminated directly. Hence the readout system of streamer RPCs is simpler than that of avalanche RPCs. However the rate capability is limited within few hundred Hz/cm^2.

There are two different designs of RPCs: the Trigger RPC and the Timing RPC. The schematic of a 2mm thick single gap trigger RPC is shown in figure 2.10. Typically the gas mixture used for trigger RPC working in avalanche mode, is $C_2F_4H_2$, $i - C_4H_{10}$, SF_6 in $96.7 : 3 : 0.3$ ratio and the operating voltage is 10 kV due to an electric field of 50kV/cm across the gas gap(s). The electrodes are made of 2mm thick glass or bakelite plates. Typically for RPCs operating in avalanche mode, the efficiency$\sim 98\%$ with time resolution$\sim 1 - 2$ns are obtained. Whereas for timing
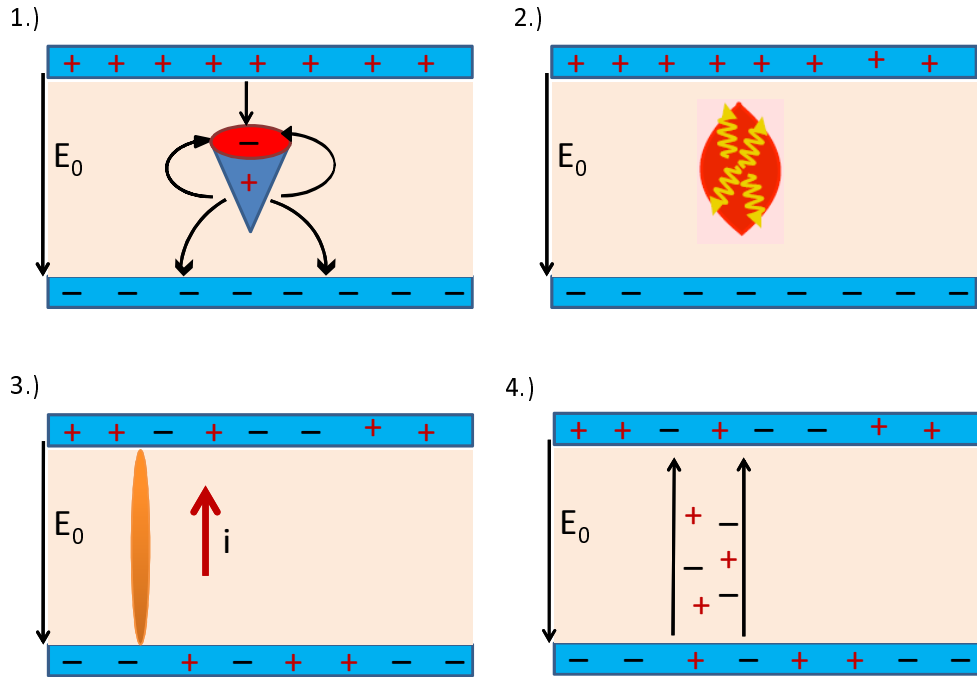
Figure 2.9: The schematic of the development of streamer inside a RPC. (1)The avalanche formation as discussed in figure 2.8, (2) a large gas gain or avalanche deteriorates the field E_0 and photons start to contribute to the avalanche and streamers are created, (3) a weak spark may be generated and a small area over the electrodes get discharged, (4) the electric field surrounding the avalanche is decreased drastically and the certain portion of the detector remains dead for each incident particle.

RPCs the gap thickness is $0.2mm-0.3mm$ and the electric field around the electrodes is $100kV/cm$ are used. For timing RPCs, the gas mixture used is $C_2F_4H_2$, $i-C_4H_{10}$, SF_6 in $85:5:10$ ratio. For timing RPCs the efficiency is $\sim 99\%$ and time resolution is of order of 50ps i.e., much better than the trigger RPCs operating in avalanche mode. Trigger RPCs can also be operational in streamer mode, which gives $> 90\%$ efficiency and $\sim 2\ |rmns$ time resolution.
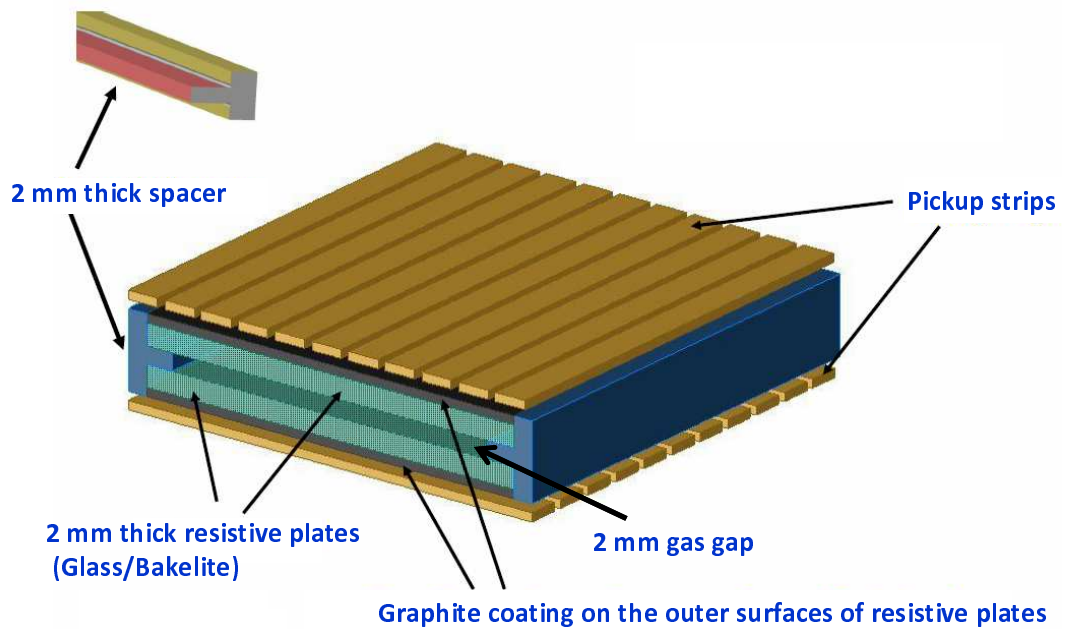
Figure 2.10: The schematic representing the structure of a single gap trigger RPC.

For ICAL, trigger RPCs will be used where the requirement of 2ns time resolution can be met. Trigger RPCs are also easy to built. Two parallel developments are performed on RPCs for ICAL. While glass RPCs are operated in avalanche mode, bakelite RPCs can be used in streamer mode. Both types of RPCs provide $> 95\%$ efficiency for a long period of operation and with time resolution ~ 2ns, thereby satisfying the requirements of INO. In chapter 6, we have discussed in detail about the Monte Carlo code developed for simulating the response of a RPC operating in avalanche mode.

Chapter 3

ICAL prototype detector and the response simulation

3.1 Introduction

As a first step towards building the iron calorimeter (ICAL) for the INO experiment [46], a prototype detector having a structure similar to that of ICAL has been installed at VECC, Kolkata. The justifications for building and testing an ICAL prototype are listed below:

1. The geometrical structure of the prototype is similar to that of the 50kTon ICAL detector, with scaled down dimension. The prototype consists of a stack of magnetized iron layers interlaced with position sensitive RPC gas detectors. In case of the main ICAL, only the dimension and the number of iron layers are larger.

2. The setup will be used to test the prototype RPCs, each of dimension 1m × 1m. RPCs of 2m × 2m will be used in the main ICAL.

3. The experience gained from the operation of this prototype detector will help us to test the RPCs as well as to debug their design philosophy.

4. The extensive testing of RPCs can be performed and the environmental effects can be studied.

5. The codes and procedures for data reconstruction can be applied to the prototype data and can be extended/used in ICAL data analysis.

6. Data-set taken over a very long period will be useful to study the properties like flux and momentum distribution of cosmic muons among other physics observable.

7. The facility can be utilized to test other tracking detectors in a magnetic field.

3.2   INO ICAL Prototype Detector

This prototype is of $\sim$ 35 ton weight, which is about $1/1000^{th}$ in weight of the 50 kTon ICAL detector. Two pictures of the prototype laboratory, where the magnet is installed is shown in figure 3.1. The prototype detector consists of 13-layers of iron plates, each having dimension of 2.5 m$\times$2.2 m$\times$5 cm, and provide an effective magnetic field of $\sim$ 1.0 T in the central region of 1.0 m^2 area. The current-carrying coils pass perpendicularly through the iron plates, as shown schematically in figure 3.2. A steel box of $\sim$ 2.0 cm width with 3.0 m $\times$ 3.0 m dimension and filled with concrete, is installed as the base plate on a specially made concrete platform. The iron plates are subsequently mounted one after the other using cranes. A complete iron layer is built by joining together two smaller C and T shaped plates, and the current carrying coils pass through the gap between the C and T shaped plates on each plane. A dedicated power supply is used to supply currents upto 500 Amp., which provides a maximum

Figure 3.1: Left Panel: The INO iron calorimeter prototype detector at VECC. Right Panel: Six RPCs placed inside the iron layers, four of them are glass RPCs and other two are bakelite RPCs.

field of 1 Tesla. Chilled low conductivity water (LCW) is circulated through the core of the tube carrying the conducting coil to reduce the heating effect. The magnet power supply has interlock arrangement such that it can be protected against the rise in coil temperature. Each iron layer is 5.0 cm thick and inter-spaced with 5.0 cm gap as shown in figure 3.1. It is designed such that a set of 12 Resistive Plate Chambers (RPCs) [49], having dimensions of 1.0 m × 1.0 m each will be placed in between the iron layers at the central region. This prototype is planned to be used for tracking cosmic muons by taking data over a long period of time for good statistics. Experience gathered from the operation of this prototype detector will be extremely useful for future planning and installation of the INO detector. As a part of the R&D effort, we are working on RPCs with two types of electrodes, one made of glass and other made of bakelite. The glass RPCs are operated in avalanche mode and the bakelite RPCs are operated in streamer mode thereby producing larger signal. The readout electronics is based on reading out the signal in triggered mode, where triggers are generated by the time-coincidence of the signals from two scintillators placed at the top and bottom of the magnet and/or by
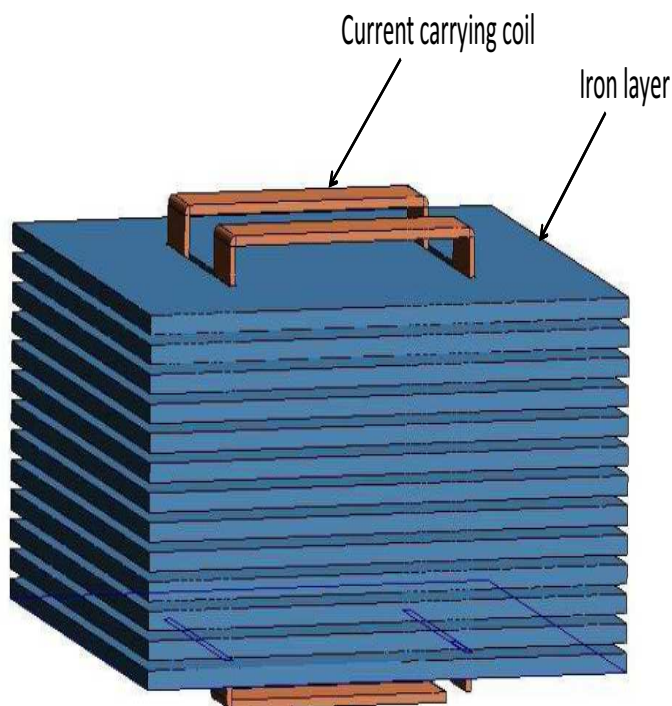
Figure 3.2: The schematic showing the coil carrying current to magnetize the iron layers inside the prototype detector volume.

making coincidences of signals from two or more RPC strips. Triggers can be generated by combining various "folds" i.e., various combinations of RPC strips and planes. The prototype detector uses a CAMAC-based data acquisition system (DAQ). The RPCs with the DAQ system is shown in figure 3.3. It should be noted that for the glass RPCs working in avalanche mode pre-amplifiers are required. However for bakelite RPCs, pre-amplifiers are not required because the signal amplitude is comparatively larger in streamer mode than the signal of glass RPCs operating in avalanche mode. The timing measurements coupled with the strip co-ordinates will provide the location of the cosmic hit. Two dedicated gas distribution systems [61] are installed in the laboratory as the gas compositions for streamer and avalanche modes of operation are
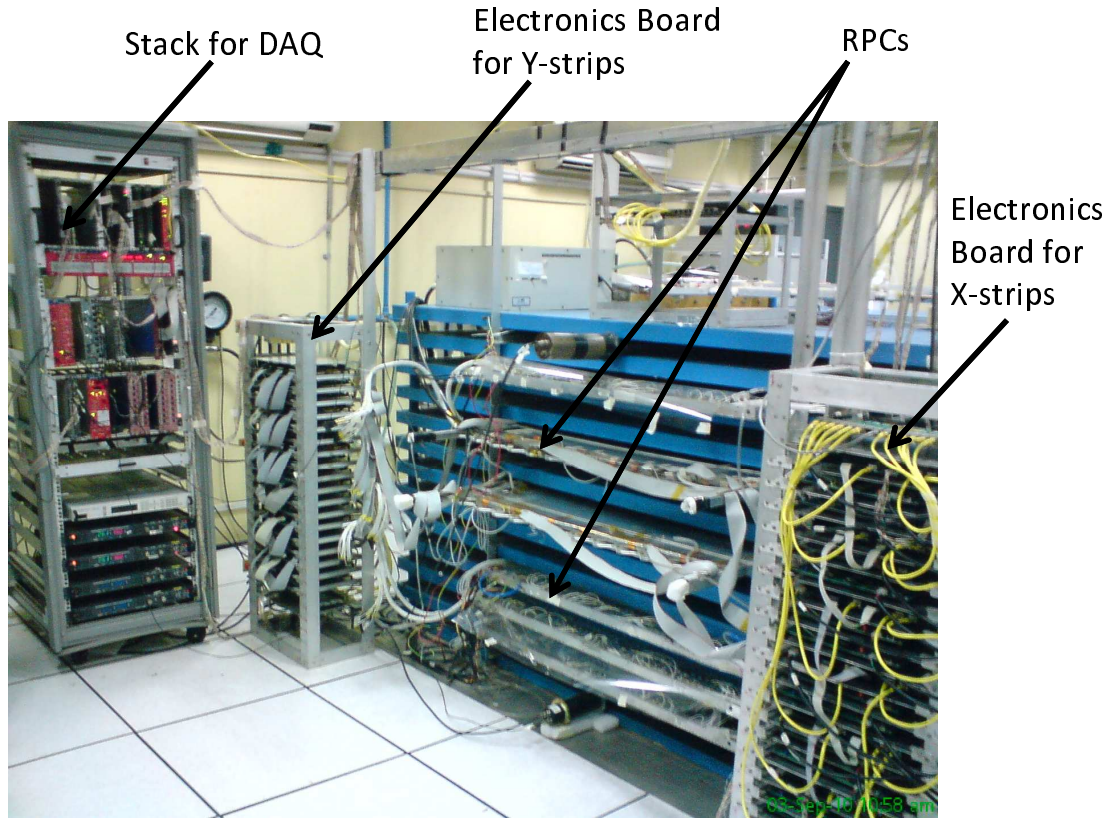
Figure 3.3: The RPCs and electronics stack in the prototype Lab.

different. A dehumidifier is installed along with the air conditioning units to provide consistent temperature of $22^{o}C$ and relative humidity <55%.

3.3 Operation of the prototype detector

Recently four glass RPCs and two bakelite RPCs, each of dimension $1.0 \text{ m} \times 1.0 \text{ m}$ have been installed in six RPC-slots and the corresponding DAQ and readout electronics are commissioned in the laboratory. The glass RPCs are operated in avalanche mode with a gas mixture of tetrafluroethane (R-134a) and isobutane in 94.77 : 5.3 volume
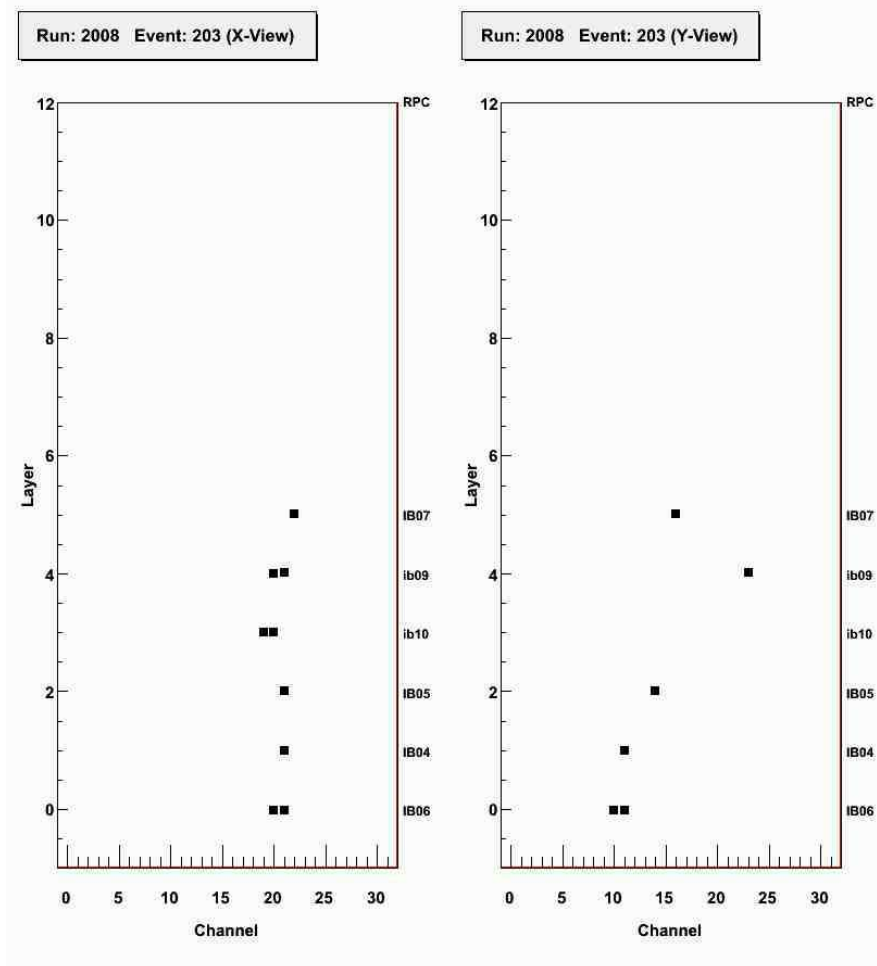
Figure 3.4: Cosmic muon track for Run No. 2008 and Event No.203. X & Y views of the hits as recorded by strips are shown.

mixing ratio whereas the bakelite RPCs are operated in streamer mode with a mixture of $Ar, R - 134a, i - C_4H_{10}$ gases in volume ratio of $55 : 37.5 : 7.5$. Pickup strips each of $3cm \times 1m$ dimension are placed perpendicular to each other, over top and bottom surfaces of the RPCs i.e., there are 32 strips along each of the X&Y-directions on both the surfaces of a $1m \times 1m$ RPC. Hence, there are 64 read out channels for each RPC. The data acquisition system is designed to generate the trigger depending on the hit
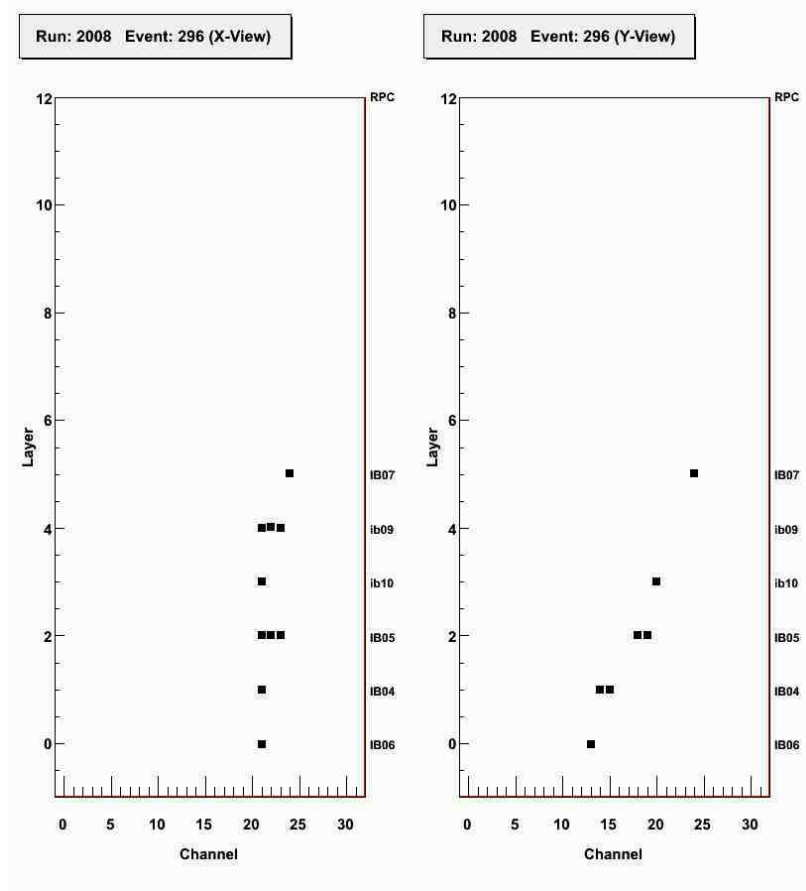
Figure 3.5: Cosmic muon track for Run No. 2008 and Event No.296.

pattern on the RPC pickup strips and to record strip hit patterns together with the timing information of the generated hits with reference to the trigger time. One of the important tasks of the online data acquisition system is to monitor the stability of the detectors and also to supervise the laboratory ambient parameters, like temperature, relative humidity and barometric pressure etc. The signal readout system for glass RPCs consists of fast high gain preamplifiers and low level threshold discriminator followed by the digital back-end. A photograph showing the installed electronics and DAQ is shown in figure 3.3. All the details about the electronics, data acquisition system and the gas mixing and distribution system are discussed in Ref [62].

48

Two cosmic muon tracks of Event No. 203 and Event No. 296 recorded from Run No. 2008 are shown in figure 3.4 & figure 3.5 respectively. In these figures the signature of the cosmic muon trajectory is shown both in x-z plane (X-view) and y-z plane (Y-view), where Z represents the direction of the incident particles. The magnet was not switched on for these events and the trigger was based on time coincidence of two scintillators placed at the top and bottom of the magnet which were overlapping the positions of the strips being readout in an event. Here, IB04, IB05, IB06, and IB07 represent the glass RPCs whereas ib09 and ib10 are for the bakelite RPCs. Sometimes more than one hits appear on a detector plane e.g., in figure 3.5 for the X-view, there are three hit points for IB05 RPC. These hits are likely to be generated due to crosstalk inside the RPC the detector.

3.4 Simulation of the prototype detector using GEANT4

We have simulated the response of the ICAL prototype detector by using the object-oriented "detector description and simulation tool", called GEANT4 [63] and cosmic muons are considered as input particles.

3.4.1 GEANT4: A detector simulation tool-kit

GEANT4 is a publicly available detector simulation package based on the object-oriented programming framework using C++ language. Basically, GEANT4 is a geometry modeler which provides a list of particles with associated properties and their interactions by different physics processes and their corresponding cross sections. The user has to define the detector geometry of own choice by specifying the material and
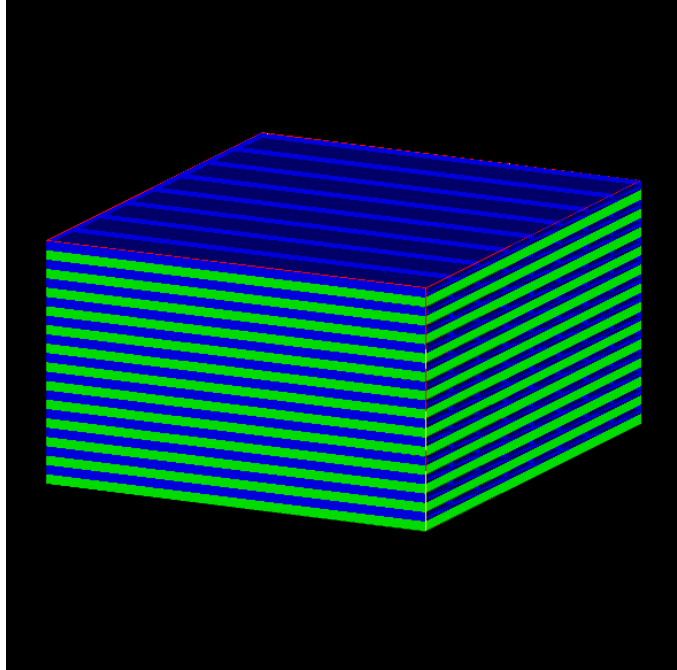
Figure 3.6: Geometry of the simulated prototype detector volume.

also assign the components of the detector which will generate signal i.e., the sensitive detector and attributes required to compute the signal. There is an interface to the event generators for simulating input particles. The information needed to be stored for further analysis e.g., energy deposition provided by GEANT4 can be converted into a detector signal.

3.4.2 Results

We have used GEANT4 to simulate the geometry of the prototype discussed in section 3.2 and also analyzed the response of the detector. While simulating the geometry we have incorporated all the details of RPC detector components (e.g., electrodes material, gas mixture components, pickup strips material among others). The simulated detector volume is shown in figure 3.6.

The simulated prototype detector [64] volume consists of 13 iron layers, which are stacked along the z-direction and the pick-up strips are placed along the x and y-directions inside the gap, as shown in figure 3.7. The simulated iron layers are magnetized uniformly along the y-direction with 1 T magnetic field. The gas volume of 2 mm thickness consisting of $Ar, C_2F_4H_2$, $i - C_4H_{10}$ gases and Cu pick-up strips each of 1.0 m $\times$ 3.0 cm size are placed on both sides of each RPC gas volume and considered as sensitive strips for collecting signal. Hence, on each side (above and below orthogonally) of the 1.0 m $\times$ 1.0 m RPC electrodes there are such 32 pick-up strips. It should be mentioned that even though actual area of the iron layers in the prototype is $\sim$ 2m $\times$ 2m, in this simulation we have considered the 1m $\times$ 1m region which is supposed to have uniform magnetic field.

The sensitive regions are the gas chambers in the RPCs, and as mentioned above the transverse size of the sensitive regions are 3cm each in the x and y directions, i.e., the spatial resolution of the detector in the x and y directions are determined by 3cm wide strip. The energy deposition on a strip is considered as the signal for further analysis in simulation. The charged particle triggers the RPC by the energy it loses inside the medium and registers a *hit*. For this detector simulation, the response of the RPC and the associated electronics are not incorporated. The simulation of RPC response is performed separately and discussed in chapter 6. As mentioned earlier, the prototype detector is not underground, so it is expected that we will only able to track cosmic muons in this detector. GEANT4 also simulates the response of the prototype detector when muon events traverse through it.

When single muons are incident along the z-axis, a clear signature of bending is visible in presence of the magnetic field, as shown in figure 3.7. From figure 3.8, it is visible that the μ^+ and μ^- events show opposite bending inside the simulated prototype detector volume. The INO ICAL prototype will therefore be able to identify charges of
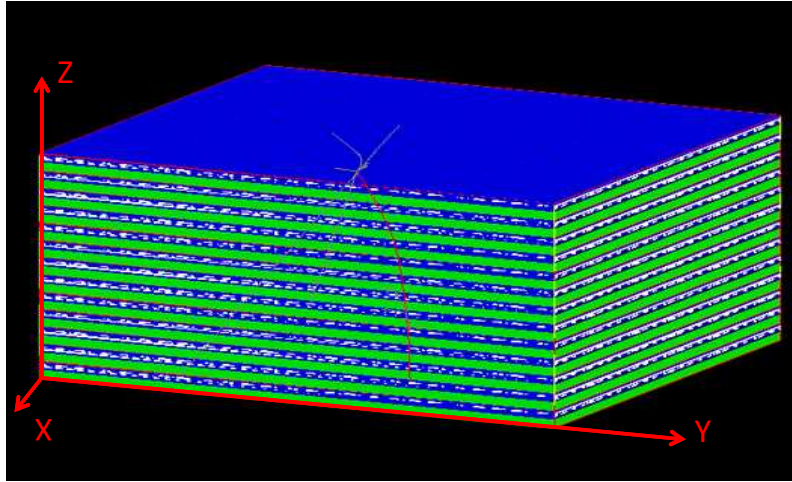
Figure 3.7: Simulated prototype detector response while muon passing through it.
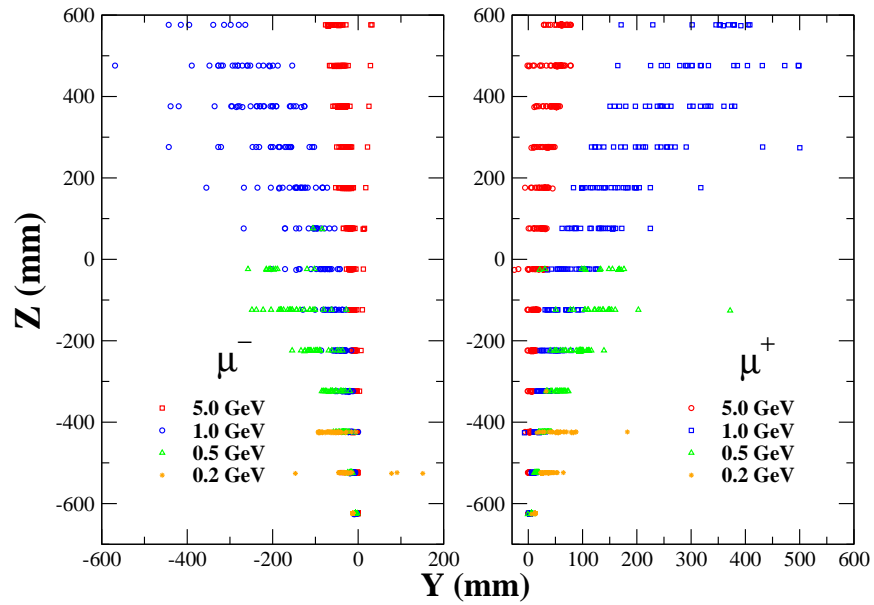
Figure 3.8: Opposite bending of μ^+ and μ^- events of different energy inside the detector magnetized with 1 T field.

the cosmic muons from the bending in presence of the desired magnetic field of 1.0 T over a maximum track length of about 1.3m. From figure 3.8, it can also be observed that the bending of track has an energy dependence, low energy muon tracks bend more than those of the higher energy particles.

The muon events with energy > 1.0 GeV have almost straight line trajectory shown by the red squares in figure 3.8 and these events are partially contained (PC) events, the events whose vertices are within the fiducial volume but whose tracks are not completely contained in the detector volume. So it is expected that for higher energy PC events the resolution of the reconstructed momentum will be worse compared to that of the low energy fully contained (FC) events. Because the track fitting method
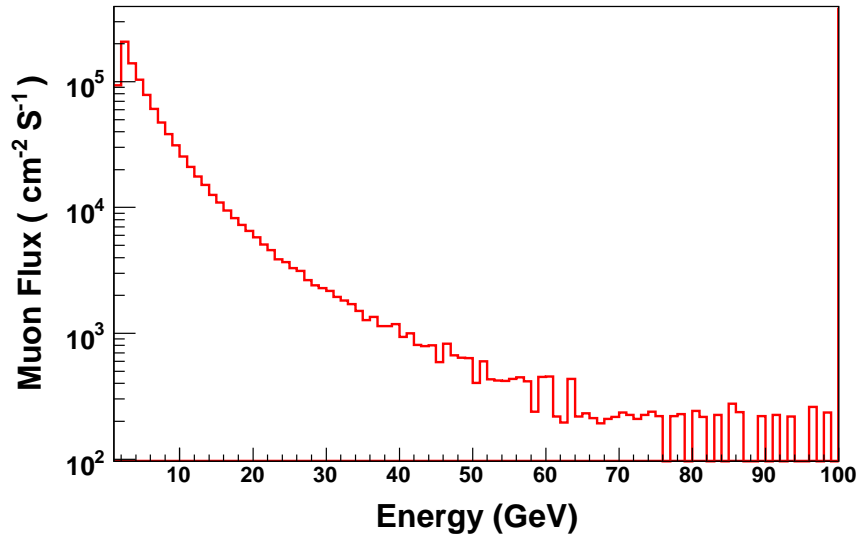
Figure 3.9: Energy distribution of cosmic muon flux on the Earth surface.

(discussed in chapter 5) we have developed, utilizes the entire track length for fitting, and such method is relatively more useful to reconstruct the momentum of the fully contained (FC) events, the events whose tracks finished within the detector volume. For the prototype detector muons events having energy $\lesssim 1.1$GeV are fully contained.

We have simulated the response of the cosmic muon flux as available on earth's surface.
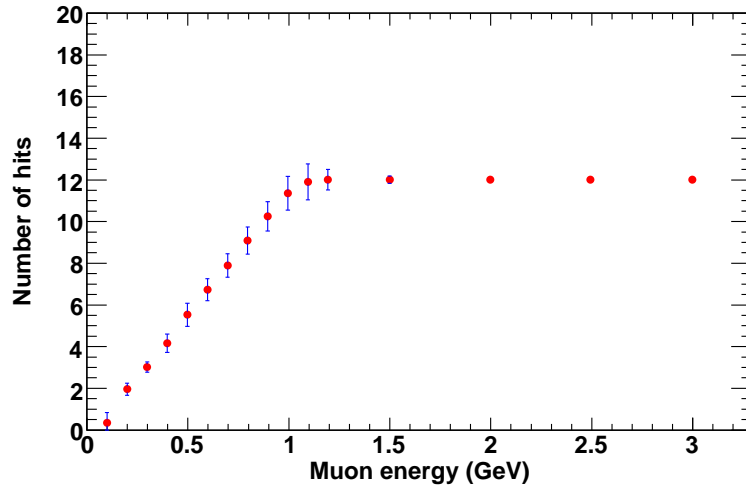
Figure 3.10: Energy dependence of hit multiplicity of the incident muons. As muons affect mostly one layer, number of hits in this figure represents number of layers muons pass through before getting stopped completely or escaping the prototype detector. Bars represent the RMS of the distribution and at higher energies bars are inside the symbol.

The energy spectrum of the cosmic muon flux on the earth's surface [65] is shown in figure 3.9 and this flux distribution is used as the incident particles on the prototype detector volume. However, for further analysis we have considered the energy range of 0.5 GeV to 2.0 GeV. Interaction of the incident particles with the detector material and energy deposited in the pickup strip of the RPC is termed as a 'hit'. It is expected that the low energy particles will leave shorter track inside the detector compared to those by the high energy particles. In this discussion, a track is the trajectory of a charged particle inside the calorimeter volume. Variation of the average number of detector layers (5cm thick) traversed by muons of varying energies is shown in figure 3.10
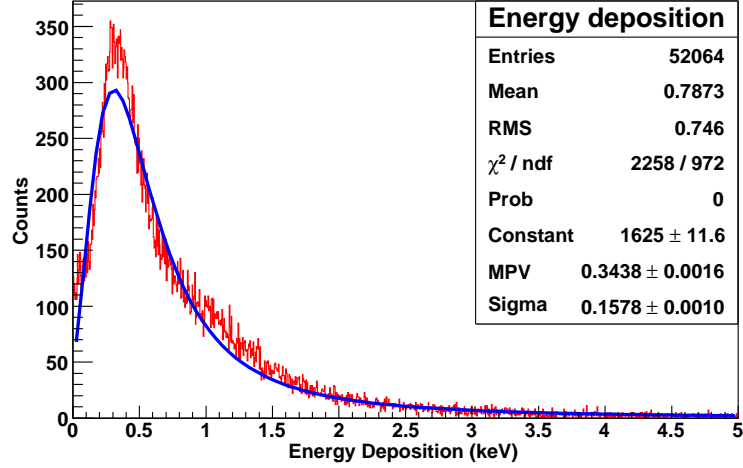
Figure 3.11: The distribution of energy deposition by muons in 12 RPC layers. The energy deposition spectrum is fitted with the Landau distribution function.

and we termed it as hit multiplicity. It is observed that the number of hits increases linearly with the energy of the incident particles, thereby suggesting the applicability of a procedure of muon momentum measurement by the number of layers traversed by a track i.e., from the length of the track. During the propagation of muons through the iron calorimeter, energies get deposited both inside the iron layers as well as inside the gas layers of RPCs. As the signal is collected in the form of energy deposition inside the active detector, so we have studied the energy deposition inside RPC layers in details.

Figure 3.11 shows the spectra for energy deposition inside gas layers of all 12 RPCs in the calorimeter, by cosmic muons as per the flux distribution given in figure 3.9. Muon energy depositions in the gas volume follow Landau distribution with most probable value (MPV) of ~ 0.34keV and mean of ~ 1keV. These values match the estimations of energy deposition inside a 2mm gas volume, by the Bethe-Bloch formula [66]. In figure 3.12, the energy depositions by muons at different RPC layers are plotted. As
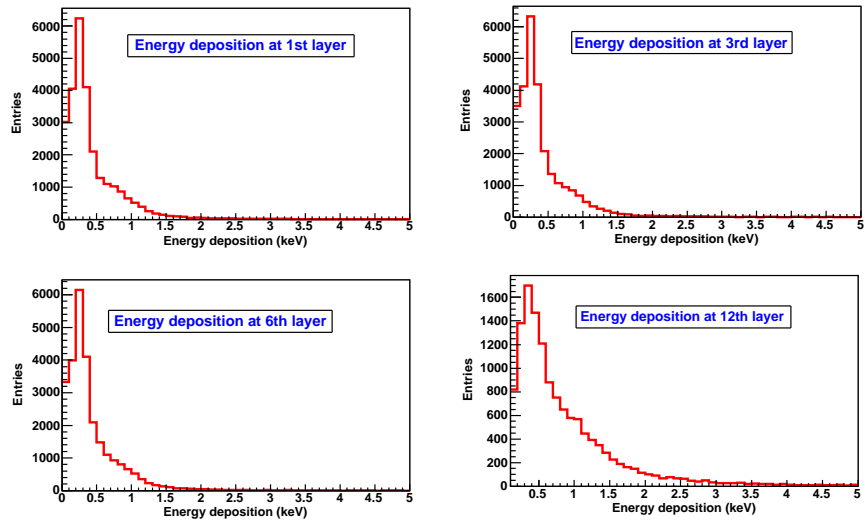
Figure 3.12: Spectra of energy deposition at different RPC layers for 1GeV muons.
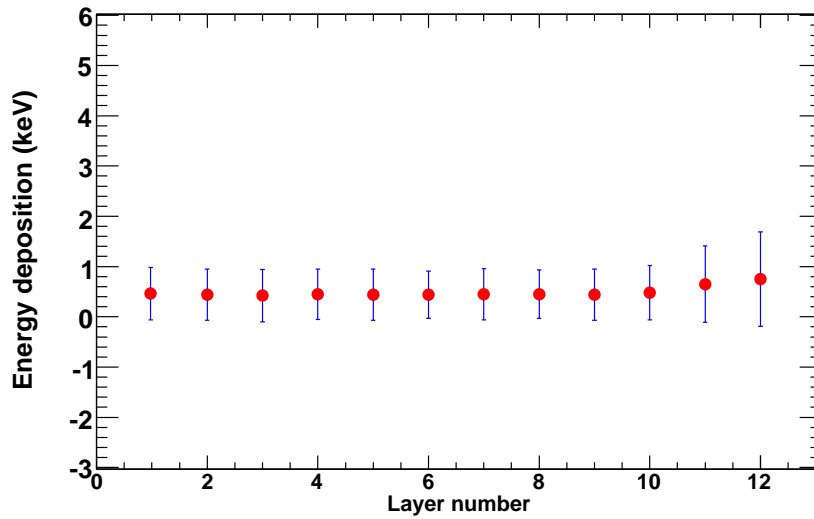
Figure 3.13: Average energy deposited by the cosmic muons at 12 RPC layers. Layer number 1 represents the layer at the bottom and this is the 1st layer hit by incident muon. Bars represent the RMS of the distribution.

expected energy deposition at different layers (e.g. $1^{st}, 3^{rd}, 6^{th}$ and 12th) have similar distributions. Layer-wise average energy depositions by cosmic muons in all the 12 RPCs are shown in figure 3.13 and this distribution is obtained for the statistics of 10000 muon events of 1GeV energy.

In the next step of the study, we have varied the energy of incident muons and it is observed that while traversing different detector layers, cosmic muons deposit similar amount of energy in each layer. Hence the average energy depositions appear indepen-
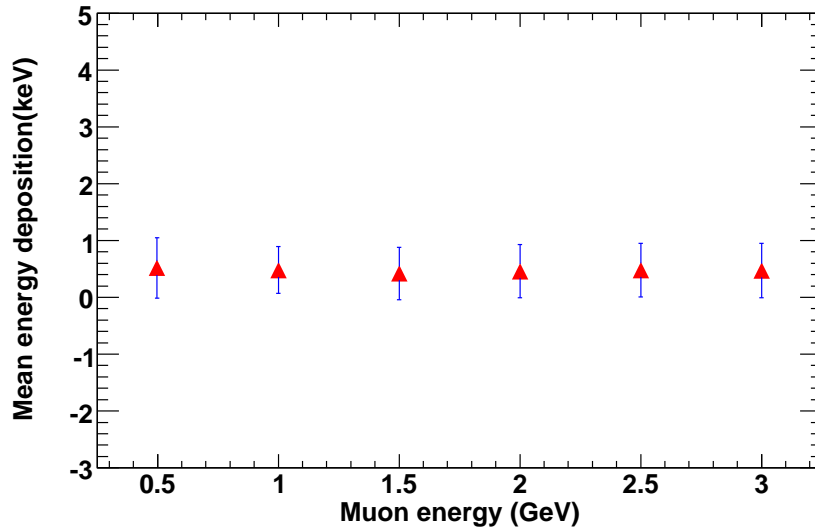
Figure 3.14: Mean energy deposited inside 12 RPC layers by muons of varying energy. In this figure mean represents the mean of the Landau distribution and the bars represent the spread of the distribution.

dent of the energy of interacting muons, as shown in figure 3.14. We have also studied the response of pions in the prototype detector. Figure 3.15 depicts the distribution of average number of hits by muons and pions in 12 RPCs. It is observed that muons leave on an average one hit over 10 layers whereas pions loose all it's energy after traversing 3-4 layers. Here 'hit' represents number of interactions inside one RPC strip of area
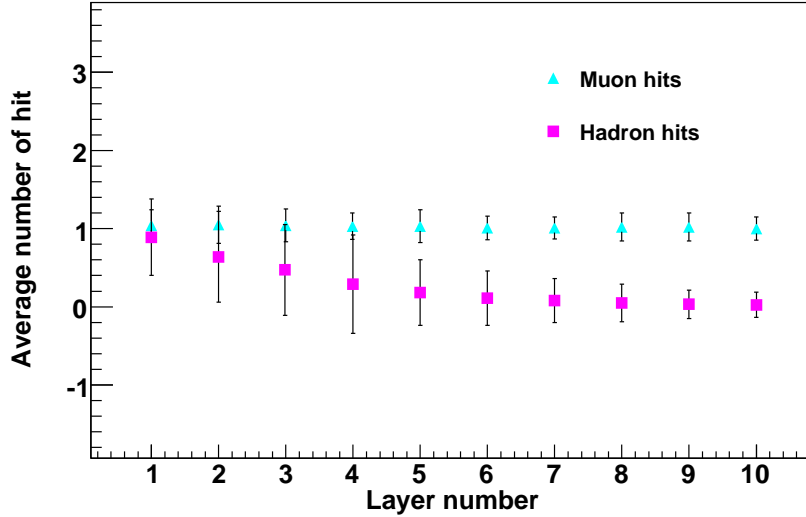
Figure 3.15: Distribution for average number of hits left by 1GeV muons and 1GeV pions at different RPC layers. Bars represent the RMS of the distribution.

3cm × 1m in a particular detector layer. More precisely a particle will have multiple hits in a layer (say, layer 1), only if the particle fires more than one RPC strips on both x&y-directions.

3.5 Summary and Conclusions

A prototype calorimeter having geometry similar to that of the ICAL detector of the INO experiment has been installed at VECC, Kolkata. This prototype consists of 13 magnetized iron layers, keeping a provision of installing 12 RPCs inside the gaps between the iron layers. The prototype has started collecting data where four glass RPCs and two bakelite RPCs have been installed. In this work we have implemented the geometry of the detector by GEANT4 simulation tool-kit and analyzed the response of the detector to the cosmic muon flux on earth's surface. Energy deposition by

cosmic muons on RPC layers has been studied. The dependence of energy deposition on different interacting detector layers and also on energy of incident muons have been analyzed. It is observed that the energy deposition spectra is MIP-like and remains almost independent of the incident energy and positions of the layers. This property can be used to estimate muon momentum by counting the number of layers it passes through before depositing entire energy inside the detector volume. It is also observed that both 1GeV muon and 1GeV pion have different hits spectra inside the RPCs and this discrimination in hit pattern can be utilized to separate out muons from the hadrons.

Chapter 4

Discrimination of muons and hadrons inside the INO Iron Calorimeter using the artificial neural network

4.1   Introduction

In calorimetric measurements of neutrino interactions, produced muon and hadron hits on a detector layer poses a challenge in identifying muon hits for reconstruction of muon tracks. An algorithm based on the method of Artificial Neural Network (ANN) is developed to separate out the muon hits from the hadron hits. One of the main goals of the atmospheric neutrino experiments is to study the neutrino oscillation phenomena by precise measurements of the oscillation parameters. These parameters can be extracted by reconstructing the neutrino interaction events [46] in a calorimeter. In INO, the

incident neutrino energy (E) and the total path (L) traversed by the neutrino before interaction are used to obtain an event variable (L/E) for studying the oscillation parameters. The neutrino oscillation probability is given as follows:

$$P_{\mu\tau} = \sin^2 2\theta_{32} \sin^2 1.27 \frac{L\Delta m_{32}{}^2}{E} \tag{4.1}$$

Hence the sinusoidal L/E dependence of the survival probability i.e., $P(\nu_\mu \to \nu_\mu)$ can provide the compelling evidence of neutrino oscillations. The mixing parameters θ_{ij} and the sign of Δm^2, are the fundamental parameters that could constraint theories beyond the standard model. Precise measurement of these quantities is therefore a pre-requisite for extracting the physics variables.

Neutrinos interact with the iron nucleons inside calorimeter mainly by the following channels:

1. In neutral-current (NC) interaction, hadrons are generated through the exchange of Z particles,

$$\nu_\mu + Fe \to \nu_\mu + X \tag{4.2}$$

   In the above interaction mainly pions are generated, thereby creating events with hadron hits only.

2. During charged-current (CC) interaction, neutrinos interact weakly through the exchange of a W^+ or W^- boson to form charged particles:

$$\nu_\mu + Fe \to \mu^- + X \tag{4.3}$$

   The events in this case will consist of both muon and hadrons hits.

3. Low energy muon neutrinos undergo quasi-elastic scattering and muon tracks from this interaction dominate over very low energy hadrons. So, in this case an event consists of mainly muon hits.

Neutrino interactions are rare, therefore proper procedures need to be adopted for identifying the reaction channel in an event. From a collection of events accumulated by the calorimeter, it is necessary to make use of the suitable selection criteria for (a) separating muon-rich events from hadron events and (b) then in the next step, separating muon hits from hadron hits for CC events given by equation 4.3. Separation of hits is essential for proper reconstruction of muon track parameters. In this study, therefore we make use of the characteristics of muon and hadron for separating one from the other. Since the energy of the interacting neutrino can be reconstructed by summing the energies of muons and hadrons. Similarly the direction of parent neutrino can be deduced from that of muon, while its particle type (i.e., whether ν or $\bar{\nu}$) can be determined from the curvature of the track of produced muon in the CC interaction in the presence of magnetic field.

Muons being minimum ionizing particles(MIP), usually produce one hit per layer which can then be connected to form a long track and the track parameters e.g., momentum, direction can be extracted by using sophisticated procedures like Kalman Filter technique [67]. On the other hand, hadrons get absorbed inside the detector after traversing first few layers. However, complexities arise for cases like (a) muons generating larger number of hits due to processes like multiple scattering and (b) events containing both muons and hadrons and creating hits mixed together in each layer. The degree of complexity in separating muon and hadron events or identifying the origin of a hit depends on the level of track intermixing. Out of the above two cases, case (b) is more complex in terms of separating the origin of hits.

Neutrino experiments are dealing with the issue of particle discrimination for decades. For example, the NEMO experiment [68] is designed to study the double-beta decay in search for the majorana neutrino and here, the Cellular Automata [69] algorithm is utilized for muon track searching [70]. Similarly for Neutrino Factory (NuFact) [13],

a large magnetized iron calorimeter is considered as the detector and the neutrino interactions in such a detector will have signatures similar to those from INO. The ν-factory beam will contain $\bar{\nu}_\mu(\nu_\mu)$, by accelerating μ^+ in a muon storage ring,

$$\mu^+ \rightarrow e^+ \nu_e \bar{\nu}_\mu \qquad (4.4)$$

and if ν_e oscillates into ν_μ, then that ν_μ will produce μ^- after CC interaction, remaining $\bar{\nu}_\mu$ will generate μ^+. Hence the presence of μ^- in the detector will provide a clear signature of neutrino oscillation. As a consequence the observation of wrong sign muon events will provide the opportunity to measure θ_{13}, the sign of Δm_{23}^2, CP violation and matter effects as well. As described in Ref. [71], about 99.2 % muons from ν_μ CC events at 50 GeV are to be separated out. It is seen that at a distance of about 10 cm from the interaction vertex, hadron showers have their peaks whereas muons traverse more than 100 cm. However, it could not distinguish short muon tracks from the hadronic shower. MONOLITH [72] was a proposed atmospheric neutrino experiment which also had the same iron calorimeter detector geometry like INO and an analysis of the performance of the MONOLITH prototype [73] shows a good degree of separation between the muon track and the hadronic shower. In this experiment, this discrimination is performed by angular resolution measurement. It is reported in [73] that the hadron showers should have an average energy resolution of the order of $100\%/\sqrt{E}(\text{GeV})$, for a full reconstruction of the energy and direction of interacting neutrinos. While parameterizing the shower axis reconstruction and angular resolution, MINOS [74] parameters are used. The angular resolution θ_0 is calculated by [71]:

$$\theta_0 = \frac{A}{\sqrt{E}} + \frac{B}{E} \qquad (4.5)$$

where θ_0 is the r.m.s of the angular resolution in degrees and E is the shower energy in GeV, whereas A and B are the parameters taken from the MINOS experiment.

Apart from these neutrino interaction experiments, many other high energy physics experiments also adopted the procedure of using absorbers for stoping hadrons and muons are identified by tracking chambers. Recently a paper [75] on the Magnetized Iron Neutrino Detector (MIND) also discusses some useful approaches for muon and hadron energy reconstruction. The 50 kTon MIND detector has similar configuration as the INO ICAL detector. For muon experiments [76], where tracking is performed by sampling inside the absorber, separation of muon and hadron hits at every detector layer is of extreme importance. In this article we have applied the method of Artificial Neural Network (ANN) on simulated data for performing the above mentioned separation.

In next section, we discuss the basics of ANN in brief, section 4.3 describes the analysis procedure on simulated data including the implementation of ANN method for our purpose, in section 4.4 results are presented. The implications of the results in the detection of atmospheric neutrinos are described in section 4.5.

4.2   Artificial Neural Network

The artificial Neural Network (ANN) [77, 78] is a widely used technique in the field of machine learning, especially for pattern recognition. The method is inspired by the human brain's architecture of interconnected neuron cells and mimic its learning processes. ANN is an approach of supervised training of nodes with a set of trained patterns and the pattern parameters obtained from the training step are applied to the unknown samples for selecting the desired patterns. The nodes in ANN are set up in analogy to the human neurons. Like in human neuron system, in this case as well, suitable input patterns with best possible discriminatory properties are used for training. One of the advantages of ANN over conventional methods is that, in
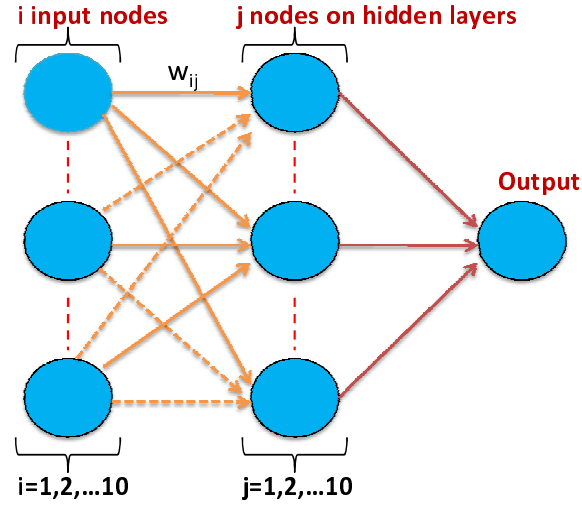
Figure 4.1: Architecture of the artificial neural network as implemented.

ANN, all possible inputs with uncorrelated discriminatory attributes can be utilized simultaneously for achieving the best possible result. In ANN, inputs are not applied sequentially and therefore the signal detection efficiency does not decrease. In feed forward neural network method, known as Multilayer Perceptron (MLP) algorithm, one or more layers are constructed in between the input layers representing a given pattern and the output layer with one or more target values. These layers in between are known as hidden layers, where the patterns are distributed over several nodes in a layer. Figure 4.1 shows the schematic representation of the feed forward ANN with one hidden layer. Each of the input and hidden layers consist of 10 nodes, and the output layer has one node. As indicated in figure 4.1, neuron inputs to a layer are linear combinations of the neuron outputs of the previous layer. For a given neuron j in layer k, we have the equation

$$x_k{}^j = A\left(w_{0j}^k + \sum_{i=1}^{M_{k-1}} w_{ij}^k . x_i{}^{k-1}\right), \tag{4.6}$$

65

where $x_i{}^{k-1}(i = 1, 2, ..., M_{k-1})$ represents the input signal from the previous layer $(k-1)$, M_{k-1} is the total number of neurons in layer $k-1$, w_{ij}^k represents the synaptic weights of neuron j, the bias term w_{0j}^k is acquired by adding a new synapse to neuron j whose input is $x_{0j}^{k-1} = 1$. A represents the activation function. For the present work, we used the sigmoid function of the form

$$A(x) = \frac{1}{1 + e^{-x}}, \tag{4.7}$$

as the activation function. In the procedure of training, the ANN involves minimization of error given by:

$$E = \frac{1}{N_p} \sum_{p=1}^{N_p} (O^p - t^p)^2, \tag{4.8}$$

where p denotes a pattern and O^p is the output obtained for that pattern with the target output t^p and N_p is the total number of training patterns. The weights obtained from this supervised learning can then be applied to an unknown pattern which gives an output that can then be related to a pattern. Various methods are applied for minimization.

A complete neural network therefore consists of multiple layers of neurons. The "input layer" takes the dataset on which the classification task has to be performed. In the case of a face recognition problem, for example, this could be the pixel-by-pixel information of a camera image or derived quantities, such as the ratio of height and width of the image. There will be one neuron for each input variable. The "output layer" consists of neurons for the different categories, corresponding to the different possible outcome of the classification. In the example of the face recognition problem, there would be one neuron for each person to be recognized. After the layout of the network architecture is chosen which also includes the number of hidden layers, the network has to be trained with events whose pattern or class is known. In the example of face pattern recognition problem, this would be done with a selection of photographs

of the people to be recognized. Training is an iterative process. In each step, the neural network assigns a class to the trained events. By comparing the assigned class to the true class or pattern for all events, an overall classification error for the neural network is calculated. Then the weights of the individual neurons are adjusted and the whole process is repeated. The weights are varied until the classification error reaches a minimum and the optimal weight for a particular set of pattern is obtained.

ANN has been used extensively for both online and offline pattern recognition in various fields. In the field of high energy physics, ANN is utilized for extracting photons from a mixture hadrons in a preshower detector [79] and also for identifying jets in high energy collision events [80]. In this work, we have used the publicly available code JETNET3.4 [81] for the implementation of the network. The inputs to the network are the Monte Carlo simulated data, which are the detector response of a simulated ICAL detector volume, discussed in the next section.

4.3 Analysis Procedure

In this section we describe the simulation procedure , which includes a brief description of the geometry simulation of the INO ICAL detector and its response to muon and hadron events. In the next subsection we describe the variables used as inputs to the neural network procedure and finally in subsection 4.3.3, we mentioned about the application of ANN method for the discrimination.

4.3.1 Detector response simulation

The response of ICAL is simulated using GEANT3.21 [82], a detector simulation package where 140 layers of iron are placed in an effective magnetic field of 1.0 T. Each

pairs of 6.0 cm thick iron layers is inter-spaced with a 2.5 cm gap. The active detectors in ICAL, the Resistive Plate Chambers (RPCs) [49] having dimensions of 2.0 m × 2.0 m and consisting of two glass electrodes and a gas mixture of $C_2F_4H_2$, $i - C_4H_{10}$, SF_6 in between, are placed inside the gap. The readout strips each of dimension 2 m × 2 cm are placed perpendicular to each other on two outer surfaces of the RPC electrodes for reading out signals in two dimensions. In this simulation, energy deposition in a gas volume inside RPC detectors above a threshold is considered as a hit. A detailed description about the simulated INO ICAL detector is given in Ref. [53]. An event generator called NUANCE [83] has been used to produce particles from neutrino interactions inside detector materials. To study the ICAL detector response, the GEANT3.21 code is used. The information about the vertex positions and the momenta of the product particles obtained from NUANCE are incorporated as input to the GEANT code.

Event generation by NUANCE

The NUANCE event generator is used to generate neutrino interaction events. The HONDA flux [84] for atmospheric neutrinos has been incorporated in the simulation. In the generator, there is a provision of choosing distribution of neutrino fluxes and also to turn on a 3-flavour mixing from the source to detection point, apart from providing the relevant interaction cross sections. As mentioned earlier neutrino interactions depend on the density of scatterers in the medium. A simplified ICAL detector geometry i.e., a unit cell consisting of iron and glass have been encoded in the NUANCE for providing medium parameters. The main CC interactions of neutrinos with detector materials are quasi-elastic (QE) and resonance (RS) interactions at low energies (upto a few GeV) and deep-inelastic scattering (DIS) at higher energies. CC interactions produce associated lepton of interacting neutrinos and the DIS events usually produce
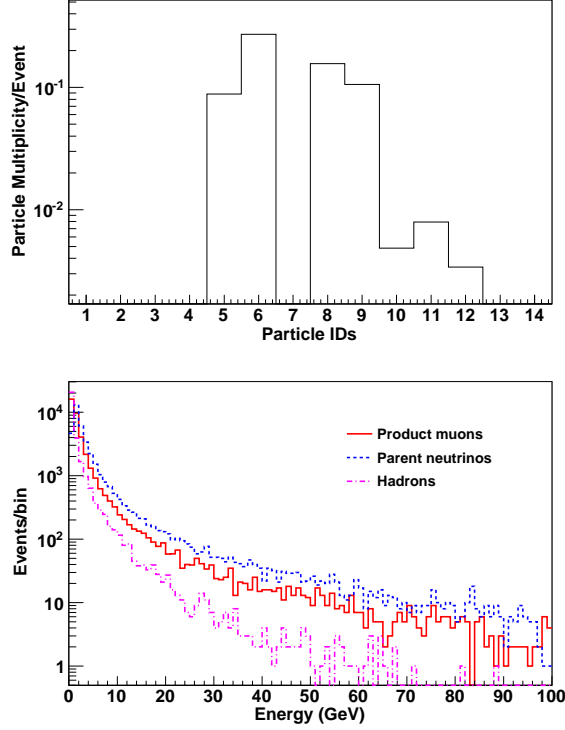
Figure 4.2: Top Panel: Particle multiplicity distribution as provided by NUANCE event generator due to CC interaction of neutrino events. Bottom Panel: Energy distributions of parent neutrinos and their product muons, and pions as simulated from NUANCE.

a large number of accompanying hadrons (mostly pions). On the otherhand, resonance interactions generate mostly one pion along with hadron. The NUANCE output are fed to the GEANT code. Figure 4.2 (top) shows the average multiplicities of various particles (given by particle-id, according to GEANT3 convention e.g., 5,6 for μ^+, μ^- and 8,9 for pions respectively) produced from charged-current interaction of ν events as simulated by NUANCE. The energy distribution of product muons and hadrons generated from muon-neutrino CC interactions is shown in figure 4.2 (bottom). there

is a strong correlation between the product muons and parent neutrinos as the muons carry substantial amount of energy of the parent neutrinos.

In this work, we have studied the response of the ANN algorithm, first by using inputs from the single particle muons/hadrons and later NUANCE generated neutrino interaction events are used as inputs. The simulated hits are obtained from every layer of the calorimeter for the inputs of single particle muons and hadrons of varying energies. However for this study, as discussed later hits from the first 10 detector layers starting from the interaction vertex are considered as inputs to the network. Two sets of mixed-events inputs are generated, (a) event-level mixing, where a collection of events consisting of muons and hadrons are chosen in a random sequence. The collection of these type of events is termed as 'Category-I' input. In other case, (b) for hit-level mixing, where hits from muon and hadron events are mixed to form a new event such that the mixed event contains both types of hits. These events correspond to the CC events and are termed as 'Category-II' input. Events of two different categories are incorporated as input to the network; first one has muon and hadron events mixed in event-level and secondly, muon and hadron hits are mixed in an event i.e. hit-level mixing. A collection of such events simulate neutrino interaction inside the calorimeter i.e., a mixture of CC and NC events. These two collection of mixed events are used as inputs to ANN for this study at single particle level.

4.3.2 Inputs to ANN

The basic criterion for selecting inputs to ANN (i.e., x_i^{k-1} as in equation 4.6) is to utilize the best possible discriminatory properties between muons and hadrons. The property which has been used in this study is that, muons while passing through the calorimeter layers deposit energy equivalent to MIP thus generating mostly one

hit/layer for large number of detector layers, however hadrons deposit most of its energy in first few layers. It is also important that the inputs corresponding to a particular type of particle (muon or hadron) should be uncorrelated. Keeping these criteria in mind, we have selected *number of hits in a layer* (N_{hit}^m) as input (where m stands for 1 to 10 successive calorimeter layers) to the network. N_{hit}^m values in the first 10 layers subsequent to the vertex layer are used mainly to reduce the computational time and it is also observed that first 10 layers can provide best separation. The point of interaction of the neutrino with iron layer is considered as the vertex and its coordinate is chosen as the origin (0,0,0).

As discussed earlier, we have divided the job of discrimination in two categories, (a) separating muon-rich events (CC events) from a collection of mixed single particle events i.e., event-level separation for Category-I input and (b) isolating the muon hits from the hadron hits in a CC event i.e., hit-level separation for Category-II input. N_{hit}^m as mentioned above is obtained differently for two cases. For event-level separation i.e., for Category-I input N_{hit}^m has been chosen as the total hit multiplicity in every layer. Whereas for hit-level separation i.e., for Category-II input N_{hit}^m is the number of hits inside a circular region around the candidate hit to be identified, as illustrated in figure 4.3. Figure 4.4 (left and right panel) show the layerwise distribution of average N_{hit}^m for Category-I and Category-II inputs respectively. In these plots each point corresponds to N_{hit}^m averaged over a large number of events at a particular layer and the vertical bar at every point represents the RMS spread on N_{hit}^m. As seen from the figure 4.4 (left panel), hadrons are mostly absorbed in first few layers and muons continue to generate on an average one hit/layer for all 10 layers. In the figure 4.4 (right panel), where N_{hit}^m are obtained from the hit-level mixing and the RMS spread N_{hit}^m at each layer is large, suggesting the characteristics of the variable is not well separated for two types of particles and therefore it is expected that ANN will not be

71
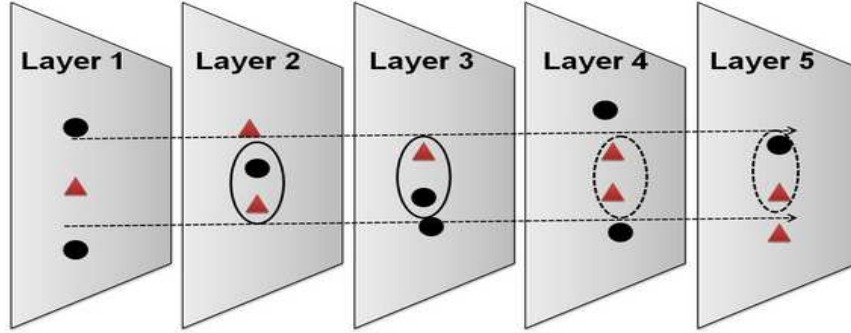
Figure 4.3: Schematic illustration of the philosophy of selection of inputs for identifying hits for Category-II inputs. Here the muon hit at layer 1 is the candidate hit i.e., the hit whose neighboring hits distribution is to be studied. A circular region is chosen around the candidate hit for 10 subsequent layers (5 layers are shown in the figure) and hit multiplicities inside the region is taken as the input to the network. The filled circles represent the hadron hits and the triangles represent the muon hits. As shown in this figure the projected circular area from the candidate muon hit on layer 1 consists of two hits (both muon and hadron) for all the successive four layers.

able to train the inputs very well to discriminate particles. As a result the particle identification efficiency in hit-level mixing will be comparatively lower than that for the inputs in event-level mixing. It is important to mention that we have obtained similar hit distribution pattern for single particle muons and hadrons of 1GeV energy, from the GEANT4 simulated prototype detector volume, as discussed in chapter 3.
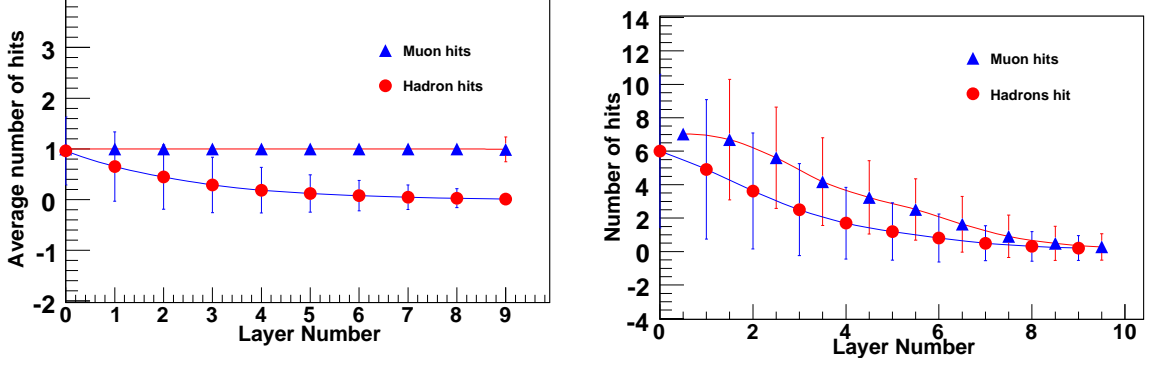
Figure 4.4: Left panel: Average number of hits (N_{hit}^m) in first 10 layers after the vertex for Category-I input e.g., when 1 GeV muon and 1 GeV hadron events are mixed at the event-level. Right panel: Hits (N_{hit}^m) distribution at different layers for Category-II input e.g., when 1 GeV muon hits and 5 GeV hadron hits are mixed at the hit-level to create a new event. N_{hit}^m is >1 even for muons, because the circular region for obtaining N_{hit}^m contains both types of particles. Here, for muon hits distribution, layer numbers are shifted slightly from the original value for better visualization. The error bars represent the RMS of the N_{hit}^m distribution calculated over a particular layer number.

4.3.3 Application of ANN method

N_{hits}^m from first 10 layers successive to the vertex layer for every event (category (a)) or every hit (category (b)) are used as inputs to ANN, first for training and then for testing the network for particle identification. About 50000 candidates are used for training and 25000 for testing in each case. We have tested various minimization methods and found that the Conjugate Gradient - Hestenes-Stiefel method [81] is the most effective for the present study. The assigned target (t^p in equation 4.8) output value of ANN for muon and hadron candidates are set as 1 and 0 respectively.

73
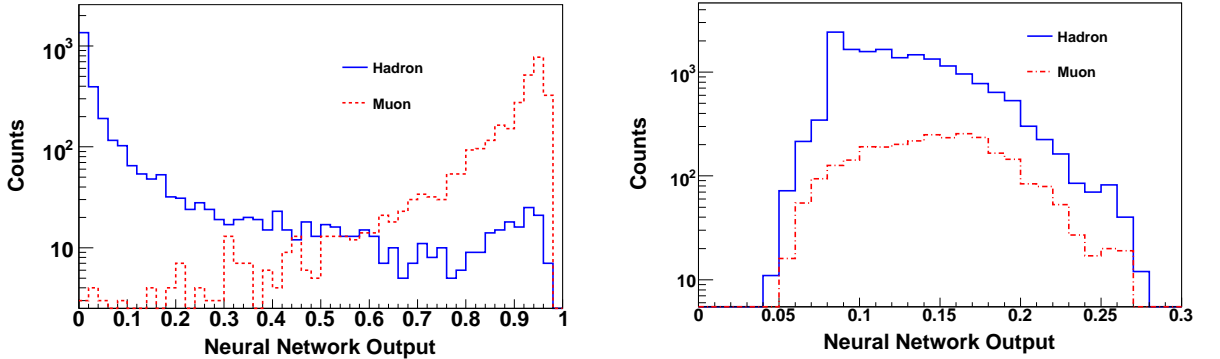
Figure 4.5: ANN output spectra for category I (Left Panel) and category II (Right Panel) inputs. Reasonable distinction are seen for two types of particles for category I input. We apply a threshold of 0.5 for obtaining the efficiency and background fraction. For category II inputs, as expected the spectra is not well separated and the threshold need to be adjusted to obtain reasonable muon discrimination efficiency.

4.4   Results

4.4.1   For single particle events

Figure 4.5 (left and right panel) shows the ANN output spectra for category I and II respectively. For further discrimination, a threshold is applied on the ANN output. Muons and hadrons are the selected candidates just above and below the threshold respectively.

For Category I, ANN outputs from muons and hadrons are well separated and a threshold of 0.5 is applied for selecting candidates and estimating the efficiency and background fraction. The efficiency (ϵ) and background fraction (B_f) are defined as follows:

$$\epsilon = \frac{\text{Number of selected muon candidates}}{\text{Total number of incident muon candidates}}, \quad (4.9)$$

$$B_f = \frac{\text{Number of selected non muon candidates}}{\text{Total number of incident non muon candidates}} \quad (4.10)$$

74
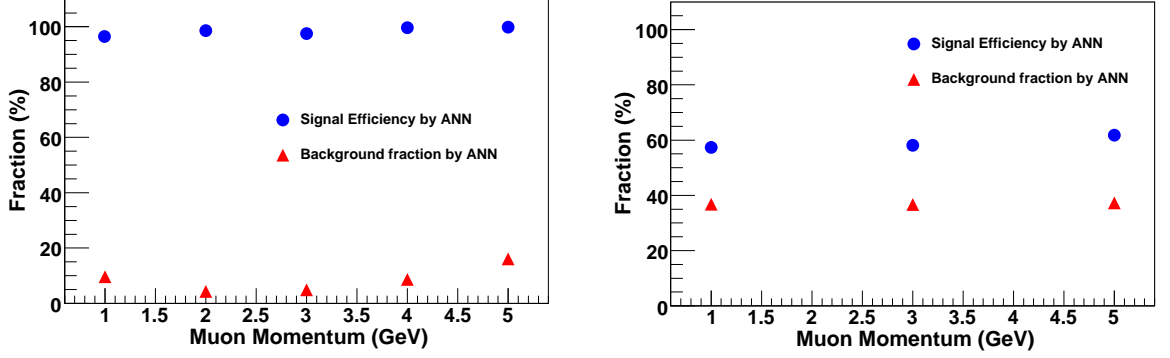
Figure 4.6: Left Panel: Variation of the muon discrimination efficiency and background fraction for category I input at 0.5 threshold, for muon events of varying energies. Right Panel: Variation of efficiency and background fractions with muon energy, for category II input. In this case 0.14 was the threshold value for the discrimination.

For category I, variation of efficiency and background fraction is shown in the Fig. 4.6 (left panel). The efficiency reaches $\approx 98\%$ with the background fraction $\approx 10\%$ and remain independent of input particle energy. As shown in figure 4.4 (left) for muons there are a large number of layers having non-zero hits however for hadrons on an average first 3 layers have non-zero signal i.e., number of hits at the layers convey the discrimination between muon and hadron to the network as seen in figure 4.5 (left). It is observed in the literature that ANN provides considerably better performance compared to the conventional methods which uses one particular parameter as input variable for discrimination. We have therefore formulated another method named as "One-Input Method (OIM)" where number of layers with non-zero hits is taken as the parameter for discrimination. In "One-Input Method" events having more than 3 layers with non-zero hits are taken as muon events.

It is observed that by ANN, both efficiency and background fractions are considerably improved compared to that of the one-input method. In the case of ANN, the efficiency
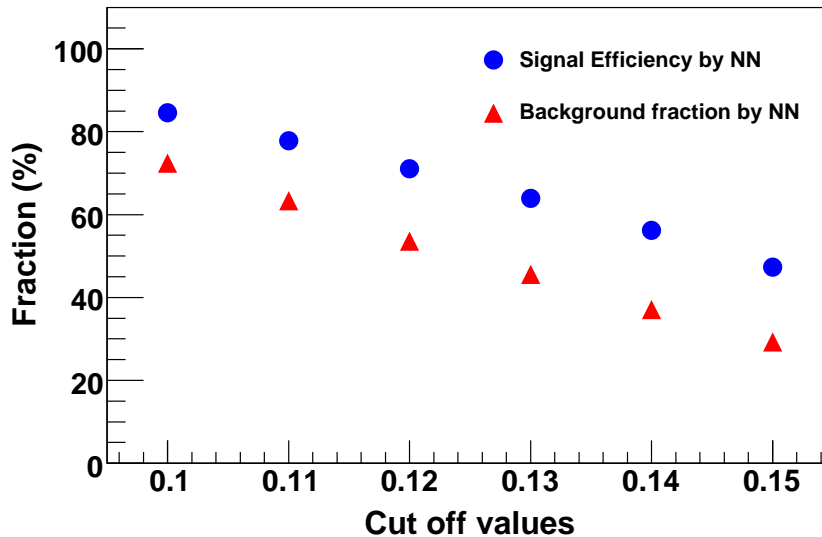
Figure 4.7: Variation of efficiency and background with varying threshold for Category-II, where 1 GeV muon hits and 5 GeV hadron hits are mixed at the hit-level in each event.

of detection of muon hits is $> 98\%$ with background fraction about 10%. However, we get poorer ϵ and B_f by the one-input method. The main difference we observe here is that in OIM, the background fraction deteriorates sharply with energy of the incident particles whereas in ANN the efficiency and background fraction remains independent of input energy. For category II, as shown in the figure 4.5 (right) the ANN output spectra for muon and hadron hits are not well separated. The hadron peak is shifted to ~ 0.08 and muon peak shifts approximately at 0.16. This performance is not un-expected as N_{hits}^{m} for both muons and hadrons have large RMS spread, at each layer as shown in figure 4.4 (right panel). For category II, a large number of samples for two particles have exactly similar hit distributions and this makes the discrimination extremely difficult. However for this category, a suitable threshold applied on ANN output can provide a reasonable separation between muons and hadrons. Figure 4.6 (right panel) shows the variation of ϵ and B_f with input muon momenta for Category-
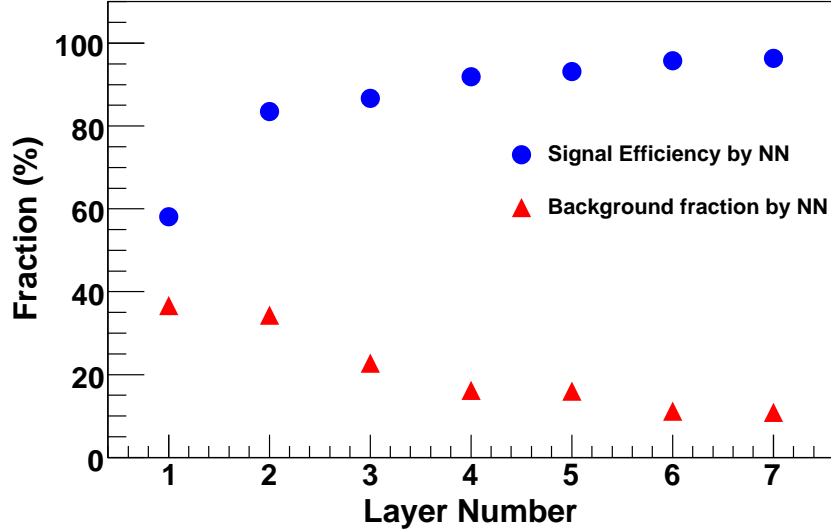
Figure 4.8: Efficiency and background fraction for Category-II input (where 1 GeV muon hits and 5 GeV hadron hits are mixed at the hit-level in each event) at different layers subsequent to the closest to the vertex.

II. The efficiency obtained is about 67 % with the background fraction of 40 % at threshold of 0.14. The efficiency and background fractions for Category-II at different thresholds are shown in figure 4.7. As shown in this figure, the efficiency can be improved considerably at the expense of purity of the samples. For example, the efficiency can reach 90 % with a background fraction of $\sim 70\%$. However reasonable adjustment of the threshold can reduce the background fraction. The results discussed so far for Category-II, are obtained only considering the hit multiplicity at layer 1 and this layer is closest to the vertex. This layer represents the most challenging scenario in terms of ambiguity in N_{hits}^{m} as shown in figure 4.4 (right panel) because at the 1st layer both muons and hadrons have equal number of hits on an average. Whereas if we proceed from 1st layer to other layers one by one, there are discrepancy in hits distribution between muons and hadrons for a particular energy. We also tried to use OIM for

this category, however no reasonable discrimination is obtained. In figure 4.8 we show the optimized results for Category-II input at different layers subsequent to layer 1. While going away from the vertex, hadrons get absorbed and the ambiguity between the patterns are reduced thereby giving better performance. As seen in figure 4.8, the efficiency increases slowly upto 98 % with the background fraction goes below 10 % for seventh layer.

4.4.2   Performance of ANN using input from NUANCE

As mentioned earlier, atmospheric neutrino interactions have been simulated using the NUANCE [83] neutrino interaction generator. The generator provides options for choosing neutrino fluxes and also flavor-mixing with the relevant cross sections, to be turned on from the source to the detection point associated . For studying the performance of ANN-discrimination for NUANCE generated neutrino events, we have incorporated NUANCE simulated output as input to the GEANT3 detector simulation code. In this case, the output obtained from GEANT is equivalent to the Category-II input i.e., muon and pion hits are mixed at hit-level in an event. For this study therefore, we have analyzed only the discrimination of CC neutrino interaction generated events. In addition to that, NUANCE input provides correct distributions of energy and particles as expected in case of atmospheric neutrino. Figure 4.9 (Left Panel) shows the average number of hits around the candidate muon and pion hits. The candidate hit means, the hit (muon or pion) which we want to identify. A pion hit is associated with ∼6 neighboring hits, whereas a muon hit has ∼1 hits at the first layer, the layer closest to the vertex and for rest of the layers both the particles have similar hits-distribution. It is important to mention that the neutrino flux utilized here is shown in figure 4.2 (bottom). Figure 4.9 (Right Panel) shows the output after

training of the samples by ANN. We obtain ~99% muon identification efficiency with ~40% associated background for a threshold of 0.55 applied on the output of ANN.
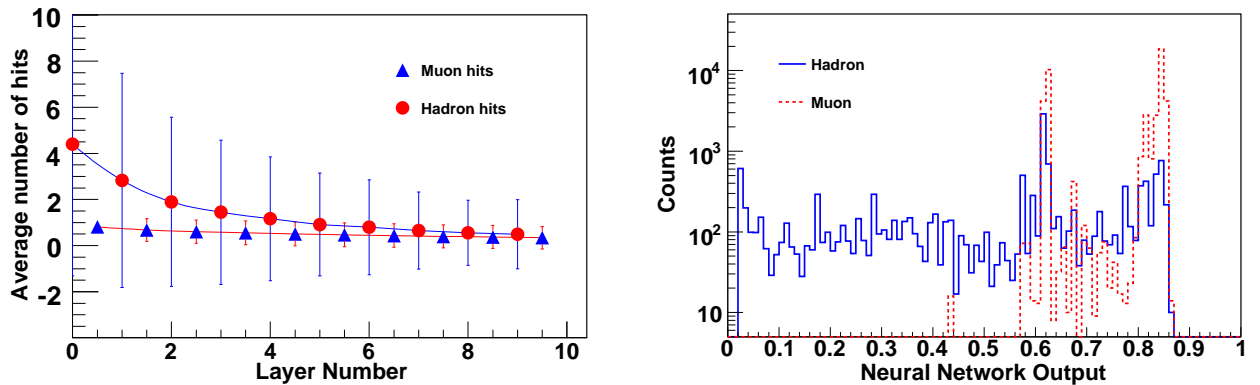
Figure 4.9: Left Panel: Variation of N_{hits}^m for muon and pion hits from the CC neutrino events generated from NUANCE. Here layer numbers for muon candidate hits are shifted slightly from the original value for better visualization purpose. Right Panel: ANN output spectra of the events containing the muon and pion hits, after training in ANN.

4.5 Summary and Discussions

The method of ANN has been applied to discriminate muons and hadrons generated due to neutrino interaction inside a calorimeter. A brief description about the geometry of the calorimeter and its simulation by GEANT3 is provided. For event-level mixing of single-particle muon and hadron events, we obtain the efficiency of muon identification upto 98% with a very low associated background fraction. However, for the case when muon and hadron hits are mixed in hit-level in an event i.e., CC neutrino interaction events, the efficiency of muon identification goes upto 67% with relatively larger background fraction.

In summary, we propose a method based on the artificial neural network for identifying muon hits as well as muon events in the midst of backgrounds due to hadron hits and hadron events respectively. The method can be applied to improve the track finding efficiency for muons considerably. The separated hadron hits can further be used for reconstructing hadron fraction in neutrino interactions.

Chapter 5

Track Reconstruction by Kalman Filter method

5.1 Introduction

As discussed earlier, one of the main observable used for probing the neutrino oscillation is the L/E distribution, where E is the energy of the interacting neutrino. Neutrinos produce corresponding charged leptons and associated hadrons while undergoing charged-current (CC) interactions with the iron nuclei of the ICAL detector. The simulated energy distributions of both the initial muon neutrinos and their product muons are shown in figure 5.1, as obtained from the NUANCE simulation. This distribution is for 5 years' unoscillated data sample. It is observed that the product muons carry substantial amount of energy of parent neutrinos. If neutrino oscillation is turned on in NUANCE; the distribution for the zenith angle dependence of the NUANCE generated muon events is shown in figure 5.2 and it is observed that oscillated flux is severely deteriorated in the upward direction ($\cos\theta_z > 0$) compared to that of
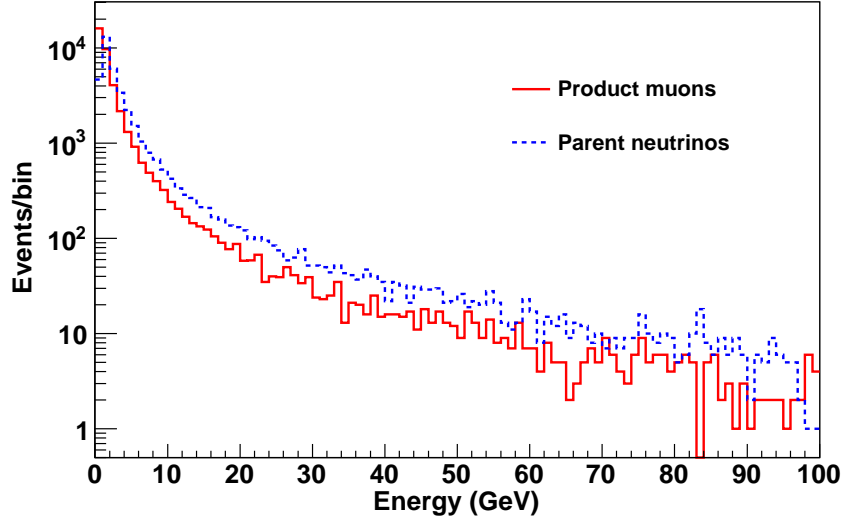
Figure 5.1: The distribution for interacting neutrinos events and product muons, in absence of oscillation.

the unoscillated flux. The muons generated from muon neutrinos due to the CC interactions inside ICAL, also have similar dependence on the zenith angle, as shown in figure 5.3. Hence, these two distributions of muon neutrinos and their product muons confirm that the product muons do reflect the energy and the direction of the parent neutrinos. The energy of the interacting neutrinos can be reconstructed by obtaining the energies of the product muons and hadrons.

The muon hits isolated from the hadron hits will form the muon track and the tracks will be used for reconstructing the energy of the neutrino event. Track reconstruction is a process by which one can determine the trajectory of the particle inside the detector. For INO, we reconstruct the muon tracks inside the calorimeter and the reconstructed momenta will be utilized further for physics analysis. The direction or curvature of the muon track will determine the particle type of the incident neutrino i.e., whether ν or $\bar{\nu}$. Since ν and $\bar{\nu}$ events produce μ^- and μ^+ after CC interaction $(\nu(\bar{\nu}) + A \rightarrow \mu^-(\mu^+) + X)$

82
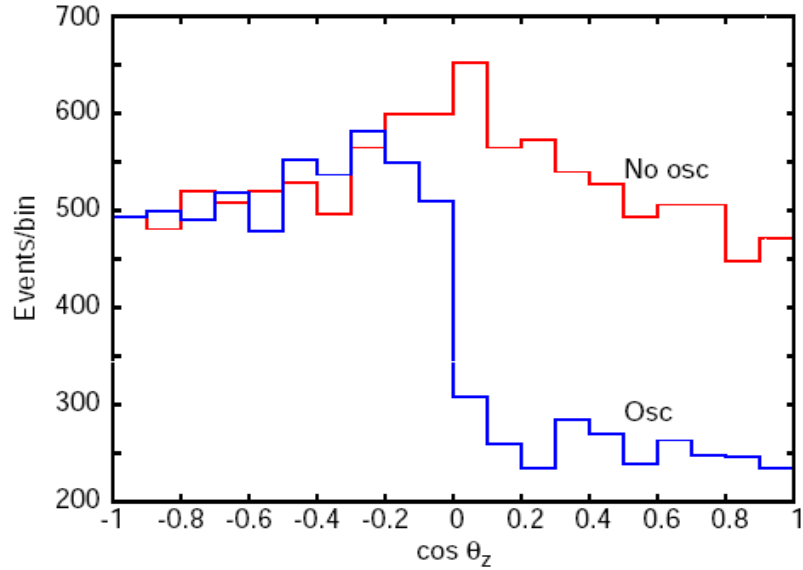
Figure 5.2: Zenith angle distribution for muon neutrino events. The events for $\cos\theta_z > 0.1$, termed as 'up-going' events in NUANCE are depleted when 2-flavour oscillations are turned on. (adopted from Ref. [46]).

and the product muons bend oppositely inside calorimeter in presence of magnetic field. This track reconstruction process can be split into two steps, track finding and track fitting. Different approaches to both the track finding and the reconstruction of the initial track parameters are investigated. In the present study for track fitting, a "Kalman Filter" [67] technique is utilized.

The Kalman filter technique is preferable over the global least square methods under appropriate circumstances due to the following features:

- The filter is recursive and is thus well suited for iterative track finding and fitting.

- The filter can be extended into a smoother and thereby provides optimal estimates of the track parameters along the tracks.
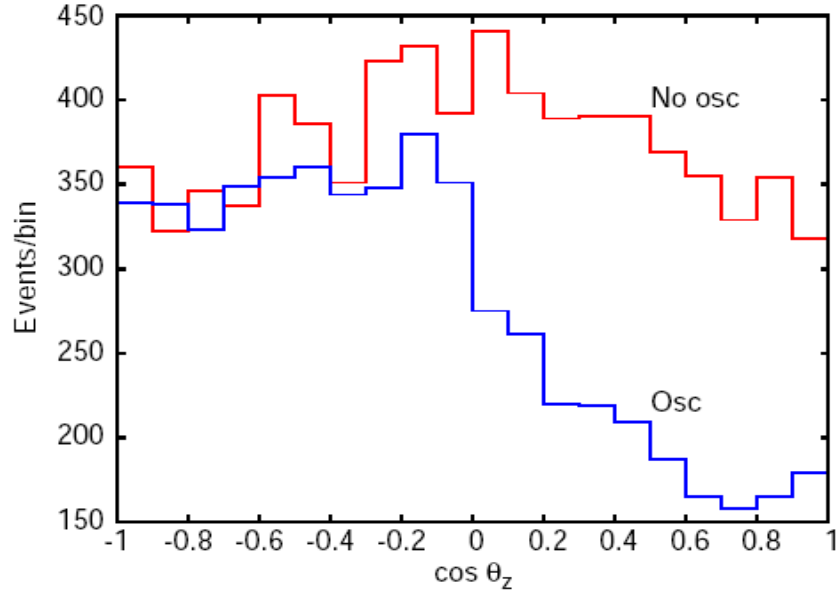
Figure 5.3: The muon events corresponding to the CC interactions of muon neutrinos in figure 5.2. Here also the effect of oscillation is similar to the neutrinos. (adopted from Ref. [46]).

- It permits efficient resolution and removal of outliers points.

- No large matrix operation is required.

Now, we would like to discuss the Kalman Filter algorithm and its implementation for reconstructing the tracks inside the prototype for the INO experiment.

5.2 Kalman Filter Algorithm

In the Kalman Filter framework, a track is designated as a set of parameters, called the Kalman State Vector ($\mathbf{r}$), which is allowed to change along the particle's path. The state vector should contain the information of the position of hits of a particle track

together with the direction of particle trajectory and also the momentum carried by the particle. In this case, the state vector is defined as $\mathbf{r} = \mathbf{r(x, y, dx/dz, dy/dz, q/p)^T}$ i.e., this column vector represents the particle's path in the x-y plane and dz is the distance between two consecutive detector planes. The procedure begins with a certain initial approximation $\mathbf{r} = \mathbf{r_0}$ and refines the vector $\mathbf{r}$ consecutively adding more measurements. The optimum estimation of the state vector is attained after the addition of the last measurement. The estimation of $\mathbf{r}$ is governed by the linear differential equation

$$\mathbf{r_k} = \mathbf{A_{k-1}r_{k-1}} + \nu_{\mathbf{k-1}}, \tag{5.1}$$

where A_{k-1} is a linear operator, $\nu_{\mathbf{k-1}}$ is the process noise between $(k-1)_{th}$ and k_{th} measurements. The process noise corrupts the state vector and the multiple scattering and energy loss suffered by a charged particle while traversing through a detector, are the sources of process noise. The quantity $\nu_{\mathbf{k-1}}$ corresponds to stochastic variations of the signal/state, through the detector associated with the propagation of tracks. A_{k-1} is also known as the propagator matrix which transports the state vector from $(k-1)^{th}$ layer(hit) to the kth layer(hit).

The components of the state vector mentioned above are not measured directly, the actual measurement is performed on a measurement space. Where the measurement vector $\mathbf{m_k}$ linearly depends on the state vector $\mathbf{r_k}$, then

$$\mathbf{m_k} = \mathbf{H_k r_k} + \eta_{\mathbf{k}}, \tag{5.2}$$

where H_k is the projection matrix between the measurement space and Kalman state, and η_k is the measurement noise. Hence the measurement performed at layer k is represented by the vector $\mathbf{m}_k$. The projection matrix H_k, which relates the state vector to the measurement vector is

$$H_k = \begin{bmatrix} 1 & 0 & 0 & 0 & 0 \\ 0 & 1 & 0 & 0 & 0 \end{bmatrix} \tag{5.3}$$

since the hits will be collected from the RPC read out strips, and the strips are aligned in x and y-directions on both surfaces of the RPC electrodes i.e., $m_k = \begin{pmatrix} x_k \\ y_k \end{pmatrix}$.

It is assumed that the measurement errors η_k and the process noise ν_k are uncorrelated, unbiased and the covariance matrices V_k, Q_k from these errors are expressed as

$$< \eta_k \cdot \eta_k^T > \equiv V_k,$$
$$< \nu_k \cdot \nu_k^T > \equiv Q_k. \tag{5.4}$$

In addition to the state vector, the covariance matrix C needs to be extrapolated in the Kalman filter fitting routine. By definitions, the covariance matrix consists of the estimated errors of the track parameters obtained from the resolutions of the detector measurements

$$C = \langle (\mathbf{r} - \langle \mathbf{r} \rangle).(\mathbf{r} - \langle \mathbf{r} \rangle)^T \rangle \tag{5.5}$$

Hence the covariance matrix is a 5×5 matrix.

The conventional Kalman Filter (KF) algorithm consists of following four stages ::

1. **Initialization Step** :: An approximate value of the vector $\mathbf{r_0}$ is chosen to start the fitting process. To start with, one first initializes the covariance matrix (C_0) with large positive diagonal values and null for the off-diagonal elements. As the filter progresses from layer to layer, more points/hits are added to the track, and the diagonal elements of the covariance matrix reduce to values, representing the uncertainties on the track parameters.

2. **Prediction step** :: The value of the state vector and the covariance matrix are propagated from the $(k-1)^{th}$ layer to the next layer i.e. the kth layer and the transportation equations are following:

$$\tilde{\mathbf{r}}_k = A_{k-1}\mathbf{r}_{k-1},$$

$$\tilde{C}_k = A_{k-1}C_{k-1}A_k^T. \tag{5.6}$$

The particle is moving in the magnetized iron calorimeter and we have used an analytic formula for track extrapolation inside magnetic field is discussed in Appendix A. In general, the fourth order Runge-Kutta method [85] is widely used in high-energy physics for charged particle tracking through a magnetic field e.g., for the transport of charged particle in GEANT. Fourth-order method means that the precision of the method depends on the step size to the fifth power. Runge-Kutta methods of any order exist, however the fourth-order method is the optimal one with respect to the CPU time consumption. When a particle proceeds inside the detector it undergoes energy loss due to the inelastic scattering and also faces multiple scattering, which are part of the process noise. These noises will perturb the state vector and the effect of the perturbation or noise will be comparatively larger when the momentum of the moving particle is small. So in the next step of the Kalman Filter algorithm, the influence of the noise is incorporated to the state vector. Once the state vector is updated, it will simultaneously modify its corresponding covariance matrix also.

3. **Process noise** :: The process noise describes probabilistic deviations of the state vector $\mathbf{r}$. The state vector and its covariance are modified in the following way:

$$\hat{\mathbf{r}}_k = \tilde{\mathbf{r}}_k,$$
$$\hat{C}_k = \tilde{C}_k + Q_k. \tag{5.7}$$

As mentioned earlier, the process noise has to be incorporated during the track propagation and so the covariance of process noise is calculated at each step. This covariance matrix will consist of noise due to multiple scattering and energy

loss. Hence the covariance matrix for process noise will be [86] :

$$
\begin{bmatrix}
Q_k^{MS} & 0 \\
0 & Q_k^{\delta E}
\end{bmatrix}
\tag{5.8}
$$

The q/p covariance $Q_k^{\delta E}$ is

$$
Q_k^{\delta E} = \left(0.25 \frac{\delta E}{p^2}.ds/dz \right)^2
\tag{5.9}
$$

where δE is the mean energy loss for a perpendicular muon while crossing $\sim$ 6 cm thick iron plate inside the ICAL detector and we have calculated the value of δE as $\sim$63 MeV from the Bethe-Bloch equation [66]. ds is the distance traversed by the particle between two successive detector layers and $\frac{ds}{dz} = \sqrt{(1 + (dx/dz)^2 + (dy/dz)^2)}$.

The multiple scattering part of the covariance matrix is calculated to be [87]

$$
\begin{bmatrix}
\delta z^2 \sigma_{33}^2 & \delta z^2 \sigma_{34}^2 & -\delta z \sigma_{33}^2 & -\delta z \sigma_{34}^2 \\
\delta z^2 \sigma_{34}^2 & \delta z^2 \sigma_{44}^2 & -\delta z \sigma_{34}^2 & -\delta z \sigma_{44}^2 \\
-\delta z \sigma_{33}^2 & -\delta z \sigma_{34}^2 & \sigma_{33}^2 & \sigma_{34}^2 \\
-\delta z \sigma_{34}^2 & -\delta z \sigma_{44}^2 & \sigma_{34}^2 & \sigma_{44}^2
\end{bmatrix}
\tag{5.10}
$$

where

$$
\sigma_{33}^2 = \frac{1}{2}\sigma_{MS}^2 \left(\frac{ds}{dz} [1 + t_x^2] \right)
\tag{5.11}
$$

$$
\sigma_{34}^2 = \frac{1}{2}\sigma_{MS}^2 \left(\frac{ds}{dz} [t_x.t_y] \right)
\tag{5.12}
$$

$$
\sigma_{44}^2 = \frac{1}{2}\sigma_{MS}^2 \left(\frac{ds}{dz} [1 + t_y^2] \right)
\tag{5.13}
$$

In the above expressions, the direction of the particle track along the x-direction is $t_x = dx/dz$ and similarly the direction along y-axis is given by $t_y = dy/dz$. Similarly, in those expressions σ_{MS} is the variance of the multiple scattering angle:

$$
\sigma_{MS}^2 = (13.6\text{MeV}/p)^2 [1 + 0.038\ln(X/X_R)] X/X_R
\tag{5.14}
$$

In the above equation X_R is the radiation length (1.76 cm) of iron and X is the distance travelled by the particle inside the scatterer.

Next step is to check which of the propagated hits will be included into the track and this is performed by χ^2- checking in the following Filtration step.

4. **Filtration step** :: In this step, $\mathbf{r}_k$ is updated with the new measurement $\mathbf{m}_k$ to get the optimal estimate of $\mathbf{r}_k$ and as a consequence, the covariance of state vector C_k is also modified. In this step a new variable is formulated by using the parameters obtained from the previous three steps. This new parameter is known as the Kalman gain matrix and designated by K_k.

$$K_k = \hat{C}_k H_k^T \left(V_k + H_k \hat{C}_k H_k^T \right)^{-1}. \tag{5.15}$$

Initially the covariance matrix $\hat{C}_k$ dominates the denominator $\left(V_k + H_k \hat{C}_k H_k^T \right)^{-1}$, so the gain K_k is almost unity at the beginning of fitting. As the number of points associated with the track increases during fitting, the denominator becomes dominated by the measurement noises V_k and the value of Kalman gain gets comparatively smaller. With large gain values, the addition of a new measurement to a track has a significant impact on the updated track parameters. On the other hand, when the gain reduces while more points are added to a track, the addition of new points has progressively smaller impact on the update. Decomposing all the matrices like $\hat{C}_k$, H_k^T and V_k, the simplified form of K_k will be like:

$$K_k = \hat{C}_k \begin{bmatrix} 1 & 0 \\ 0 & 1 \\ 0 & 0 \\ 0 & 0 \\ 0 & 0 \end{bmatrix} \left\{ \begin{bmatrix} V_{00} & V_{01} \\ V_{10} & V_{11} \end{bmatrix} + \begin{bmatrix} 1 & 0 & 0 & 0 & 0 \\ 0 & 1 & 0 & 0 & 0 \end{bmatrix} \begin{bmatrix} C_{00} & C_{01} & C_{02} & C_{03} & C_{04} \\ C_{10} & C_{11} & C_{12} & C_{13} & C_{14} \\ C_{20} & C_{21} & C_{22} & C_{23} & C_{24} \\ C_{30} & C_{31} & C_{32} & C_{33} & C_{34} \\ C_{40} & C_{41} & C_{42} & C_{43} & C_{44} \end{bmatrix}_k \begin{bmatrix} 1 & 0 \\ 0 & 1 \\ 0 & 0 \\ 0 & 0 \\ 0 & 0 \end{bmatrix} \right\}^{-1}$$

$$K_k = \begin{bmatrix} C_{00} & C_{01} \\ C_{10} & C_{11} \end{bmatrix}_k \left\{ \begin{bmatrix} V_{00} & V_{01} \\ V_{10} & V_{11} \end{bmatrix} + \begin{bmatrix} C_{00} & C_{01} \\ C_{10} & C_{11} \end{bmatrix} \right\}^{-1} \tag{5.16}$$

The gain matrix regulates or updates the state vector($\mathbf{r}_k$) and the covariance matrix(C_k) in the following ways:

$$\begin{aligned} \mathbf{r_k} &= \hat{\mathbf{r}}_k + K_k \left(\mathbf{m_k} - \mathbf{H_k}\hat{\mathbf{r}}_\mathbf{k} \right), & (5.17) \\ C_k &= \hat{C}_k - K_k H_k \hat{C}_k. \end{aligned}$$

The residual of the measurement vector and the state vector i.e., $\left(\mathbf{m_k} - \mathbf{H_k}\hat{\mathbf{r}}_\mathbf{k} \right)$ determines how much the value of $\mathbf{r}_k$ will be updated.

Next is the calculation of the value of χ^2_k and minimum value of χ^2_k determines which of the hit points i.e., state vectors $\mathbf{r}_1, ...\mathbf{r}_k$ will be included in the fitted track. A χ^2_k criterion is needed to select the most suitable candidate and to decide whether the most relevant candidate is in fact sufficiently close to the track to be added to it and the χ^2_k is calculated by:

$$\chi^2 = \chi^2_{k-1} + (m_k - H_k \hat{r}_k)^T \left(V_k + H_k \hat{C}_k H_k^T \right)^{-1} (m_k - H_k \hat{r}_k). \qquad (5.18)$$

The value χ^2_k is the total χ^2- deviation from the measurements $m_1, ...m_k$.

All the four processes discussed above shown in a flowchart in figure 5.4.

In brief, in the track fitting algorithm, the track parameters are modified and the reconstructed parameters are obtained from the optimal state vector i.e., from the state vector $\mathbf{r}_n$ obtained after the iterations over all the layers. This method is a very useful one since it can be used in both track finding and track fitting simultaneously.
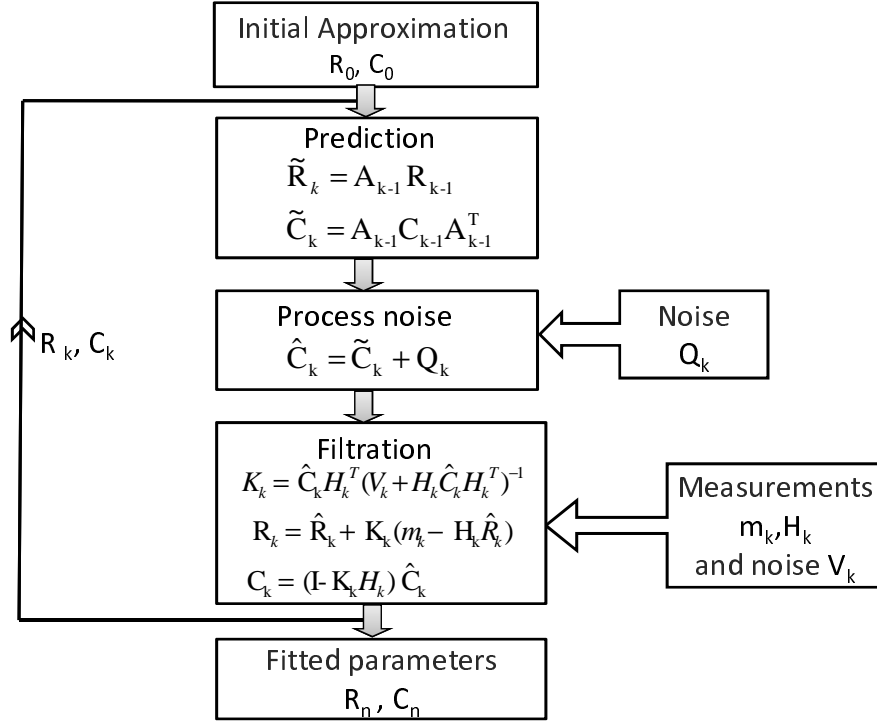
Figure 5.4: Flowchart to represent the main processes in Kalman Filter method.

5.3 Implementation of Kalman Filter method for track fitting and the results

As mentioned earlier, the state vector at a point on the particle trajectory can be represented by the 5 parameters: $\mathbf{r = r(x, y, dx/dz, dy/dz, q/p)}$ where x and y are for hit positions, dx/dz and dy/dz define track direction, and q/p is the charge to momentum ratio. The kalman state vector $\mathbf{r}$ is then allowed to be modified during track fitting by considering the process and measurement noises. The process noise includes noises due to multiple scattering and energy loss by the charged particle while passing through the detector whereas the measurement noise comes from the measurement plane which is due to the random disturbance in measurement of hits. The optimal
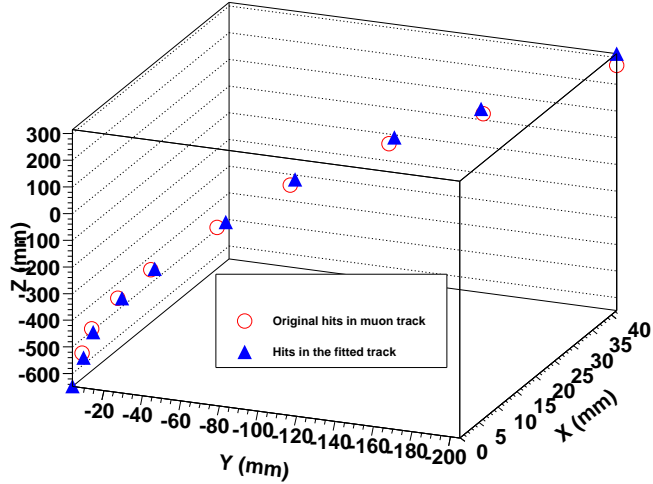
Figure 5.5: Comparison of hits from a single muon track before and after propagation.

estimation of state vector i.e., $\mathbf{r_n}$ in flowchart 5.4 should give the reconstructed track parameters at every point or layer.

As explained in earlier section that there are two main processes in KF method: prediction and filtration. In the prediction step, the current state vector is extrapolated to the next detector layer by including the multiple scattering and energy loss of the corresponding particle. In the filtration step, the extrapolated state vector is updated by taking a weighted mean with the new measurement. This means that after each prediction step it has to be decided which measurement should be included in the subsequent filter step. Conventionally, the measurement which is closest to the prediction is selected for inclusion in the filter.

In the present case, the track fitting begins with a seed track and proceeds with the hits of the single muon track through the ICAL prototype. The initial state vector components are chosen to be zero. Furthermore, the non-diagonal elements of the state vector covariance matrix C_0 are set to zero whereas all the diagonal elements have non-

zero values reflecting the initial uncertainty in the measurements [88]. This covariance matrix takes care of the multiple scattering and energy loss due to the passage of the charged particle inside the calorimeter material. At first, the fit proceeds towards the downstream direction (from first layer to last layer) and the seed parameters are transported to the first downstream active plane. This transportation follows the track extrapolation formula based on the analytic formulation[1] which takes care of the bending of the track in presence of the magnetic field. A fully-contained single particle track points before and after fitting is shown in the figure 5.5. During fitting, a particular measured hit point on the extrapolated layer is included to the fitted track if difference between the projected hit and the measured hit is minimum, among all the hits on a layer. We also calculate the covariance due to the process noise during and after each propagation. For this study, the covariance of measurement noise is set to zero as all the hit points are obtained from GEANT4 simulation, without any measurement error. The mean energy deposition for muons as calculated from Bethe-Bloch equation is approximately 63 MeV while traversing a 6.0 cm thick iron plane perpendicularly. This energy loss is incorporated to modify the fifth component of state vector i.e., the q/p. When the downstream fit ends, its last updated state vector is again used as the starting value for the propagation proceeding from last layer to the first layer. This upstream fit is performed in the same fashion, starting from the same initial covariance matrix as used during the downstream fit. The value of the momentum from the final state vector at the first layer obtained at the end of the upstream fit is the reconstructed momenta of a particular track.

The analytic formula for the motion of charged particle in the magnetic field has been implemented in Kalman filter and the routine is tested for a large number of muon events. The fitting program based on the Kalman filter method provides good esti-

---

[1]Analytic formula discussed in Appendix A
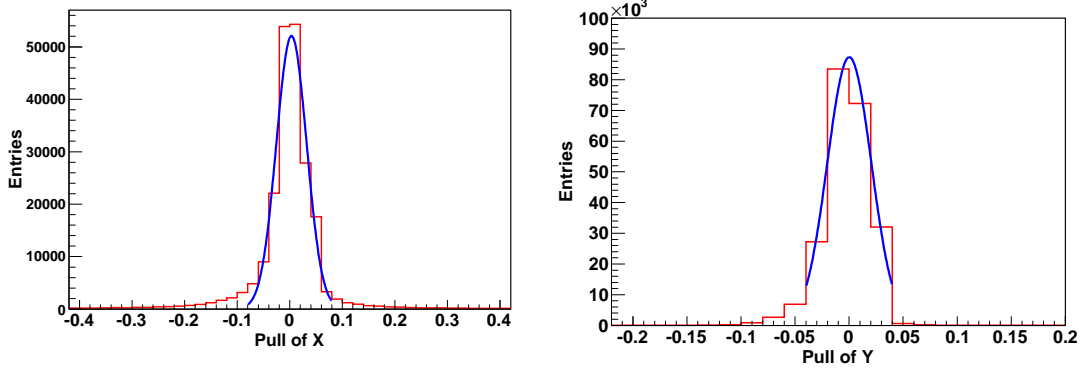
Figure 5.6: x,y-pull distributions after track fitting.

mation of track parameters. This is represented by the pull distributions of various parameters. The pull (normalized residuals) distribution for the track co-ordinates x,y and track momentum are shown in figure 5.6 and figure 5.7 respectively. All the distributions have Gaussian nature with mean close to zero. The pull is defined as the ratio of the difference between reconstructed track parameters with the incident parameters to the values of track parameters of incident tracks. The reconstructed momenta obtained after the completion of fitting for 1 GeV single particle simulated muon events is shown in figure 5.8. The distributions are fitted with Gaussian, excluding the non-Gaussian tail. The main reason for this non-Gaussian tail lies in the reconstruction process. The code is not always efficient enough to reconstruct the entire track, resulting in a smaller track length and as a consequence a smaller measured momentum.

The linearity of the variation of the average reconstructed momenta with the incident muon momenta is found to be satisfactory as shown in figure 5.9. The performance of the fitting is characterized by the momentum resolution of the reconstructed tracks as shown in figure 5.10, where

$$\text{resolution } (\%) \;=\; \frac{\sigma}{M} \;\times\; 100. \tag{5.19}$$

94
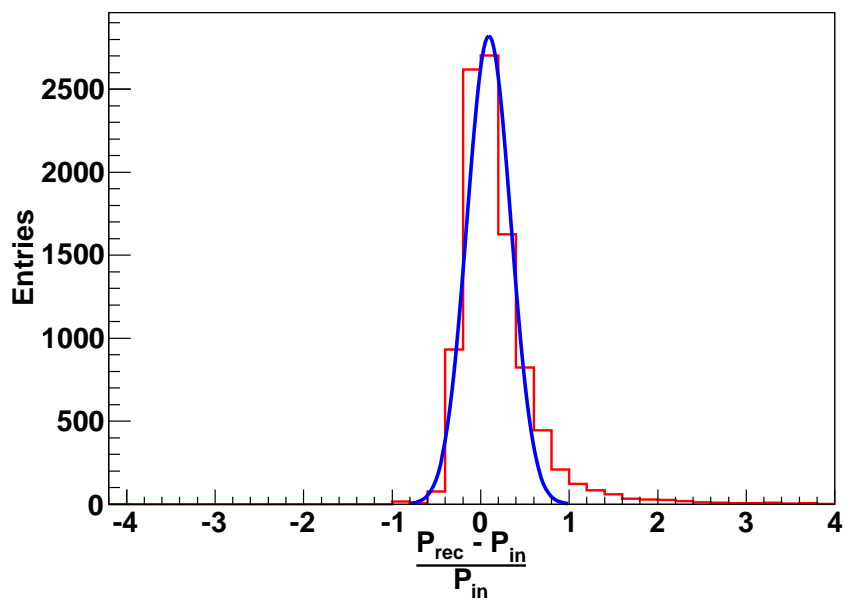
Figure 5.7: Pull of muon tracks momenta after track fitting.
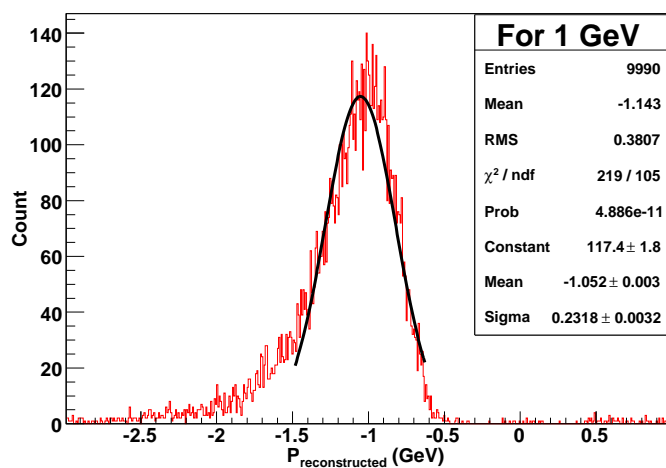
Figure 5.8: Reconstructed momentum distribution for 1 GeV incident muon events.
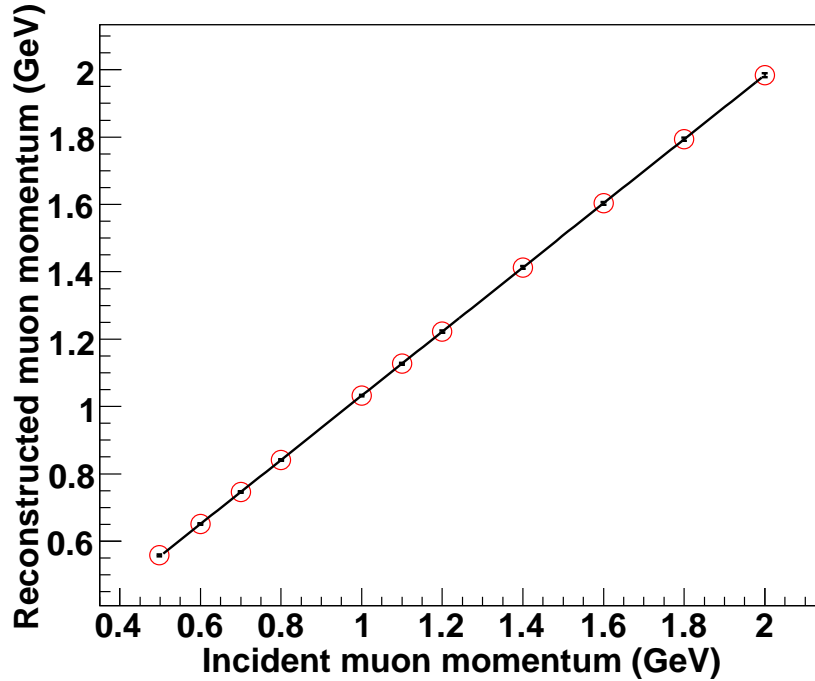
Figure 5.9: Reconstructed momenta for incident muon tracks of varying momentum.

Where σ is the width of the gaussian and M is the average fitted momenta as shown in figure 5.8.

For a fully-contained muon track i.e. the track which stops inside the detector volume, we can estimate its initial momentum very well. For this prototype, the muon tracks having energy up to 1.1 GeV are fully contained, although the code is sensitive enough to reconstruct the partially contained events. However, for momenta beyond 2 GeV, the resolutions is worsened [90] considerably. The main reason is that at higher momentum, the particles travel beyond the 13 iron layers of the prototype detector.
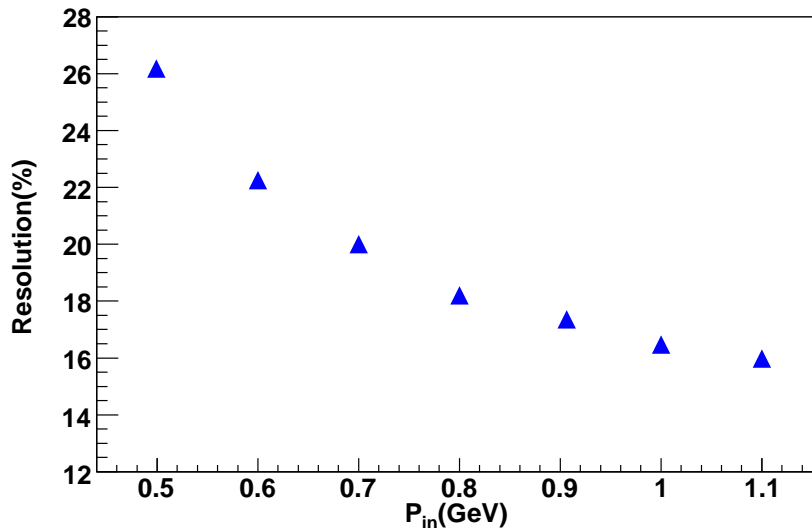
Figure 5.10: Resolution of the reconstructed momenta.

5.4   Summary

We have developed a track fitting algorithm by implementing the Kalman Filter algorithm where track parameters are reconstructed by fitting the measured hits on the prototype calorimeter of INO. The Kalman filter routine takes care of the particle bending inside the magnetic field. In this work, the cosmic muon tracks inside the prototype calorimeter have been fitted and the momenta of the tracks have been reconstructed with good resolution. The performance of the fitter is also represented by the pull distribution of different track parameters. This code can be utilized for the analysis of the ICAL events for INO experiment.

Chapter 6

Monte Carlo Simulation to study the effect of surface roughness on the performance of RPC

6.1 Introduction

The Resistive Plate Chambers (RPCs) [49] will be used as the active detectors of the iron calorimeter for the INO experiment. The cosmic neutrinos will produce corresponding charged leptons and hadrons while interacting with iron nucleons inside the 50 kTon iron calorimeter. The possible options for the electrodes to be used for the INO-RPCs are bakelite or glass having high resistivity. As per the requirements in INO, the time resolution of the RPCs is $\sim$ 2ns with an efficiency $> 90\%$. The glass and bakelite RPCs being operated in the prototype calorimeter are working in avalanche and streamer modes respectively. The RPCs can be operated in trigger and timing modes providing timing resolution of $\sim$ 2ns and $\sim$ 40ps respectively. Even though the

single-gap RPCs in trigger mode of operation will do the job for INO, multi-gap RPCs are commonly used in avalanche mode in timing application. It is therefore of extreme importance to develop a framework to simulate the operation of RPCs by implementing all the relevant processes in gas applying Monte Carlo techniques.

In this work, we have simulated the performance of a chamber working in avalanche mode by implementing the primary ionization, avalanche development processes inside the gas volume and then induced current is calculated considering the space charge effect when a minimum ionizing particle passes through the detector. Efforts have been made earlier towards achieving this goal. Detailed analytical formulas and procedures for primary ionization, avalanche development processes and to obtain induced signal, charges and time resolution are described in Ref. [91]. The analytic formalism is discussed in section 6.2. The Monte Carlo procedure developed in this study, simulates all the above mentioned processes inside the RPC gas gap and follows techniques similar to the one discussed in Ref. [91] and additionally we have introduced surface roughness of bakelite electrodes for further study. Typically, the resistivity of the electrode material is in the range of $10^{10} - 10^{12} \ \Omega - $ cm and a large voltage gradient of > 10 kV/mm is applied across the electrodes. For this work, we consider a 0.3 mm single-gap RPC, having 2 mm thick bakelite electrodes. We have used $C_2F_4H_2$, $i - C_4H_{10}$, SF_6 gases in $85 : 5 : 10$ ratio as a gas mixture for the detector. It is reported in Ref [92] that the efficiency of a P-120 grade bakelite RPC operating in streamer mode decreases gradually with the increase in voltage across the electrodes. One of the possible reasons for the decrease in detection efficiency is assumed to be the non-uniformity in the inner surface of bakelite electrodes, which may cause drastic variation in electric field inside the gas gap. Several approaches/methodologies are applied to smoothen the surface of electrodes to obtain better detection efficiency. For example, a $\sim 10 \mu m$ thick coating of the highly viscous silicone fluid gives a stable efficiency plateau at 96% [92]. In BaBar

RPCs, similar exercises were adopted for surface treatment using linseed oil. Similar exercises were made elsewhere using linseed oil for smoothness of surface. There are previous studies where the electric fields have been calculated at the edges of rough surfaces. Finite element analysis (FEA) software ANSYS has been used to calculate the electric field variation due to various defects e.g. pin, ball, dome and ridge [93]. In the present work we tried to simulate the effect of the variation in average electric field inside the gas gap due to the defects on the surface of electrodes.

6.2 Monte Carlo Simulation to study the RPC performance

When a charged particle passes through the RPC, it ionizes the gas. During primary ionization the average number of clusters generated for the $C_2F_4H_2/i-C_4H_{10}/SF_6$ 85/5/10 gas is provided by HEED [94]. HEED is a Monte-Carlo model based on the photo-absorption ionization model by W.W.M. Allision and J.H. Cobb [95]. It is assumed that the probability of occurance of an ionizing collision is independent of the previous collision, considering if the energy loss is negligible compared to the particle energy. The probability of finding a cluster between position x and $x + dx$ is [96]

$$P(x) = \frac{1}{\lambda}e^{-x/\lambda} \tag{6.1}$$

where λ is the average distance between two clusters or mean free path. If $\sigma_p(\beta)[\text{cm}^2]$ is the ionization cross-section in a gas with density ρ and pressure P, the mean free path can be expressed as:

$$\lambda = \frac{A}{\rho N_A}\frac{1}{\sigma_p(\beta)} \tag{6.2}$$

where A is the atomic mass number of the gas [gm/mol] and N_A is the Avogadro's number [1/mol].

The number of electrons in a cluster depends on the amount of energy exchanged in a particular interaction, this energy transfer can vary from interaction to interaction, and the distribution is known as the *cluster size distribution*. HEED is used to calculate the cluster size distribution for a given gas mixture and the distribution is shown in figure 6.1.
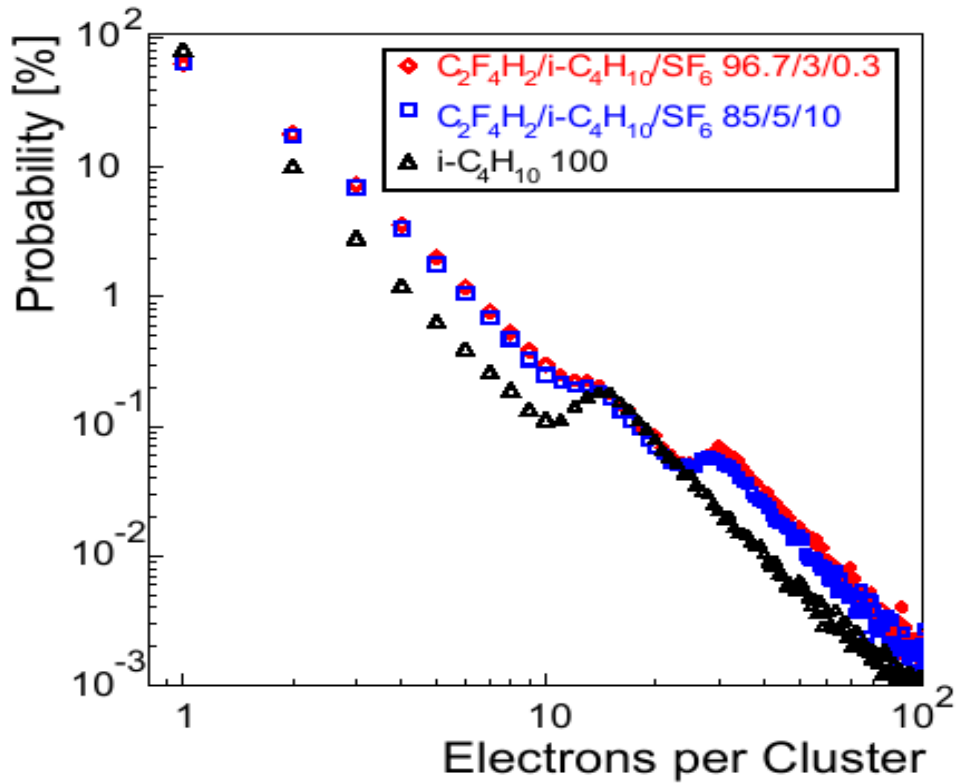
Figure 6.1: Cluster size distribution for RPC gas mixture, (adopted from Ref [91])

The average number of clusters formed and the probability distribution of the number of electrons per cluster, both are estimated from HEED [94] and the values obtained are similar to the values used in Ref. [91]. The avalanche development of the primary electrons is governed by the Townsend coefficient α and attachment coefficient η. The Townsend coefficient is defined as the average number of ionizing collisions suffered

by an electron while travelling unit distance in the direction of the field. There is another probability that the electrons may get attached with the neutral gas molecules, forming negative ions. The attachment coefficient (η) is defined as the probability of attachment per unit distance traversed by an electron in the direction of the field. Hence the attachment will reduce the number of ionizations per unit distance from α to $\alpha - \eta$, known as the effective Townsend coefficient or effective primary ionization coefficient. In general α and η are functions of E/p, where E is the electric field strength and p is the pressure of the gas.

If the avalanche contains n electrons at position x the probability that it will contain $n + 1$ electrons at $x + dx$ is given by $n\alpha dx$. Similarly, the probability for an electron get attached over the distance dx from an avalanche of size n is $n\eta dx$. The average number of electrons $\bar{n}$ and positive ions $\bar{p}$ at position $x + dx$ is governed by [97]

$$\frac{d\bar{n}}{dx} = (\alpha - \eta)\bar{n}, \frac{d\bar{p}}{dx} = \alpha\bar{n} \tag{6.3}$$

with the initial conditions $\bar{n}(0) = 1$ and $\bar{p}(0) = 0$ will provide the solution,

$$\bar{n}(x) = e^{(\alpha-\eta)x}, \bar{p}(x) = \frac{\alpha}{\alpha - \eta}(e^{(\alpha-\eta)x} - 1) \tag{6.4}$$

Let, the avalanche starts from a single electron generated due to primary ionization and the probability of having n avalanche electrons after traversing x distance is given by [91]

$$
\begin{aligned}
P(n, x + dx) &= P(n-1, x)\ (n-1)\alpha dx\ (1 - (n-1)\eta dx) \\
&\quad +P(n, x)\ (1 - n\alpha dx)\ (1 - n\eta dx) \\
&\quad +P(n, x)\ n\alpha dx\ n\eta dx \\
&\quad +P(n+1, x)\ (1 - (n+1)\alpha dx)\ (n+1)\eta dx \tag{6.5}
\end{aligned}
$$

The four lines are depicting four possibilities during the avalanche development. The first line represents the probability that there are $n - 1$ electrons at x, exactly one of

them create further ionization and no electron gets attached. The second line gives the probability that there are n electrons at x, no electron creates ionization and no electron is attached. The third line gives the probability that from the n electrons, one multiplies and one get attached and finally the fourth line gives the probability that from the $n + 1$ electrons, one gets attached and no electron is multiplied. Neglecting the higher order terms, the evaluation of the above expression gives

$$\begin{aligned}
\frac{dP(n, x)}{dx} &= -P(n, x)n(\alpha + \eta) + P(n - 1, x)(n - 1)\alpha \\
&\quad + P(n + 1, x)(n + 1)\eta
\end{aligned} \tag{6.6}$$

Now the solution of the above equation will be the probability to have n avalanche electrons at position x, which is depicted by the relation

$$P(n, x) = \begin{cases} k\frac{\bar{n}(x)-1}{\bar{n}(x)-k} & n = 0 \\ \bar{n}(x)(\frac{1-k}{\bar{n}(x)-k})^2(\frac{\bar{n}(x)-1}{\bar{n}(x)-k})^{(n-1)} & n > 0 \end{cases} \tag{6.7}$$

where

$$\bar{n}(x) = e^{(\alpha-\eta)x}, k = \frac{\eta}{\alpha} \tag{6.8}$$

Hence, the avalanche multiplication is a stochastic process and due to the statistical fluctuation there are different models used for avalanche process. One of them is the Polya distribution derived from the probability p to have $n + 1$ electrons at $x + dx$:

$$p = nc\left(b - \frac{1-b}{n}\right) \tag{6.9}$$

where c and b are constants. This expression represents the avalanche charge distribution of RPC.

To implement the Monte Carlo procedure for the avalanche process according to equation 6.7, we generate uniform random numbers in the interval (0,1) and calculates

$$n \begin{cases} 0, & s < k\frac{\bar{n}(x)-1}{\bar{n}(x)-k} \\ 1 + \text{Trunc}[\frac{1}{\ln(1-\frac{1-k}{\bar{n}(x)-k})} \ln(\frac{\bar{n}(x)-k)(1-s)}{\bar{n}(x)(1-k)})], & s > k\frac{\bar{n}(x)-1}{\bar{n}(x)-k} \end{cases} \tag{6.10}$$

where 'Trunc' implies truncation of the decimals. If $\bar{n}(x)$ is very large, a series expansion is used for $\ln(1 - x) = -(x + \frac{1}{2}x^2 + \frac{1}{3}x^3 + \ldots)$

To calculate the induced signal, we have to simulate the avalanche development process for the electrons. For that, the gas gap is divided into N steps of step size Δx. The average multiplication $\bar{n}(\Delta x)$ for a single electron while passing through Δx distance is given by $e^{(\alpha-\eta)\Delta x}$. Suppose, starting with one electron at $x = 0$, we find n_1 electrons at $x = \Delta x$, where n_1 is obtained from equation 6.7. Each of these electrons will again multiply in the similar fashion. To find n_2 number of electrons at $x = 2\Delta x$ position inside the gap, we have to make a loop over n_1 electrons and repeat the process of equation 6.7 for each electron and add them up to get the avalanche growth for the n_1 electrons. And this procedure has to be repeated through the whole gap and for all the existing electrons at each step. This method is very time consuming and as a remedy we have applied the central limit theorem which makes the whole process very fast. If the number of electrons n_i at any position $i\Delta x$ is sufficiently large(~ 100), then the central limit theorem will calculate the number of electrons n_{i+1} at distance $(i+1)\Delta x$ from a Gaussian random number with mean μ and sigma σ_μ of

$$\mu = n_i\bar{n}(\Delta x), \sigma_\mu = \sqrt{n_i}\sigma(\Delta x) \tag{6.11}$$

where σ comes from the variance of the distribution 6.7

$$\sigma^2 = \left(\frac{1+k}{1-k}\right)\bar{n}(x)(\bar{n}(x) - 1) \tag{6.12}$$

If the gas gain is high or the number of charges in an avalanche at a particular position are sufficiently large, then they influence the electric field in the gas, and simultaneously the values of α and η. This effect is known as the *space charge effect*. For a small gas gain in the detector, the electric field $E_0 = U_0/d$ between the two electrodes is uniform, where U_0 is the applied voltage. The approximate perturbation of the field due to the
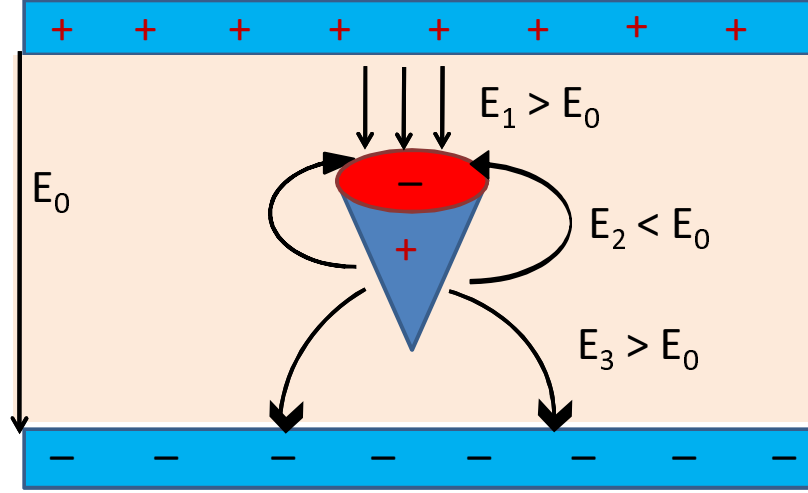
Figure 6.2: Space charge effect is shown schematically. Here E_0 is the applied field across the RPC electrodes and E_1, E_2 and E_3 are the electric field arises due to the accumulation of space charges between the two electrodes.

space charge can be deduced, e.g., consider a sphere of r_s having n number of electrons, then the field at the surface of this charged sphere will be

$$E_s = \frac{e_0 n}{4\pi\varepsilon_0 r_s^2} \tag{6.13}$$

where e_0 is the unit charge and ε_0 is the dielectric constant of the vacuum. For an avalanche containing 10^7 number of electrons and $r_s = 0.1$ mm, the field due to space charge is $E_s = 144$ V/mm, which is about 30% of E_0 (50 kV/cm) of trigger RPCs and about 15% of E_0 (100 kV/cm) of timing RPCs. The space charge plays an important role in the field perturbation inside a RPC and hence affects the detector's response. The space charge effect is shown schematically in figure 6.2. For typical RPC gas mixtures, this perturbation of the field due to the space charge changes the effective Townsend coefficient and as a consequence the avalanche growth inside the detector get affected . In the simulation we have taken care of the space charge effect and stopped
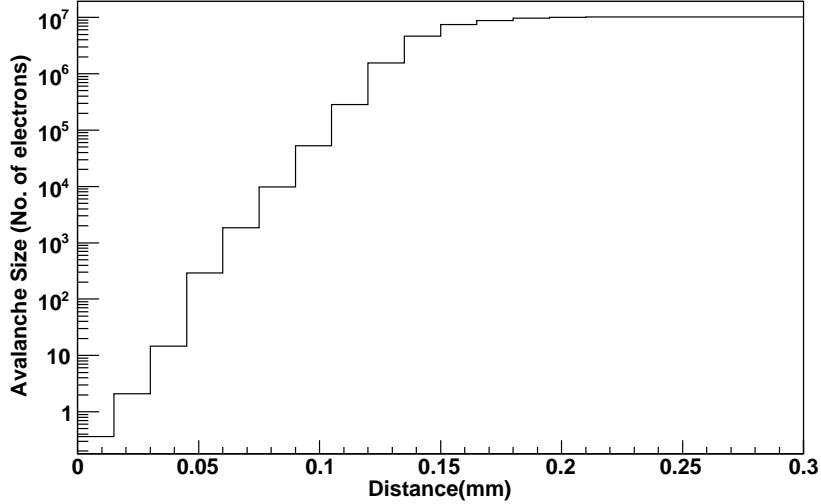
Figure 6.3: The avalanche development inside 0.3 mm gas gap after inclusion of space-charge effect and it is assumed that avalanche saturates when number of avalanche electrons is $\geq 5 \times 10^7$.

the avalanche multiplication process when each individual avalanche size is of the order of $\sim 10^7$ i.e., when number of electrons in an avalanche reaches $\sim 10^7$ in each step of avalanche calculation. The growth of the avalanche inside the 0.3 mm single-gap RPC is shown in figure 6.3. The growth reaches saturation when the number of electrons is $\geq 5 \times 10^7$.

6.3   Induced Signal

Finally the movement of the avalanche electron induces a current signal on the electrodes of the RPC. While simulating the induced current, we have neglected any influence of the signal induced by the positive ions since ions have very low drift velocity.
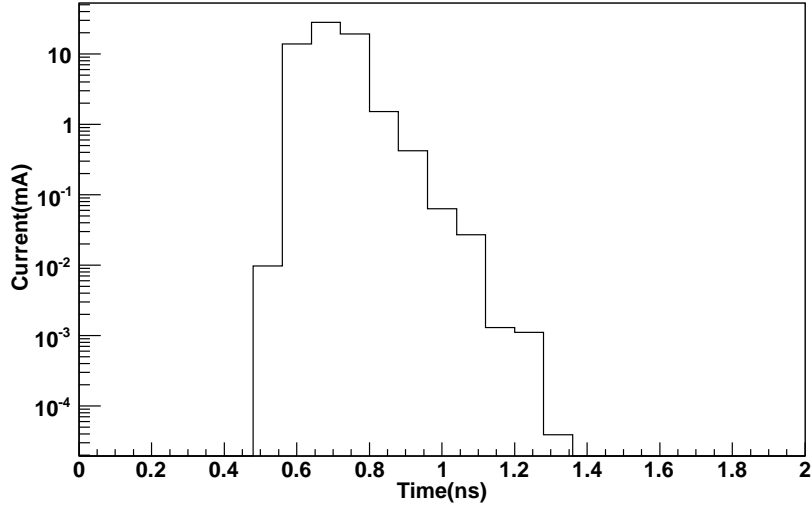
Figure 6.4: The induced current distribution for the single gap RPC, without considering any surface roughness.

The current signal induced on an electrode is given by

$$i(t) = \frac{E_w.v}{V_w} e_0 N(t) \tag{6.14}$$

where e_0 is the electron charge and E_w is the weighting field, the field in the gas gap if we put the electrode to potential V_w and ground all other electrodes, v is the drift velocity and $N(t)$ is the number of avalanche electrons present at a time t. $N(t)$ is obtained by simulating the avalanche development starting from a single primary electron at time $t = 0$. The distribution for induced current the single-gap RPC is shown in figure 6.4.

The weighting field calculated for the single-gap RPC having geometry like shown in figure 6.5 is:

$$\frac{E_w}{V_w} = \frac{\varepsilon_r}{2b + d\varepsilon_r} \tag{6.15}$$

107
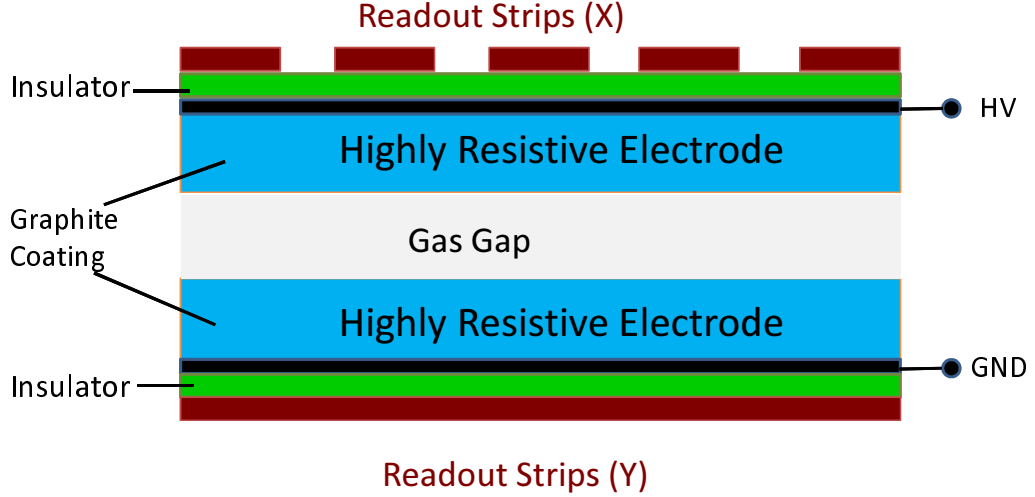
Figure 6.5: The internal structure of a single gap Bakelite RPC, shown schematically.

where ε_r is the Bakelite permittivity, b is the Bakelite thickness and d is the thickness of the gas gap. In this study the following values are used:

$$\varepsilon_r = 8 \text{ for Bakelite}, b = 2\text{mm}, d = 0.3\text{mm} \tag{6.16}$$

The weighting field is calculated in the following way: the electric fields E_i at i^{th} layer in a capacitor with n number of layers of thickness d_i and permittivity ε_i can be calculated by the conditions

$$\sum_{i=1}^{n} E_i d_i = V_w, \varepsilon_i E_i = \varepsilon_j E_j \tag{6.17}$$

for neighboring layers. To get an idea about the induced signal, we start the avalanche process from a single electron and for the present RPC configuration, the weighting field calculated is 1.25/mm. Figure 6.6 shows the induced charge spectrum for the timing RPC with 20 fC threshold.

The glass RPCs have excellent surface uniformity and no surface treatment is required. Whereas the surface profile of Bakelite is not smooth like glass. The non-uniform
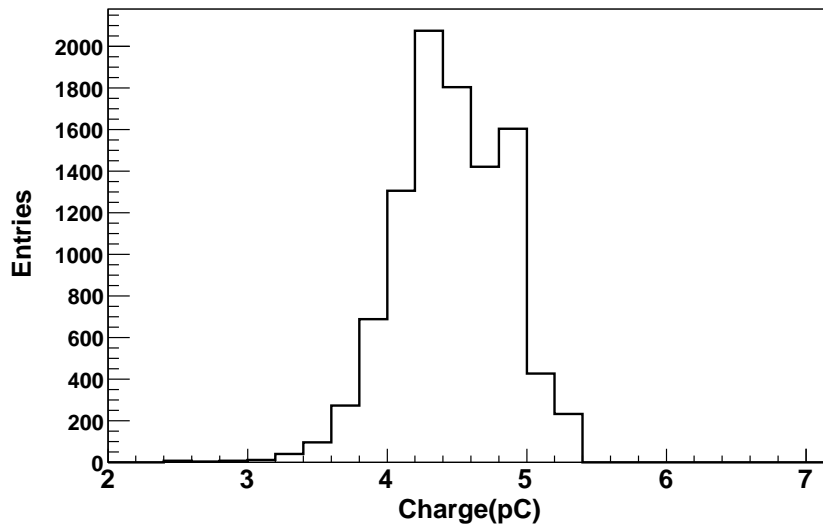
Figure 6.6: Charge spectrum for the timing RPC, considering the avalanche saturation at $N(t) \sim 5 \times 10^7$.

surface of RPC electrodes can have two types of effects: (a) sharp edge will likely to produce discharges thereby reducing the efficiency and (b) resulting fluctuation in the gap between two electrodes will introduce the localized variation in the electric field causing the effect on the performance of the detector. This perturbation of field influence the time resolution as well as the efficiency of RPC. In the following subsection we will discuss the procedure adopted to study the effect of fluctuation of the width of the gas gap.

6.3.1 Roughness simulation

As mentioned earlier, two different grades of bakelites are used to develop RPCs for INO iron calorimeter prototype. In figure 6.7, we have shown the surface profiles of three different grades of bakelite materials which are P-120, Superhylam and P-1001.

109

Table 6.1: Variation in roughness for three different grade bakelite materials.

Grade	Longe Range Variation (μm)	Short range Variation (μm)
P-120	0.84±0.12	0.64±0.06
Superhylam	0.49±0.17	0.17±0.02
P-1001	0.88±0.09	0.63±0.13

Among the three grades, P-1001 grade bakelite was not used for building RPCs because of the low resistivity of the material. A DekTek 117 Profilometer is used to scan the surface profile for each of the bakelite grades and the distribution of the experimentally measured heights on the surfaces is shown in figure 6.7. During the procedure, the profilometer pointer touches at 2000 equidistant points over a 5mm long bakelite sheet and the first point of measurement is referred to as the zero reference level. The successive values of surface heights are measured positive and negative depending on the position of the pointer about the reference level. As shown in figure 6.7, the variation of the heights measured by the profilometer has following features (a) when the measured heights are binned in the scale of $\sim 1\mu m$, the shape of the variation of heights along the direction of scan shows fluctuations in a long range scale and the RMS of the distribution of heights (in $\sim 1\mu m$ scale) is called "long range variation" of surface heights and (b) the distribution of the measured heights when binned in
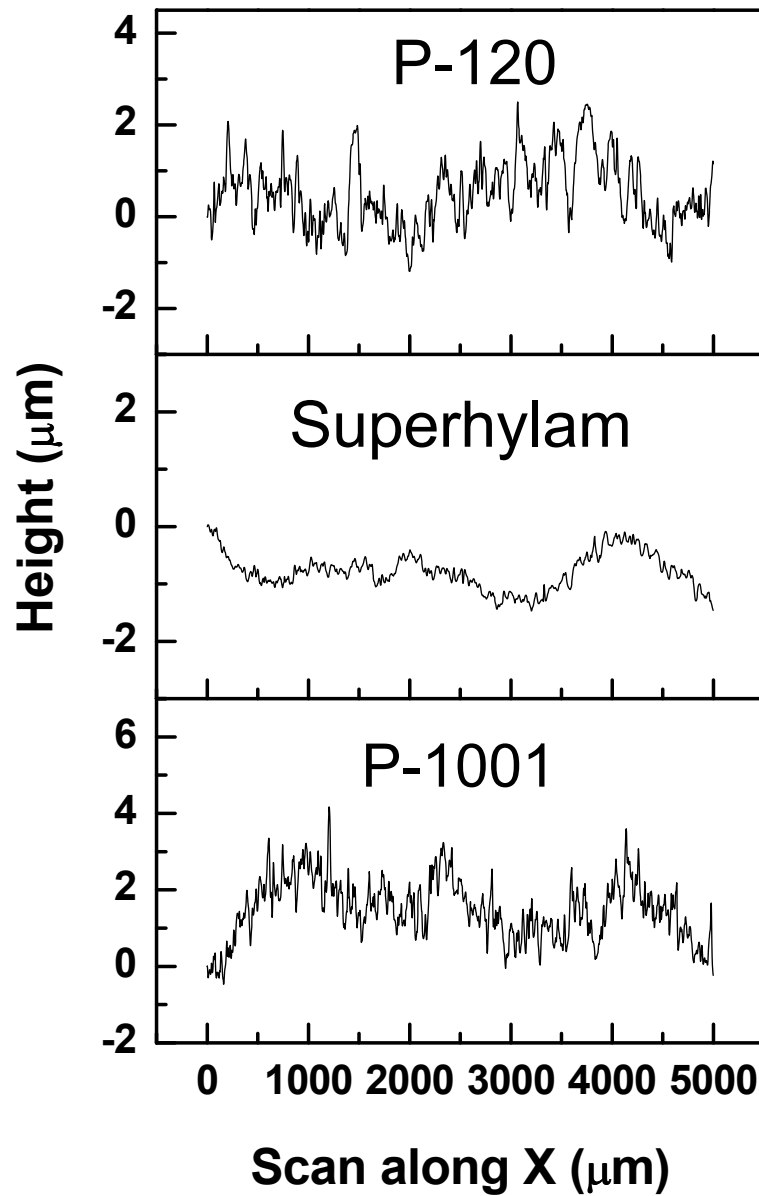
Figure 6.7: The fluctuations in surface heights for three different grades of bakelite materials as measured by a DekTek 117 Profilometer.
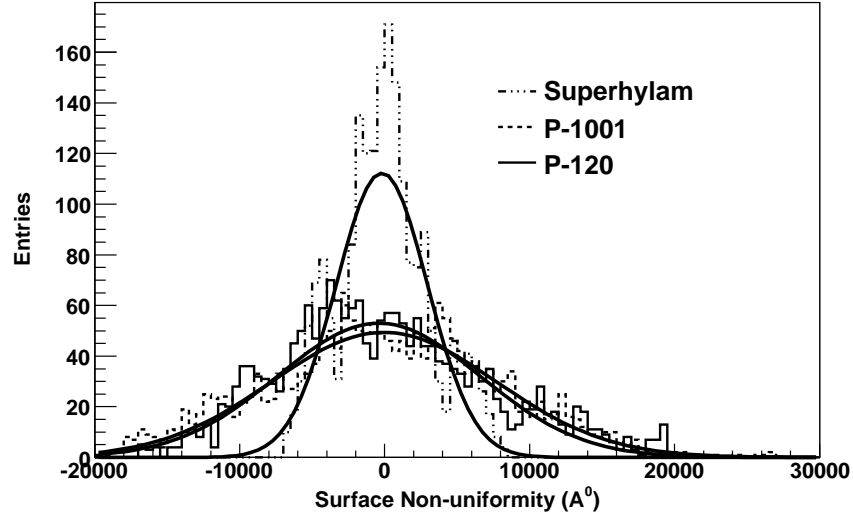
Figure 6.8: The distributions of surface heights for three different grades of bakelite.

the scale of $\sim 0.1 \mu m$ shows fluctuating behavior when inspected along the direction of scan. This small scale variation as measured by RMS of the distributions of heights (binned in the scale of $\sim 0.1 \mu m$) is called "short range variation" of surface heights. The values of "long range variation" and "short range variation" in terms of RMS of surface heights distribution are tabulated in table 6.1. As shown in figure 6.7, the wavy nature along the direction of scan, representing long range variations exist in all three grades, however the localized variation is considerably small for glossy finished superhylam grade. The distribution of the measured heights centered at zero, by proper shifting of the mean is shown in figure 6.8. The RMS values of these distributions represent the roughness for three grades of bakelite. It is clearly seen that the roughness represented by the RMS of each distribution is minimum for the superhylam grade and similar for other two grades. In this work we have considered the shape of the surface roughness profile of P-120 grade bakelite to model the roughness for the simulation. It should be mentioned that the field variations due to the fluctuation in gap width, affecting

112

the avalanche could be discussed in various scales, including the avalanche transverse scale.

Another process which affects the avalanche is the diffusion of ions and electrons. Diffusion effects is small compared to the effects due to drift and the diffusion can be represented by a macroscopic diffusion coefficient giving rise to additional diffusion current densities:

$$J_e = -D_e \Delta \rho_e$$
$$J_p = -D_p \Delta \rho_p \tag{6.18}$$

where J_e, J_p represent current densities due to electrons and positive ions respectively. The diffusion coefficients for electrons (D_e) and for positive ions (D_p) are approximately given by:

$$D_e = \frac{\lambda_e v_e}{3}$$
$$D_p = \frac{\lambda_p v_p}{3} \tag{6.19}$$

where v_e, v_p and λ_e, λ_p are the drift velocities and mean free path for electrons and positive ions respectively. If we consider the effects due to electrons only, then the diffusion of electrons in a gas occurred due to random collisions with gas atoms due to thermal motion. A free electron in a gas occupies energy following the Maxwell-Boltzmann distribution, with mean $< E >= 3/2kT \approx 40\text{MeV}$, where k is the Boltzmann constant and T is the room temperature in Degree-Kelvin. In absence of any external field, the diffusion has Gaussian distribution and is isotropic in nature. Hence, a cloud of electrons that is point-like at a position $\vec{r_0}$ at time t_0, will diffuse according to:

$$\varphi_{isotr}(\vec{r}, t) = \frac{1}{\left(\sqrt{2\pi}\sigma(t)\right)^3} e^{\left(-\frac{(\vec{r}-\vec{r_0})^2}{2\sigma(t)^2}\right)} \tag{6.20}$$

In presence of electric field, the diffusion becomes anisotropic and one can separate the longitudinal (D_l) and transverse (D_t) components of diffusion coefficient, depending

on whether the spread of diffusion is in the direction of field or perpendicular to it. Then equation 6.20 becomes:

$$\varphi_{isotr}(r,z,t) = \frac{1}{\sqrt{2\pi}\sigma_l\sigma_t^2}e^{(-\frac{(z-z_0)^2}{2\sigma_l^2}-\frac{(r-r_0)^2}{2\sigma_t^2})} \tag{6.21}$$

where z_0 and r_0 are the positions of the centre of mass of the distribution. Equation 6.21 shows that the spread of the diffusion is gaussian with width σ and dependent on the drift distance L. Here, assuming a constant drift velocity $v_D = L/t$, we will get $\sigma_{l,t} = \sqrt{2\overline{D}_{l,t}t} = D_{l,t}\sqrt{L}$ [98]. The separate distributions for the longitudinal and transverse distributions will be respectively [98] :

$$\varphi_l(z,L) = \frac{1}{\sqrt{2\pi L}D_l}e^{\left(-\frac{(z-z_0)^2}{2D_l^2 L}\right)} \tag{6.22}$$

$$\varphi_t(r,L) = \frac{1}{D_t^2 L}e^{\left(-\frac{(r-r_0)^2}{2D_t^2 L}\right)} \tag{6.23}$$

If we assume that the transverse and longitudinal diffusion coefficients are equal and considering the picture of pure diffusion, the avalanche diffuses in space with an average radius $\sigma_D = D_t.\sqrt{g}$ [98, 99], which is of the order of $1\mu m$ for the given gas mixture and 0.3mm gas gap. Where D_t is calculated from MAGBOLTZ [100], shown in figure 6.9 and g is the gap width. In the current discussion therefore, the measured long range variation of roughness is in the avalanche transverse scale.

The distribution of the surface heights is gaussian in nature, as shown in figure 6.8. We have therefore incorporated this gaussian distribution of surface non-uniformity in the simulation and sigma of the distribution is the measure of the roughness. The fluctuation of the width of the gas gap will have an impact on the field inside the RPC. It is assumed that the perturbation in the field is only due to the non-uniformities in the gap size g and under this assumption, the RMS variation of field relative to the mean becomes equal to the RMS variation of gap i.e.,

$$\bar{E}_{gap} = E \quad \text{and} \quad \frac{rms_E}{E} = \frac{rms_g}{g}. \tag{6.24}$$

114
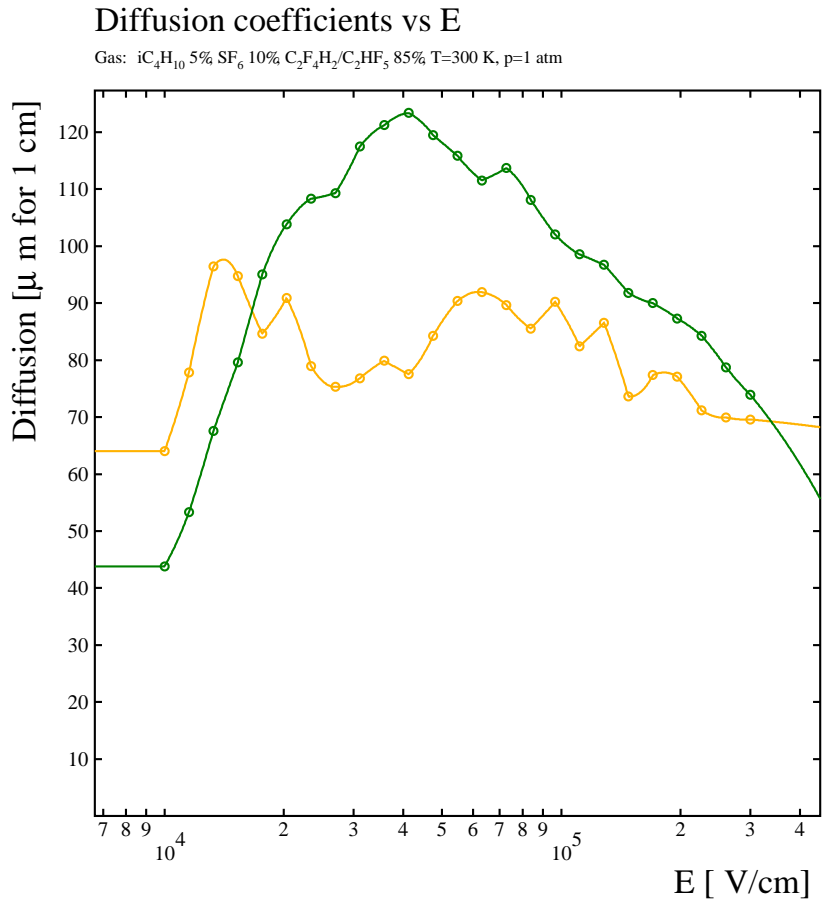
Figure 6.9: Longitudinal (orange line) and transverse (green line) diffusion coefficients calculated by MAGBOLTZ [100] for the given gas mixture.

While simulating the electric field variation inside the gas gap of the detector, we generate gaussian random numbers with sigma as the fluctuation in the field. As a consequence, the sigma of the field variation will represent the sigma of the non-uniform surface profile distribution.

The variation of the electric field E due to gas gap fluctuation will thus influence the Townsend coefficient and the attachment coefficient, as shown in figure 6.10. Similarly, the drift velocity of electrons will also change with varying field, which is shown in
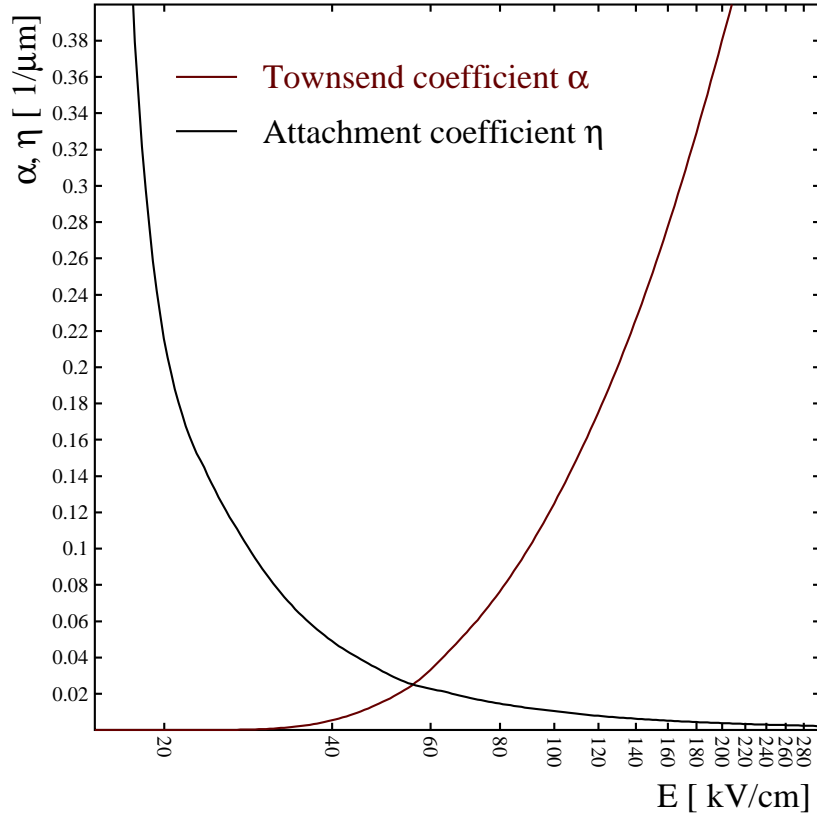
Figure 6.10: Townsend and attachment coefficients as obtained from MAGBOLTZ [100] for a mixture of $C_2F_4H_2$, $i-C_4H_{10}$, SF_6 gases in $85 : 5 : 10$ ratio.

figure 6.11. As a consequence, the perturbed field will affect the avalanche growth according to equation 6.7 & 6.8. Finally it will influence the induced signal as well as the charge spectrum of the RPC.

Since the time resolution σ_T is the second moment of RPC time response, it is expected that σ_T will have an impact due to the fluctuations of the voltage across the gas gap.
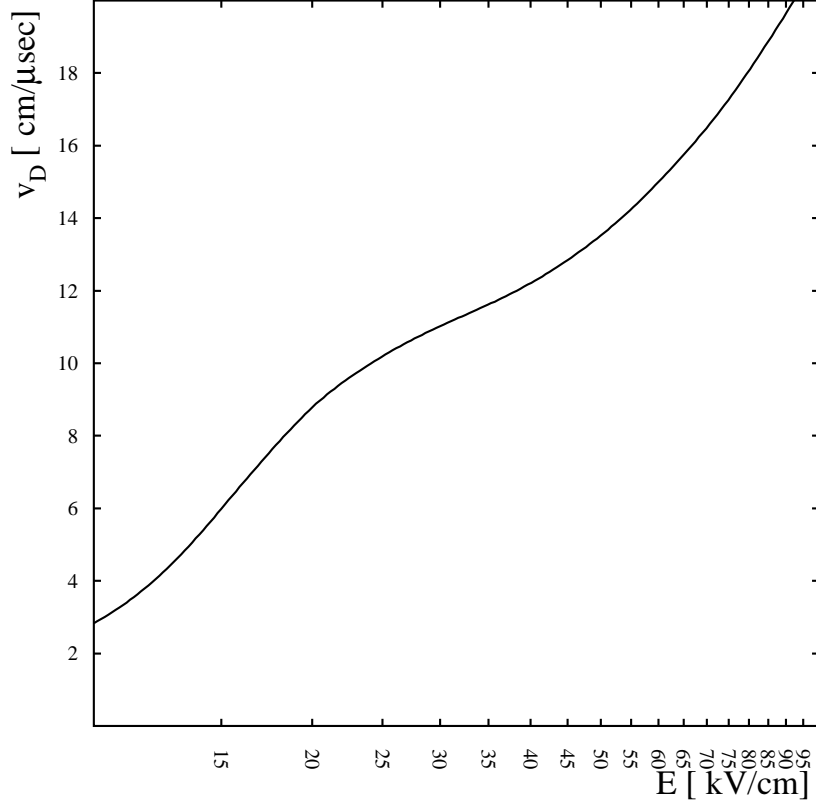
Figure 6.11: Variation of drift velocity with electric field as predicted by MAG-BOLTZ [100] for $C_2F_4H_2/i - C_4H_{10}/SF_6$ gas mixture in 85/5/10 ratio.

The influence of small fluctuations can be estimated [101]:

$$rms_T{}^2 = \left[\frac{K^2}{S^2} + t_0{}^2 \left(\frac{E}{S} \frac{dS}{dE} \right)^2 \left(\frac{rms_E}{E} \right)^2 \right]_{\bar{E}_{gap}} \qquad (6.25)$$

where $\frac{K^2}{S^2}$ governs the intrinsic timing resolution due to intrinsic avalanche fluctuations of RPC and $t_0{}^2 \left(\frac{E}{S} \frac{dS}{dE} \right)^2 \left(\frac{rms_E}{E} \right)^2$ term is added for the dynamic fluctuation of the electric field (i.e. rms_E) inside the gas gap. Description about other parameters in equation 6.25 is in Ref. [102].

The procedures adopted for the Monte Carlo simulation are as follows:

1. The gas gap of size g is divided into N steps of size $\Delta x = g/N$, which corresponds to time step $\Delta t = \Delta x/v$, where $v = v_D(E_0/p)$ is the electron drift velocity obtained from figure 6.11 at the applied electric field strength E_0 and gas pressure p.

2. The number of primary clusters are distributed onto steps following a poisson distribution with mean equal to the number of clusters inside a 0.3 mm gas gap. The first cluster is put at a distance from the cathode, which is obtained by generating the exponential random number with mean equal to the mean free path $(= 0.1mm)$. The second cluster is placed at a distance from the first one, calculated in similar way. This procedure repeated until the anode is reached.

3. Primary electrons are put to each cluster following the cluster size distribution given in figure 6.1.

4. The Townsend coefficient $\alpha(E_0/p)$ and the attachment coefficient $\eta(E_0/p)$ and the drift velocity $v = v_D(E_0/p)$ values are obtained for a particular electric field E_0 from the figures 6.10 & 6.11.

5. The avalanche development is simulated according to the equations 6.7 & 6.10 and the growth is stopped when $N(t)$ attains the saturation value of 5×10^7. This procedure simulates the space charge effect.

6. At each time step, the current induced by the drifting electrons is calculated and induced currents at different steps are summed up to obtain the induced charge.

7. To study the effect of surface roughness of Bakelite electrodes on the performance of the timing RPC under consideration, a Gaussian distribution of surface heights fluctuations is assumed, this shape is modelled from the experimentally

measured values. The random numbers which follows Gaussian distribution are generated and sigma of the distribution is the measure of roughness on the surface of electrodes.

8. The average field inside the RPC is varied linearly with the average variation in gas gap according to equation 6.24 and as a consequence the Townsend coefficient, the attachment coefficient and the drift velocity are obtained for varying electric field from the figures 6.10 & 6.11.

9. Finally the time resolution for different degree of roughness is calculated from the RMS of the time spectrum for 20 fC threshold and the simulated result is compared with the time resolution obtained from analytic calculations according to equation 6.25.

6.4   Results

Considering all the physics processes, we obtained $\approx$ 80 ps time resolution and 99% efficiency at a 20 fC threshold for the 0.3 mm single-gap timing RPC, for a smooth surface. As a next step, the effect of the rough surfaces of the RPC electrodes on the performance of RPC has been studied. The variation of the time resolution σ_T obtained from the simulation study are compared with the analytically calculated values, which is shown in figure 6.12. It is observed that 4% variation in roughness causes $\approx$ 30% variation in time resolution and this result is compatible with the analytically obtained results. However, above 5% fluctuation of the field the Monte Carlo results show larger variation in time resolution compared to that of the analytical results. Whereas, the efficiency of the detector does not change considerably upto 10% average roughness
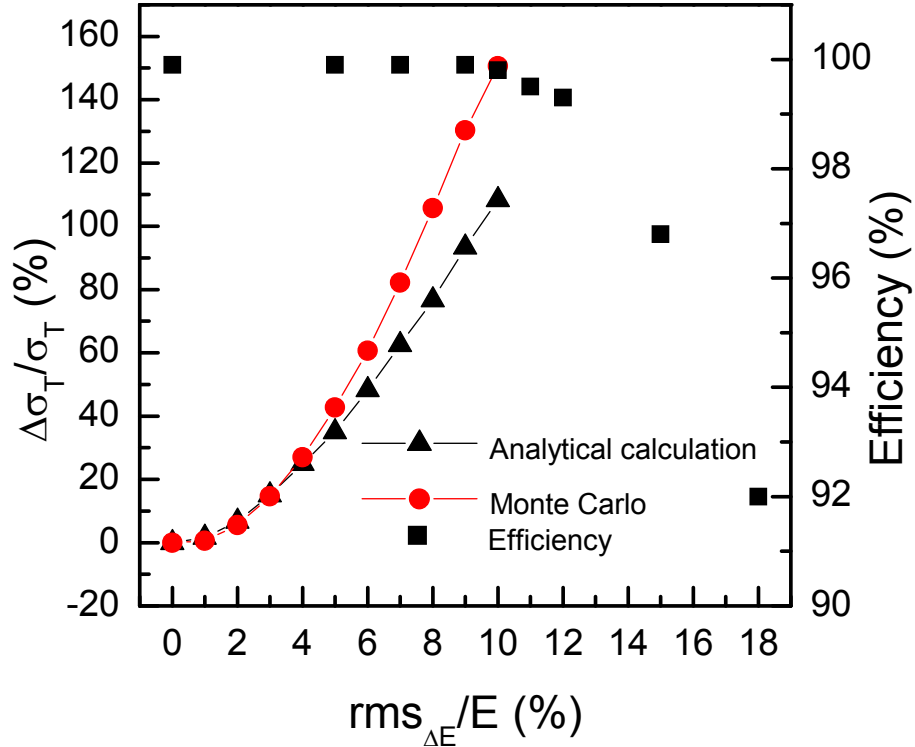
Figure 6.12: The variation of efficiency as well as time resolution of the timing RPC due to variation in electric field inside the RPC gas gap, arises due to the fluctuation in surface heights of the RPC electrodes. The simulated values are compared with those of the analytically obtained results from Ref. [102]

of the surface of the electrodes as shown in figure 6.12. There is a 10% decrease in efficiency for 20% overall variation in surface profile.

6.5   Summary

We present a Monte Carlo method which simulates the physics processes when a charged particle passes through a RPC operating in avalanche mode. We show the results for a 0.3 mm single-gap timing RPC. Our main motivation was to analyze the

effect of the non-uniformity of the surface on the performance of RPC. We assume that the average roughness in surface is Gaussian in nature which has been verified by the distribution of experimentally measured surface heights of bakelite. The fluctuation in the electric field is assumed to be equivalent to the variation in gap size i.e. $\frac{rms_E}{E} = \frac{rms_g}{g}$ under the assumption that the electric field is only influenced by the surface profile. It is observed that the field inside the gap is worsened by $\sim$30 % for 4 % variation in gap thickness and this result is comparable with the analytically obtained results. Finally, we show that a 20 % variation of the field causes 10 % worsening of efficiency.

Chapter 7

Summary and Conclusions

The phenomena of neutrino oscillation, the explanation of which needs neutrino to have a non-zero mass takes us beyond the standard model. The neutrino physics therefore has opened up a new horizon with a series of new and exciting possibilities. Even though, over the years by a series of challenging experiments, the existence of neutrino oscillation is established beyond doubt, however mapping the exciting world of neutrino physics requires the precision measurements of different landmarks in the neutrino mass matrix e.g., three mixing angles and two mass-squared differences apart from the exotica like fourth family of neutrino.

A series of new experiments are planned, which will take data with different neutrino sources e.g., atmospheric neutrino, accelerator neutrino etc. One such planned experimental effort is the India-based Neutrino Observatory (INO), which is likely to begin data taking in few years. INO will take data with atmospheric neutrinos in the first phase and plans to accept neutrino beams from CERN at a later stage. The physics agenda for INO includes (a) demonstration of neutrino oscillation pattern by disappearance and appearance of ν_μ through the measurement of the variation of the ratio

of up-going and down-going neutrinos with L/E, (b) precise measurement of $|\Delta m_{23}^2|$ and θ_{23}.

The considerations of (i) precise measurement of neutrino energy (E) and neutrino path length (L) before interaction, (ii) charge identification of muons, (iii) separation of up going and down going neutrinos and (iv) large neutrino events statistics in a reasonable time led to the design of a 50 kTon magnetized iron calorimeter consisting of 140 iron layers. For design development, production and installation of such a large detector system, we need to have a detailed simulation and data reconstruction framework. As a first step towards realization of the project, a prototype has been installed at VECC with a scaled down geometrical configuration. This thesis deals with the topics towards achieving the overall goal of making a framework for ICAL, taking ICAL prototype as a first case. Following topics are covered in this thesis:

1. Simulation by GEANT4: Detailed simulation has been performed for the ICAL prototype in GEANT4 framework. Energy deposition, hits distribution for muons and hadrons have been studied. Even though a GEANT3-based simulation framework exists as a central INO tool, but present work will enable us to keep an alternative and make use of GEANT4 where GEANT3 based description is not adequate e.g., interactions of pions in iron.

2. Event Reconstruction: Reconstruction of a neutrino events has been dealt in two steps (a) discrimination of hadrons and muons hits on every layer by using the Artificial Neural Network (ANN). For events containing both muons and hadrons e.g., CC events, the hadrons traverse few layers after the vertex layers before getting stopped completely, however muons continue to travel for a longer distance, therefore making the first few layers tp contain hits from both types of particles. This property has been utilized in a feed-forward ANN framework,

where training has been performed by using single particle events and interacting neutrino events from NUANCE model. The separation of "muon only events" from CC type events could be achieved upto 98% efficiency with 10% background fraction. The corresponding numbers for isolating hits in first few layers worsens to 67% efficiency and 40% background fraction. The discrimination performance of hits from subsequent layers is considerably improved. (b) The hits identified as muon hits on various layers are then connected to form muon tracks. Charge and momentum of the tracks are to be determined with good precision, as they form important physics variables. We therefore apply a recursive track fitting algorithm known as Kalman Filter (KF) towards achieving this goal. KF is an iterative procedure where measured hits are included at steps for precise determination of the track parameters. The track parameters are described by a state vector, defined as a column matrix containing (x, y, dx/dz, dy/dz, q/p) as elements. Well defined procedures are adopted to propagate the track from one layer to other thereby updating the track parameters by including new measurements. The procedure has the provision to include process and measurement noise while updating the state vector. The momentum of a track can be determined by the optimized q/p parameter at the first layer considered as vertex. We have applied the method to reconstruct tracks from the simulated hits by cosmic muons on ICAL prototype. We have seen that for fully contained tracks, a momentum resolution of 15% and a linearity between incident and reconstructed track momenta have been achieved. This procedure can be adopted to full scale ICAL data analysis as an extension of the algorithm.

3. Response simulation of the active detectors: The simulation based on GEANT provides energy deposition in the active layers' gas volume as signal. However for a complete response simulation work, one needs to simulate the signal-generation

by active detector layers. In our case, therefore the generation of induced current/charge on RPC-strips needs to be simulated. We have developed a Monte Carlo technique for performing the job. For a 0.3 mm single gap timing RPC, primary ionization and electron generation have been performed using HEED. The formation and propagation of avalanche in presence of the electric field have been simulated, using a formalism based on first the Townsend coefficient, the attachment coefficient, and the saturation due to space charge. Induction and charge collection have been separately formulated. As a result of the implementation of the processes, we obtained time resolution and efficiency of the timing RPC which match with the earlier calculations and measurements. Additionally, we have implemented the roughness of the electrode surfaces in a scale of 1 μm and studied the effect on time resolution and efficiency of the detector. The implementation of the surface roughness was motivated by a measurement of the surface profile of different grades of bakelite, used to built RPCs for ICAL prototype. The long range surface profile follows a Gaussian distribution. After considering the RMS of the distribution as the measure of the roughness, we have introduced different roughness by Gaussian random numbers with varying widths. The final effect on time resolution and efficiency of the roughness shows that the time resolution deteriorates by 30% for a roughness of 4%, while efficiency remains unchanged upto 20% change in roughness and then decreases gradually.

In summary, we have discussed various steps of simulation and reconstruction procedures towards design and data analysis of the ICAL detector in the proposed INO experiment. Different steps are developed independently either for working with ICAL prototype or for ICAL, however these procedures can be seamlessly put together for building a self consistent package for ICAL.

Appendix A

Analytic formulation to calculate propagation of a charged particle in magnetic field

In the Kalman filter track fitting procedure (discussed in chapter 5), an extrapolation formula is used instead of the fourth-order Runge-Kutta method is implemented. The analytic formula for track extrapolation for a charged particle inside magnetic field is discussed here. This analytic formula expands the extrapolated track parameters in a power series of the magnetic field components. The position of a particle can be represented by its position coordinates (x, y), directions $t_x = dx/dz$, $t_y = dy/dz$, signed charge q, and momentum p. All these parameters form a state vector $\mathbf{r}(z) = (x, y, t_x, t_y, q/p)^T$. During particle transportation inside the detector volume, there is propagation of track parameters from one hit point $\mathbf{r}(z_0)$ to the new hit position $\mathbf{r}(z_p)$ i.e., $\mathbf{r}(z_0) \rightarrow \mathbf{r}(z_p)$. In addition to the state vector $\mathbf{r}$, the covariance matrix $C = \langle (\mathbf{r} - \langle \mathbf{r} \rangle).(\mathbf{r} - \langle \mathbf{r} \rangle)^T \rangle$ needs to be extrapolated in the fitting routine. To extrapolate

the covariance matrix, it is only required to derive the extrapolated track parameters $\mathbf{r}(z_p)$ on the initial track parameters $\mathbf{r}(z_0)$. This derivative is calculated in the form of jacobian i.e.,

$$J = \frac{d\mathbf{r}(z_p)}{d\mathbf{r}(z_0)} \tag{A.1}$$

When the jacobian is known, the covariance is extrapolated to the next layer by matrix multiplication

$$C(z_p) = JC(z_0)J^T \tag{A.2}$$

In following section the extrapolation of both the state vector and its' covariance is discussed.

A.1   Equation of motion

The equation of motion for a charged particle moving inside the magnetic field is governed by Lorentz force F and the expression for the force is following:

$$\frac{d\mathbf{p}}{dt} = \mathbf{F} = \kappa.q.\mathbf{v} \times \mathbf{B} \tag{A.3}$$

with momentum $\mathbf{p}[\mathbf{GeV/c}]$, signed charge $q[e]$ i.e. $q = \pm 1$ for μ^+ and μ^- respectively, magnetic field $\mathbf{B}[\mathbf{kG}]$ and the coefficient $\kappa[(\mathrm{GeV/c})\mathrm{kG}^{-1}\mathrm{cm}^{-1}] = 2.9979.10^{-4}$. Since the lorentz force is directed perpendicular to the direction of motion of the charged particle, so $v = |\mathbf{v}|$ and the momentum $p = |\mathbf{p}|$ are constants and the time can be replaced by the trajectory length s as $dt = ds/v$:

$$\mathbf{p} = \mathbf{F} = \kappa.q.\mathbf{v} \times \mathbf{B} \ ds/v \tag{A.4}$$

Introducing a unit vector $\mathbf{e} = \mathbf{v}/v = \mathbf{p}/p$ in the above equation, it becomes

$$d\mathbf{e} = \kappa.q.\mathbf{e} \times \mathbf{B}.ds = \kappa.(q/p). \begin{pmatrix} e_y B_z - e_z B_y \\ e_z B_x - e_x B_z \\ e_x B_y - e_y B_x \end{pmatrix} ds \tag{A.5}$$

127

The equation of motion(A.5) can be used only for particle extrapolation to a certain path length s. However we would like to do the extrapolation at every hit point of the particle track. For that the variable in equation A.5 have to be replaced by the track parameters i.e., by $\mathbf{r}(z) = \mathbf{r}(x, y, dx/dz, dy/dz, q/p)$.

During extrapolation, there is propagation of track parameters occur from one hit point to the next i.e., $\mathbf{r}(z_0) \to \mathbf{r}(z_p)$, for that we need evaluate the derivative of $\mathbf{r}(z)$ with respect to z.

The differentials of the track directions $(t_x = e_x/e_z = \frac{dx}{dz}, t_y = e_y/e_z = \frac{dy}{dz})$ are :

$$
\begin{aligned}
dt_x &= (de_x e_z - e_x de_z)/e_z^2) \\
&= \kappa.(q/p).(e_y e_z B_z - e_z^2 B_y - e_x^2 B_y + e_x e_y B_x)/e_z^2.ds \\
&= \kappa.(q/p).\left(t_y B_z - (1 + t_x^2)B_y + t_x t_y B_x\right).ds, \quad\quad (A.6)
\end{aligned}
$$

$$
\begin{aligned}
dt_y &= \ldots \\
&= \kappa.(q/p).\left((1 + t_y^2).B_x - t_x t_y.B_y - t_x.B_z\right).ds
\end{aligned}
$$

The path length s is replaced by $ds = \sqrt{1 + t_x^2 + t_y^2}.dz$ in equation A.6 and the derivatives[1] of the track parameters with respect to z will be:

$$
\begin{aligned}
x' &= t_x \\
y' &= t_y \\
t_x' &= \kappa.(q/p).\sqrt{1 + t_x^2 + t_y^2}.\left(t_x t_y.B_x - (1 + t_x^2).B_y + t_y.B_z\right) \\
t_y' &= \kappa.(q/p).\sqrt{1 + t_x^2 + t_y^2}.\left((1 + t_y^2).B_x - t_x t_y.B_y - t_x.B_z\right) \quad\quad (A.7) \\
(q/p)' &= 0
\end{aligned}
$$

---

[1] prime denotes derivative with respect to z

So the equation of motion becomes:

$$\frac{d\mathbf{r}(z)}{dz} = \begin{pmatrix} t_x \\ t_y \\ \kappa.(q/p).\sqrt{1+t_x^2+t_y^2}.\,(t_xt_y.B_x - (1+t_x^2).B_y + t_y.B_z) \\ \kappa.(q/p).\sqrt{1+t_x^2+t_y^2}.\,((1+t_y^2).B_x - t_xt_y.B_y - t_x.B_z) \\ 0 \end{pmatrix} = f(z,\mathbf{r}) \quad (A.8)$$

The differential equation is solved by the Runge-Kutta method, by solving the following differential equation:

$$\frac{d\mathbf{r}(z)}{dz} = \mathbf{f}(z,\mathbf{r}) \quad (A.9)$$

The propagated track coordinates $x(z_p), y(z_p)$ can be calculated from the following expression:

$$\begin{aligned} x(z_p) &= x(z_0) + \int_{z_0}^{z_p} t_x(z)dz, \\ y(z_p) &= y(z_0) + \int_{z_0}^{z_p} t_y(z)dz \end{aligned} \quad (A.10)$$

Hence to obtain the extrapolated track parameters, we need to focus only on the extrapolation of the directions t_x, t_y. From equation A.7, we can write:

$$\begin{aligned} t_x' &= \sum_{i_1=x,y,z} \mathbf{B}_{i_1}(z).a_{i_1}(z), \\ t_y' &= \sum_{i_1=x,y,z} \mathbf{B}_{i_1}(z).b_{i_1}(z) \end{aligned} \quad (A.11)$$

Hence the derivatives of track directions are linearly dependent on the magnetic field and the multipliers $a_{i_1}(z), b_{i_1}(z)$ depend on the track directions t_x, t_y only can be represented by:

$$\begin{aligned} \mathbf{a}(z) &\equiv \kappa.(q/p).\sqrt{1+t_x^2+t_y^2}.\,\left(\; t_xt_y, \quad -(1+t_x^2), \quad t_y \right), \\ \mathbf{b}(z) &\equiv \kappa.(q/p).\sqrt{1+t_x^2+t_y^2}.\,\left(\; (1+t_y^2), \quad -t_xt_y, \quad -t_x \right) \end{aligned} \quad (A.12)$$

and the magnetic field $\mathbf{B}(z)$ along the particle trajectory is:

$$\mathbf{B}(z) \equiv \mathbf{B}(x_{\text{track}}(z), y_{\text{track}}(z), z_{\text{track}}(z)) \equiv (B_x(z), B_y(z), B_z(z)). \qquad (A.13)$$

The extrapolated track parameters can be represented by the following form:

$$
\begin{aligned}
x(z_p) &= x(z_0) + \int_{z_0}^{z_p} t_x(z) dz, \\
y(z_p) &= y(z_0) + \int_{z_0}^{z_p} t_y(z) dz, \qquad\qquad\qquad (A.14) \\
t_x(z_p) &= t_x(z_0) + \sum_{k=1}^{n} \sum_{i_1,\dots,i_k=x,y,z} t_{x_{i_1 \dots i_k}}(z_0) \cdot \left(\int_{z_0}^{z_p} B_{i_1}(z_1) \dots \int_{z_0}^{z_{k-1}} B_{i_k}(z_k) dz_k \dots dz_1 \right), \\
t_y(z_p) &= t_y(z_0) + \sum_{k=1}^{n} \sum_{i_1,\dots,i_k=x,y,z} t_{y_{i_1 \dots i_k}}(z_0) \cdot \left(\int_{z_0}^{z_p} B_{i_1}(z_1) \dots \int_{z_0}^{z_{k-1}} B_{i_k}(z_k) dz_k \dots dz_1 \right)
\end{aligned}
$$

The details about the intermediate steps will be available in Ref. [103]. The important thing to note here that in the above formulae the track directions are at initial position z_0 and the magnetic field components are integrated along the particle trajectory.

Now, the field integrals in the analytic expressions A.14 are calculated along the true particle trajectory, which remains unknown initially during the extrapolation process. It is assumed that the field derivatives along x and y-direction i.e., $\partial \mathbf{B}/\partial x, \partial \mathbf{B}/\partial y$ are negligible in the region around the particle trajectory and magnetic field change only along z-direction. And under this consideration the magnetic field in equation A.13 becomes:

$$(B_x(z), B_y(z), B_z(z)) \equiv \mathbf{B}(x_{true}(z), y_{true}(z), z) = \mathbf{B}(x_{approx}(z), y_{approx}(z), z) \quad (A.15)$$

i.e., the field integrals can be calculated along the approximate particle trajectory. Following new variables are introduced:

$$h = \kappa.(q/p).\sqrt{1 + t_x^2(z_0) + t_y^2(z_0)}, \qquad\qquad (A.16)$$

$$A_{i_1...i_k} = t_{x_{i_1...i_k}}(z_0)/h^k, \tag{A.17}$$

$$B_{i_1...i_k} = t_{y_{i_1...i_k}}(z_0)/h^k, \tag{A.18}$$

$$s_{i_1...i_k} = \int_{z_0}^{z_p} B_{i_1}(z_1)... \int_{z_0}^{z_{k-1}} B_{i_k}(z_k)dz_k...dz_1, \tag{A.19}$$

$$S_{i_1...i_k} = \int_{z_0}^{z_p} B_{i_1}(z_1)... \int_{z_0}^{z_{k-1}} B_{i_k}(z_k)dz_k...dz_1. \tag{A.20}$$

Among the above expressions, equations A.20 & A.20 represents the field integrals and other three variables will be used in the jacobian calculation. Introducing the above mentioned notations, the extrapolated track parameters become:

$$t_x(z_p) = x(z_0) + t_x(z_0)(z_p - z_0) + \sum_{k=1}^{n} \sum_{i_1,...,i_k=x,y,z} h^k A_{i_1...i_k} S_{i_1...i_k},$$

$$t_y(z_p) = y(z_0) + t_y(z_0)(z_p - z_0) + \sum_{k=1}^{n} \sum_{i_1,...,i_k=x,y,z} h^k A_{i_1...i_k} S_{i_1...i_k},$$

$$t_x(z_p) = t_x(z_0) + \sum_{k=1}^{n} \sum_{i_1,...,i_k=x,y,z} h^k A_{i_1...i_k} s_{i_1...i_k},$$

$$t_x(z_p) = t_x(z_0) + \sum_{k=1}^{n} \sum_{i_1,...,i_k=x,y,z} h^k B_{i_1...i_k} s_{i_1...i_k} \tag{A.21}$$

During the extrapolation of track using the analytic expression A.21, one needs to calculate the field integrals $s_{i_1...i_k}, S_{i_1...i_k}$ along the particle trajectory.

For the extrapolation of the covariance matrix, one needs to calculate the jacobian. The extrapolation jacobian is:

$$J = \begin{pmatrix} 1 & 0 & \partial x(z_p)/\partial t_x(z_0) & \partial x(z_p)/\partial t_y(z_0) & \partial x(z_p)/\partial(q/p) \\ 0 & 1 & \partial y(z_p)/\partial t_x(z_0) & \partial y(z_p)/\partial t_y(z_0) & \partial y(z_p)/\partial(q/p) \\ 0 & 0 & \partial t_x(z_p)/\partial t_x(z_0) & \partial t_x(z_p)/\partial t_y(z_0) & \partial t_x(z_p)/\partial(q/p) \\ 0 & 0 & \partial t_y(z_p)/\partial t_x(z_0) & \partial t_y(z_p)/\partial t_y(z_0) & \partial t_y(z_p)/\partial(q/p) \\ 0 & 0 & 0 & 0 & 1 \end{pmatrix} \tag{A.22}$$

Hence to calculate the jacobian from equation A.21, the derivatives of $A...$ and $B...$ with respect to $t_x(z_0)$, $t_y(z_0)$ are evaluated.

The coefficients $A_{i_1...i_k}, B_{i_1...i_k}$ and their derivatives are listed below, using the notations $t_x \equiv t_x(z_0)$, $t_y \equiv t_y(z_0)$, $A^{(x)} \equiv \partial A.../\partial t_x$, $A^{(y)} \equiv \partial A.../\partial t_y$, $B^{(x)} \equiv \partial B.../\partial t_x$, and $B^{(y)} \equiv \partial B.../\partial t_y$.

$$
\begin{pmatrix}
A_x, & A_y, & A_z \\
A_{xx}, & A_{xy}, & A_{xz} \\
A_{yx}, & A_{yy}, & A_{yz} \\
A_{zx}, & A_{zy}, & A_{zz}
\end{pmatrix}
=
\begin{pmatrix}
t_x t_y, & -t_x^2 - 1, & t_y \\
t_x(3t_y^2 + 1), & -t_y(3t_x^2 + 1), & 2t_y^2 + 1 \\
-t_y(3t_x^2 + 1), & t_x(3t_x^2 + 3), & -2t_x t_y \\
(t_y^2 - t_x^2), & -2t_x t_y, & -t_x
\end{pmatrix},
$$

$$
\begin{pmatrix}
B_x, & B_y, & B_z \\
B_{xx}, & B_{xy}, & B_{xz} \\
B_{yx}, & B_{yy}, & B_{yz} \\
B_{zx}, & B_{zy}, & B_{zz}
\end{pmatrix}
=
\begin{pmatrix}
t_y^2 + 1, & -t_x t_y, & -t_x \\
t_y(3t_y^2 + 3), & -t_x(3t_y^2 + 1), & -2t_x t_y \\
-t_x(3t_y^2 + 1), & t_y(3t_x^2 + 1), & 2t_x^2 + 1 \\
-2t_x t_y, & (t_x^2 - t_y^2), & -t_y
\end{pmatrix},
$$

$$
\begin{pmatrix}
A_x^{(x)}, & A_y^{(x)}, & A_z^{(x)} \\
A_{xx}^{(x)}, & A_{xy}^{(x)}, & A_{xz}^{(x)} \\
A_{yx}^{(x)}, & A_{yy}^{(x)}, & A_{yz}^{(x)} \\
A_{zx}^{(x)}, & A_{zy}^{(x)}, & A_{zz}^{(x)}
\end{pmatrix}
=
\begin{pmatrix}
t_x y, & -2t_x, & 0 \\
(3t_y^2 + 1), & -6t_x t_y, & 0 \\
-6t_x t_y, & (9t_x^2 + 3), & -2t_y \\
-2t_x, & -2t_y, & -1
\end{pmatrix},
\tag{A.23}
$$

$$
\begin{pmatrix}
A_x^{(y)}, & A_y^{(y)}, & A_z^{(y)} \\
A_{xx}^{(y)}, & A_{xy}^{(y)}, & A_{xz}^{(y)} \\
A_{yx}^{(y)}, & A_{yy}^{(y)}, & A_{yz}^{(y)} \\
A_{zx}^{(y)}, & A_{zy}^{(y)}, & A_{zz}^{(y)}
\end{pmatrix}
=
\begin{pmatrix}
t_x, & 0, & 1 \\
6t_x t_y, & -(3t_x^2 + 1), & 4t_y \\
-(3t_x^2 + 1), & 0, & -2t_x \\
2t_y & -2t_x, & 0
\end{pmatrix},
$$

$$
\begin{pmatrix}
B_x^{(x)}, & B_y^{(x)}, & B_z^{(x)} \\
B_{xx}^{(x)}, & B_{xy}^{(x)}, & B_{xz}^{(x)} \\
B_{yx}^{(x)}, & B_{yy}^{(x)}, & B_{yz}^{(x)} \\
B_{zx}^{(x)}, & B_{zy}^{(x)}, & B_{zz}^{(x)}
\end{pmatrix}
=
\begin{pmatrix}
0, & -t_y, & -1 \\
0, & -(3t_y^2 + 1), & -2t_y \\
-(3t_y^2 + 1), & 6t_x t_y, & 4t_x \\
-2t_y, & 2t_x, & 0
\end{pmatrix},
$$

$$
\begin{pmatrix}
B_x^{(y)}, & B_y^{(y)}, & B_z^{(y)} \\
B_{xx}^{(y)}, & B_{xy}^{(y)}, & B_{xz}^{(y)} \\
B_{yx}^{(y)}, & B_{yy}^{(y)}, & B_{yz}^{(y)} \\
B_{zx}^{(y)}, & B_{zy}^{(y)}, & B_{zz}^{(y)}
\end{pmatrix}
=
\begin{pmatrix}
2t_y, & -t_x, & 0 \\
(9t_y^2 + 3), & -6t_x t_y, & -2t_x \\
-6t_x t_y, & (3t_x^2 + 1), & 0 \\
-2t_x, & -2t_y, & -1
\end{pmatrix}.
$$

The analytic formula discussed here, is independent of the shape of the magnetic field. The general formula for track extrapolation is a bit cumbersome, however it becomes simple when a particular magnetic field makes many coefficients negligible. In our code we have used the following parameters:

$$
s_y = \int_{z_0}^{z_p} B_y(0, 0, z1) dz_1, \tag{A.24}
$$

$$
S_y = \int_{z_0}^{z_p} \int_{z_0}^{z} B_y(0, 0, z1) dz_1 dz, \tag{A.25}
$$

$$
\kappa = 2.99792458.10^{-4} \tag{A.26}
$$

Here s_y, S_y are the field integrals and it is considered that the B_y component of magnetic field is most dominating and hence influence the particle trajectory.

Bibliography

[1] N. Solomey, "The Elusive Neutrino", (Scientific American Library,1997), pp.16-17.[check]

[2] F. Reines and C.L.Cowan, Phys. Rev. **92**, (1953) 830.

[3] M. Goldhaber *et al.*, Phys. Rev. **109**, (1958) 1015.

[4] G. Danby *et al.* Phys. Rev. **9**, (1962) 36.

[5] K. Kodama *et al.* [DONUT Collaboration], Phys. Lett. **B 504**, (2000), 218.

[6] Z.Maki *et al.*, Prog. Theor. Phys. **28**, (1962), 870.

[7] V. Gribov and B. Pontecorvo, Phys. lett. B **28**, (1969), 493.

[8] Scott M. Oser, arXiv:hep-ex/0604021v1.

[9] Chistopher W. Walter arXiv: 0810.3937v1[hep-ex].

[10] B. Pontecorvo, J. Exp. Theor. Phys. **26**, (1968) 984.

[11] Mauro Mezzetto and Thomas Schwetz, arXiv:1003.5800v1 [hep-ph].

[12] L.Wolfenstein, Phys. Rev. D **17**, 1978 2369; S.P.Mikheev *et al.*, J. Nucl. Phys. **42**, 1985 913.

[13] S. Geer, Phys. Rev. D **57**, (1998), 6989.

[14] Raj Gandhi *et al.*, Phys. Rev. D **75**, (2007), 053002.

[15] S.M.Bilenky and S.T.Petcov, Rev. Mod. Phys. **59**, (1987) 671.

[16] V.C.Rubin and W.K.Ford, Astrophys. J. **159**, (1970) 379; T.S.van Albada *et al.*, Astrophys. J. **295**, (1985) 305.

[17] J.N.Bahcall and M.H.Pinsonneault, Rev. Mod. Phys. **67**, (1995) 1; A.Dar and G.Shaviv, Astrophys. J. **468**, (1996) 933.

[18] K.S.Hirata *et al.*, Phys. lett. B **280**, (1992), 146; Y.Fukuda *et al.*, Phys. lett. B **335**, (1994), 237; R. Becker-Szendy *et al.*, Phys. Rev. D **46**, (1992), 3720.

[19] Y.Fukuda *et al.*, Phys. Rev. Lett. **81**, (1998), 1562;Y.Fukuda *et al.*, Phys. Rev. Lett. **82**, (1999), 2644.

[20] B. T. Cleveland *et al.*, Astrophysics. J. **496** (1998), 505.

[21] T. Araki *et al.*, Phys. Rev. Lett. **94**, (2005), 081801.

[22] Y. Ashie *et al.* [Super-Kamiokande Collaboration], Phys. Rev. **D71**,(2005),112005; Y. Ashie *et al.*, Phys. Rev. Lett. **93**, (2004), 101801.

[23] M. Altmann *et al.* [GNO Collaboration], Phys. Lett. **B616**, 174 (2005), hep-ex/0504037.

[24] J. Hosaka *et al.* [Super-Kamiokande Collaboration], Phys. Rev. **D73**, 112001 (2006), hep-ex/0508053.

[25] Q. R. Ahmad *et al.* [SNO Collaboration], Phys. Rev. Lett. **89**, 011301 (2002), nucl-ex/0204008.

[26] B. Aharmim *et al.* [SNO Collaboration], Phys. Rev. Lett. **101**, 111301 (2008), 0806.0989.

[27] B. Aharmim *et al.* [SNO Collaboration], (2009), 0910.2984.

[28] C. Arpesella *et al.* [Borexino Collaboration] , Phys. Rev. Lett. **101**, (2008), 091302.

[29] T. Araki *et al.* [KamLAND Collaboration], Phys. Rev. Lett. **94**, 081801 (2005), hep-ex/0406035.

[30] S. Abe *et al.* [KamLAND Collaboration] , Phys. Rev. Lett. **100**, (2008),221803.

[31] M. H. Ahn *et al.* [K2K Collaboration], Phys. Rev. **D74**, (2006),072003 [hep-ex/0606032].

[32] P. Adamson *et al.* [MINOS Collaboration], Phys. Rev. Lett. **101**, (2008), 131802.

[33] T. Schwetz, M. A. Tortola, and J. W. F. Valle, New J. Phys. **10**, 113011 (2008), 0808.2016.

[34] G. L. Fogli, E. Lisi, A. Marrone, A. Palazzo, and A. M. Rotunno, Phys. Rev. Lett. **101**,(2008),141801 .

[35] M. C. Gonzalez-Garcia, M. Maltoni, and J. Salvado, (2010), 1001.4524.

[36] G. L. Fogli, E. Lisi, A. Marrone, A. Palazzo, and A. M. Rotunno, (2009), 0905.3549.

[37] Mauro Mezzetto *et al.*, J. Phys. G: Nucl. Part. Phys. **37**, (2010), 103001.

[38] M. Apollonio *et al.* [CHOOS Collaboration] , Eur. Phys. J. **C27**, (2003),331 [hep-ex/0301017].

[39] F. Boehm *et al.*, Phys. Rev. **D64**, (2001),112001 [hep-ex/0107009].

[40] C. Athanassopoulos *et al.*, Phys. Rev. Lett. **75**, (1995), 2650; J.E.Hill *et al.*, Phys. Rev. Lett. **75**, (1995), 2654.

[41] M. Maltoni *et al.*, Nucl. Phys. B **643**, (2002), 321.

[42] H. Ray, Int. J. Mod. Phys. A **20**, (2005), 3062.

[43] Debajyoti Choudhury *et al.*, hep-ph arXiv:1007.2923v1.

[44] M. Guler *et al.*,CERN-SPSC-2000-028,LNGS P25/2000;

[45] N.Agafonova *et al.*, hep-ex arXiv:1006.1623v1.

[46] INO Project Report INO/2006/01, June 2006, (http://www.imsc.res.in/ ino/).

[47] P. Zucchelli, Phys. Lett.**B 532**, (2002) 166.

[48] P. Billoir, Nucl. Instr. and Meth. A **225**, (1984) 352 ; R. Fruhwirth, *ibid.* **262**, (1987) 444.

[49] R. Santonico and R. Cardarelli, Nucl. Instr. and Meth. A **187**, (1981) 377.

[50] Sanjib Kumar Agarwalla thesis, University of Calcutta, 2008.

[51] B. Pontecorvo, J. Exp. Theor. Phys. **33**, (1957) 549.

[52] B. Pontecorvo, J. Exp. Theor. Phys. **34**, (1958) 247.

[53] Abhijit Samanta *et al.*, Int. J. Mod. A **23**, (2008) 233.

[54] D. G. Micheal *et. al.* [MINOS Collaboration], Phys. Rev. Lett. **97**, (2007) 191801.

[55] P. Picchi and F. Pietropaolo, CERN preprint SCAN-9710037.

[56] J. Ying *et. al.*, J. Phys. G : Nucl. Part. Phys.**26**, (2000) 1291.

[57] P. Camarri *et. al.*, Nucl. Instr. and Meth. A **414**, (1998) 317.

[58] R. Cardarelli *et. al.*, Nucl. Instr. and Meth. A **333**, (1993) 399.

[59] "Techniques for Nuclear and Particle Physics Experiments", William R. Leo, Springer International Edition, 2010.

[60] P.Fonte, *et. al.*, ICFA instrumentation bulletin, 1997.

[61] S.D.Kalmani *et al.*, Nucl. Instr. and Meth. A **602**, (2009) 845.

[62] Anita Behere *et al.*, Nucl. Instr. and Meth. A **602**, (2009) 784.

[63] GEANT4 - a simulation toolkit, S. Agostinelli *et al.*, Nucl. Instr. and Meth. A **506**, (2003) 250.

[64] Tapasi Ghosh, Subhasis Chattopadhyay, and Saikat Biswas. Proceedings of the DAE Symposium on Nuclear Physics, Vol. **53**, (2008) 769.

[65] Thomas Hebbeker and Charles Timmermans, Astroparticle Physics **18**, 107 (2002).

[66] C. Amsler *et al.*, Physics Letters B **667**, (2008) 1.

[67] P. Billoir, Nucl. Instr. and Meth. A **225**,(1984) 352; R. Fruhwirth, *ibid.* **262**,(1987) 444.

[68] NEMO Collaboration, NEMO-3 Proposal, Preprint LAL 94-29, 1994.

[69] T. Toffoli ans N. Margolus, Cellular Automata Machines: AA New Environment for Modelling (MIT Press, Cambridge, MA, 1987).

[70] I. Kisel *et al.* Nucl. Instr. and Meth. A **387**,(1997) 433.

[71] A. Carvera *et al.* Nucl. Phys. B **579**, (2000) 17.

[72] MONOLITH Proposal, LNGS P26/2000, CERN/SPSC 2000-031, August 2000 (http://castore.mib.infn.it/ monolith/proposal/).

[73] G. Bari *et al.* Nucl. Instr. and Meth. A **508**,(2003) 170.

[74] MINOS proposal Chapter 7: Simulation of Detector Response.

[75] A. Cervera *et al.* arXiv:1004.0358.

[76] Technical Status Report (2005), CBM experiment at FAIR, GSI, Germany.

[77] M. C. Bishop, *Neural Network for Pattern Recognition*, Oxford, 1995.

[78] Simon Haykin, *Neural Network A Comprehensive Foundation*, Pearson Education, 2004.

[79] S. Chattopadhyay *et al.*, Nucl. Instr. and Meth. A **421**,(1999) 558.

[80] M. Y. El-Bakry and K. A. El-Metwally, Chaos, Solitons and Fractals **16**, (2003) 279.

[81] C. Peterson, T. Rognvaldsson, L. Lonnblad, Lund. Univ. *Report LU/TP/93-29;* , CERN-TH 7135/94, 1994.

[82] GEANT - Detector Description and Simulation tool, CERN Program Library W5013. (http://wwwasd.web.cern.ch/wwwasd/geant).

[83] The NUANCE Neutrino Generator, D. Casper, Nucl. Phys. Proc. Suppl. **112**, 161 (2002) (http://www.ps.uci.edu/ nuint/nuance/default.htm).

[84] M. Honda,*et al.*, Phys. Rev. D **70**, (2004), 043008; arXive:astro-ph/0404457.

[85] William H. Press *et al.*, *Numerical Recipes in C* (Cambridge University Press, 1988).

[86] Roy Lee, "Event Reconstruction in the Near Detector", *NuMI-NOTE-COMP-917*.

[87] E.J.Wolin and L.L.Ho, "Covariance matrices for track fitting with the Kalman filter", Nucl. Instr. and Meth. A **329**, (1993) 493.

[88] Tapasi Ghosh and Subhasis Chattopadhyay.Proceedings of the DAE Symposium on Nuclear Physics, Vol. **52**, (2007) 649.

[89] Tapasi Ghosh and Subhasis Chattopadhyay.Proceedings of the DAE Symposium on Nuclear Physics, Vol. **52** (2007) 649.

[90] Tapasi Ghosh and Subhasis Chattopadhyay, AIP. Conf. Proc. 1222, (2010) 447.

[91] Werner Riegler *et al.* Nucl. Instr. Math. A **500**, (2003) 144.

[92] S. Biswas *et al.*, Nucl. Instr. and Meth. A **602**, (2009) 749.

[93] C. Lu Nucl. Instr. Math. A **602**, (2009) 761.

[94] I. Smirnov, Heed, program to computr energy loss of fast particles in gases, Version 1.01, CERN.

[95] W.W.M. Allison and J.H. Cobb, "Relativistic charged particle identification by energy loss." Ann. Rev. Nucl. Part. Sci., **30**, (1980), 253.

[96] W. Blum, L. Ronaldi, particle Detection with drift Chambers, Springer, Berlin, 1993, ISBN 3-540-56425-X.

[97] Werner Legler, Z. Naturforschung, **16a**, (1961) 253.

140

[98] C. Lippmann thesis, Johann Wolfgang Goethe University, 2003.

[99] D.González-Díaz thesis, university of Santiago, 2006.

[100] S. Biabi, Magbolz, program to compute gas transport parameters, Version 2.2, CERN.

[101] A. Blanco *et al.*, Nucl. Instr. and Meth. A **535**, (2004) 272.

[102] D.Gonzalez-Diaz *et al.*, Nucl. Phys. B (Proc. Suppl.) **158**, (2006) 111.

[103] S.Gorbunov and I.Kisel, Nucl. Inst. and Meth. A 559, (2006) 148.

List of Publications

- **Simulation for Iron Calorimeter prototype detector of India-based Neutrino Observatory.**
  Tapasi Ghosh and Subhasis Chattopadhyay,
  AIP. Conf. Proc. (1222) 447.

- **A Monte Carlo simulation to study the surface roughness effect on RPC performance.**
  Tapasi Ghosh and Subhasis Chattopadhyay,
  Nucl. Instr. and Meth. A(2010), doi:10.1016/j.nima.2010.08.070.

- **Track Reconstruction by Kalman Filter Technique.**
  Tapasi Ghosh and Subhasis Chattopadhyay,
  Proceedings of the DAE-BRNS Symposium of Nuclear Physics Vol. 52 , (2007) 649.

- **INO Iron Calorimeter prototype at VECC.**
  Tapasi Ghosh and Subhasis Chattopadhyay,
  Proceedings of the DAE-BRNS Symposium of Nuclear Physics Vol. 53, (2008) 769.

- **A Monte Carlo simulation method to study Resistive Plate Chamber Performance.**
  Tapasi Ghosh and Subhasis Chattopadhyay,
  Proceedings of the DAE-BRNS Symposium of Nuclear Physics Vol. 54, (2009) 664.

- **Discrimination of muons and hadrons in calorimeters for atmospheric neutrino experiment using the Artificial Neural Network.**

Tapasi Ghosh and Subhasis Chattopadhyay.

Proceedings of the DAE-BRNS Symposium of Nuclear Physics Vol. 55, (2010) 750.

- **Effect of surface roughness on the performance of RPC: A Monte Carlo study.**
  Tapasi Ghosh and Subhasis Chattopadhyay.

  Proceedings of the DAE-BRNS Symposium of Nuclear Physics Vol. 55, (2010) 678.